National Library of Canada
Bibliothèque nationale du Canada

Canadian Theses Service
Service des thèses canadiennes

Ottawa, Canada
K1A 0N4

NOTICE

The quality of this microform is heavily dependent upon the quality of the original thesis submitted for microfilming. Every effort has been made to ensure the highest quality of reproduction possible.

If pages are missing, contact the university which granted the degree.

Some pages may have indistinct print especially if the original pages were typed with a poor typewriter ribbon or if the university sent us an inferior photocopy.

Previously copyrighted materials (journal articles, published tests, etc.) are not filmed.

Reproduction in full or in part of this microform is governed by the Canadian Copyright Act, R.S.C. 1970, c. C-30.

AVIS

La qualité de cette microforme dépend grandement de la qualité de la thèse soumise au microfilmage. Nous avons tout fait pour assurer une qualité supérieure de reproduction.

S'il manque des pages, veuillez communiquer avec l'université qui a conféré le grade.

La qualité d'impression de certaines pages peut laisser à désirer, surtout si les pages originales ont été dactylographiées à l'aide d'un ruban usé ou si l'université nous a fait parvenir une photocopie de qualité inférieure.

Les documents qui font déjà l'objet d'un droit d'auteur (articles de revue, tests publiés, etc.) ne sont pas microfilmés.

La reproduction, même partielle, de cette microforme est soumise à la Loi canadienne sur le droit d'auteur, SRC 1970, c. C-30.

NL-339 (r. 88/04)

Canada

THE UNIVERSITY OF ALBERTA

AXIAL LASER DISCHARGE STABILIZATION WITH ROTATING MAGNETIC FIELDS

by

RONALD JOHN WILLIS

A THESIS

SUBMITTED TO THE FACULTY OF GRADUATE STUDIES AND RESEARCH

IN PARTIAL FULFILMENT OF THE REQUIREMENTS FOR THE DEGREE

OF DOCTOR OF PHILOSOPHY

DEPARTMENT OF ELECTRICAL ENGINEERING

EDMONTON, ALBERTA

FALL, 1987

Permission has been granted to the National Library of Canada to microfilm this thesis and to lend or sell copies of the film.

The author (copyright owner) has reserved other publication rights, and neither the thesis nor extensive extracts from it may be printed or otherwise reproduced without his/her written permission.

L'autorisation a été accordée à la Bibliothèque nationale du Canada de microfilmer cette thèse et de prêter ou de vendre des exemplaires du film.

L'auteur (titulaire du droit d'auteur) se réserve les autres droits de publication; ni la thèse ni de longs extraits de celle-ci ne doivent être imprimés ou autrement reproduits sans son autorisation écrite.

ISBN 0-315-40998-3

THE UNIVERSITY OF ALBERTA

RELEASE FORM

NAME OF AUTHOR RONALD JOHN WILLIS

TITLE OF THESIS AXIAL LASER DISCHARGE STABILIZATION WITH ROTATING MAGNETIC FIELDS

DEGREE FOR WHICH THESIS WAS PRESENTED DOCTOR OF PHILOSOPHY

YEAR THIS DEGREE GRANTED FALL, 1987

Permission is hereby granted to THE UNIVERSITY OF ALBERTA LIBRARY to reproduce single copies of this thesis and to lend or sell such copies for private, scholarly or scientific research purposes only.

The author reserves other publication rights, and neither the thesis nor extensive extracts from it may be printed or otherwise reproduced without the author's written permission.

(SIGNED) Ronald J. Willis

PERMANENT ADDRESS:

#201, 7835 - 159 ST

EDMONTON, ALBERTA

CANADA T5R 2E1

DATED June 26 1987

THE UNIVERSITY OF ALBERTA

FACULTY OF GRADUATE STUDIES AND RESEARCH

The undersigned certify that they have read, and recommend to the Faculty of Graduate Studies and Research, for acceptance, a thesis entitled AXIAL LASER DISCHARGE STABILIZATION WITH ROTATING MAGNETIC FIELDS submitted by RONALD JOHN WILLIS in partial fulfilment of the requirements for the degree of DOCTOR OF PHILOSOPHY.

.....
Supervisor

.....
Supervisor

.....

.....

.....

.....
External Examiner

Date June 26, 1987

Dedication

To my wife Debbie, and my parents Hugh and Fern,

for their love and encouragement in my endeavors.

Abstract

Efforts to increase the discharge specific power loading in high power carbon dioxide lasers have been hampered by the onset of electrothermal instabilities. Previous research, performed at the University of Alberta's Laser Laboratory, showed that a stabilization technique, using static magnetic fields, was effective in suppressing these instabilities, in both transverse and coaxial geometries, through the generation of sheared mixing velocities in the bulk gas and magnetic stabilization of the charged sheath regions.

The purpose of this investigation was to adapt this magnetic stabilization technique to an axial discharge, with the use of a transverse rotating magnetic field. Preliminary work, done with a sealed cylindrical discharge chamber, 10 cm in diameter and 25 cm in length, showed that electrothermal instabilities were indeed preventable in such an axial discharge, through a judicious choice of magnetic field profile and strength.

A theoretical analysis showed that the stabilization mechanism in this axial discharge geometry was not a result of the generation of mixing velocities in the bulk gas, as was the case for the transverse and coaxial geometries. In fact, high speed photography revealed that the plasma column was deflected away from the centerline position when the transverse rotating magnetic field was applied. Further theoretical analysis showed that this deflection was the result of a Lorentz force acting on the plasma column. Consequently, as the magnetic field rotated, the plasma column swept around the discharge cross-section. As the magnetic field strength was increased, the Lorentz force grew, thereby deflecting the plasma still closer to the chamber wall.

Experimental studies were performed with the discharge test section, now 50 cm in length, mounted into a recirculating gas loop. Diagnostics, done with a 20 Torr laser gas mixture, included: terminal characteristics, temperature measurements, electron density assessments and gain studies. Laser power output is discussed briefly. The results indicated that a transverse rotating magnetic field can indeed improve gas discharge stability in an axial discharge geometry. A 25% increase in discharge power loading was demonstrated, using this discharge stabilization technique.

Acknowledgements

The author wishes to thank his supervisors, Dr. C.E. Capjack and Dr. H.J.J. Seguin. Their guidance, patience and encouragement throughout the past five years is greatly appreciated.

Thanks also goes to the members of the laser research group for their invaluable assistance. In particular, Dr. S.K. Nikumb was of great help in the experimental tests, especially the gain measurements. In addition, Mr. H. Reshef and Mr. D. Presakarchuk are thanked for their assistance in overcoming a variety of mechanical and electronic problems.

The author also gratefully acknowledges the University of Alberta and the Natural Sciences and Engineering Research Council for the financial support provided.

Table of Contents

Chapter		Page
1.	INTRODUCTION	1
	1.1 Background History of the Carbon Dioxide Laser	1
	1.2 The Physics of Laser Action	4
	1.2.1 Vibrational Levels of the Carbon Dioxide Molecule	5
	1.2.2 Upper Laser Level Excitation Mechanism	5
	1.2.3 Collisional Relaxation Mechanisms	7
	1.2.4 Effect of Gas Temperature on the Lasing Process	8
	1.3 Plasma Chemistry	8
	1.4 Discharge Instabilities	10
	1.4.1 Ionization Instabilities	10
	1.4.2 Thermal Instabilities	17
	1.5 Discharge Stabilization Mechanisms	20
	1.5.1 External Ionization	20
	1.5.2 Magnetic Stabilization	21
	1.6 Scope of this Thesis	25
2.	THEORETICAL ANALYSIS	26
	2.1 Fundamental Plasma Parameters	26
	2.1.1 Collision Frequency	26
	2.1.2 Viscosity and Thermal Conductivity	31
	2.1.3 Specific Heat Capacity	33
	2.1.4 Mobility and Electrical Conductivity	35
	2.1.5 Effective Pressure	38
	2.1.6 Townsend's First Ionization Coefficient	41
	2.2 Bulk Rotation	42
	2.3 Lorentz Force on the Plasma Column	49

3. SYSTEM DESIGN 53

3.1 Vacuum System 53

3.2 Gas Transport System 56

3.3 Magnetic Field Supply and Characteristics 58

3.4 Electrode Design 60

3.5 Thyratron Pulser Ionization System 64

3.6 Sustainer Power Supply Connections 68

4. EXPERIMENTAL RESULTS AND OPERATIONAL CHARACTERISTICS 69

4.1 Terminal Characteristics 69

4.2 Gas Discharge Temperature Measurements 86

4.3 Electron Density Measurements 94

4.3.1 Electron Density: Zero Gas Velocity, Zero Magnetic Field 100

4.3.2 Electron Density: Zero Gas Velocity, 450 G Rotating Magnetic Field 103

4.3.3 Electron Density: 10 m/sec Gas Velocity 106

4.3.4 Electron Density: Radial Variation 106

4.3.5 Electron Density: Pulser Variation 110

4.3.6 Electron Density: Conclusions 115

4.3.7 Electron Density: Measurements at Low Pressure (5 Torr) 116

5. GAIN OPTIMIZATION, SATURATION INTENSITY AND LASER POWER 121

5.1 Gain Optimization 121

5.2 Gain Measurement Theory and Apparatus 124

5.3 Burst Pulse Gas Discharge Technique 126

5.4 Gain Measurements 128

5.5 Saturation Intensity 136

5.6 Laser Power Measurements 139

6. CONCLUSIONS AND CONSIDERATIONS FOR FUTURE RESEARCH 141

List of Tables

Table		Page
2.1	Molecular Radii and Masses of the Laser Gases	28
2.2	Heavy Particle Collision Cross-Sections	28
2.3	Average Molecular Mass and Cross-Sections for Several Typical Laser Gas Mixtures	29
2.4	Electron-Neutral Momentum Transfer Cross-Sections[11]	29
2.5	Pure Gas Viscosities and Thermal Conductivities for He, N_2 and CO_2 (T = 150°C)	32
2.6	Viscosity and Thermal Conductivity for Several Typical Laser Gas Mixes (T = 150°C)	32
2.7	Specific Heat Capacity for He, N_2, CO and CO_2	34
2.8	Specific Heat Capacities for Several Typical Laser Gas Mixtures	34

List of Figures

Figure		Page
1.1	CO_2 Laser Gas Flow Geometries	2
1.2	Energy Level Diagram of the CO_2:N_2:He Laser[10]	6
1.3	Ionization, Attachment and Recombination Coefficients vs. Electron Temperature[20]	12
1.4	Sequence of Events Following an Initial Disturbance in Electron Density[20]	15
1.5	Sequence of Events Leading to Discharge Thermal Instabilities[35]	19
1.6	Electrothermal Instability Growth Times[35]	19
1.7	Schematic of the Initial Magnetically Stabilized Transverse Gas Discharge[44]	22
1.8	Magnetic Field Profile of the Electromagnet shown in Fig. 1.7[44]	23
1.9	Schematic of the Coaxial Magnetically Stabilized Gas Discharge[43]	24
2.1	Electron Mobility vs. Collision Frequency: Effect of Magnetic Field	37
2.2	Radial Temperature Profile	39
2.3	Spatial Variation of Pedersen Electron Mobility vs. Magnetic Field	40
2.4	Azimuthal Velocity vs. Radius: Hartmann Number	48
2.5	Effect of Magnetic Field on the Apparent Radial Boundary of the Gas Discharge at Low Pressure (3.5 Torr)	51
3.1	Schematic of System	54
3.2	Detail of the Gas Discharge Test Section	55
3.3	Axial Gas Flow Velocity vs. RPM	57
3.4	Transverse Magnetic Field Strength Profiles	59
3.5	Initial Electrode Designs	61
3.6	Button Electrode Structure	63
3.7	Discharge Excitation System	65
3.8	Pulser Characteristic: Effect of DC Current	67
4.1	V-I Characteristics, B = 0: Effect of Gas Velocity	71
4.2	V-I Characteristics, B = 450 Gauss: Effect of Gas Velocity	72

4.3 V-I Characteristics: Effect of Magnetic Field 73
4.4 V-I Characteristics: Variation of Magnetic Field 74
4.5 Maximum Input Power vs. Gas Velocity 75
4.6 Input Power vs. Magnetic Field 76
4.7 V-I Characteristics, B = 0: Effect of Pulser Input Voltage 77
4.8 V-I Characteristics, B = 450 Gauss: Effect of Pulser Input Voltage 78
4.9 Input Power vs. Pulser Power, B = 0 80
4.10 Input Power vs. Pulser Power, B = 450 Gauss 81
4.11 Input Power vs. Pulser Power: Effect of Magnetic Field 82
4.12 V-I Characteristics: 1/0/4/15 Gas Mixture 83
4.13 V-I Characteristics: 2/0/2/16 Gas Mixture 84
4.14 V-I Characteristics: 2/1/2/15 Gas Mixture 85
4.15 Radial Temperature Profiles, B = 0: Variation of Input Power 87
4.16 Radial Temperature Profiles, B = 450 Gauss: Variation of Input Power 88
4.17 Gas Outlet Temperature vs. Input Power 89
4.18 Gas Outlet Temperature vs. Gas Velocity 91
4.19 Gas Outlet Temperature vs. Time 93
4.20 Electron Density Probe Apparatus 95
4.21 Electron Density Probe Characteristics: B = 0 101
4.22 Electron Density vs. Current: B = 0 102
4.23 Electron Density Probe Characteristics: B = 450 Gauss 104
4.24 Electron Density vs. Current: B = 450 Gauss 105
4.25 Electron Density Probe Characteristics: 10 m/sec Gas Flow 107
4.26 Electron Density vs. Current: 10 m/sec Gas Flow 108
4.27 Electron Density Probe Characteristics: Radial Variation 109
4.28 Electron Density Probe Characteristics, B = 0: Effect of Pulser Input Voltage 111
4.29 Electron Density vs. Pulser Input Voltage: B = 0 112

4.30 Electron Density Probe Characteristics, B = 450 Gauss: Effect of Pulser Input Voltage 113

4.31 Electron Density vs. Pulser Input Voltage: B = 450 Gauss 114

4.32 Electron Density Probe Characteristics at 5 Torr: Oscilloscope Traces 118

4.33 Spatial Variation of Electron Density at 5 Torr 119

5.1 Percentage of Power Input Transferred to the Upper Laser Level[24] 122

5.2 Gain Measurement Apparatus 125

5.3 Gain Coefficient vs. DC Input Voltage 130

5.4 Gain Coefficient vs. Magnetic Field 132

5.5 Maximum Gain Coefficients vs. Radial Position 133

5.6 Gain Coefficient vs. Pulser Input Voltage 135

5.7 Saturation Intensity 138

5.8 Laser Output Energy vs. Input Voltage 140

CHAPTER I

INTRODUCTION

In the past 20 years, the carbon dioxide laser has evolved from Patel's simple laboratory device, with an output of ~1mW, into one of the most versatile industrial lasers in use today. Industrial CO_2 lasers in the 1 kW range are now routinely used for cloth cutting, marking and scribing. Lasers with outputs of 2-5 kW have been successfully utilized for cutting, welding, drilling and heat treating various metals.[1] Very high power lasers, with up to 20kW output power, have been developed for heavy section welding in the pipeline and ship building industries.[2]

As the number of applications for industrial CO_2 lasers has grown, so has the need for more compact and more powerful devices. This has translated into a requirement for higher power densities within the CO_2 gas discharge. In this chapter, a brief history of the evolution in higher power densities, in the context of CO_2 laser development, will be presented. This is followed by a discussion covering the physics of the laser process and plasma chemistry of the gas discharge. Next is an investigation of discharge instabilities, which have been found responsible for limiting the input power density to the glow discharge. Lastly is a discussion of how these instabilities may be suppressed or prevented.

1.1 Background History of the Carbon Dioxide Laser

The first CO_2 laser devices, shown schematically in Fig. 1.1(a), were simply sealed-off discharge tubes or devices with a slow axial gas flow. In either case, the waste heat is rejected by simple diffusion to the cooled outer walls. The characteristic diffusion time, τ_D, associated with this process, is given by:[3]

$$\tau_D = \frac{D^2}{\lambda_m c}, \tag{1.1}$$

where D, λ_m and c are the tube diameter, mean free path of the CO_2 molecules in the gas

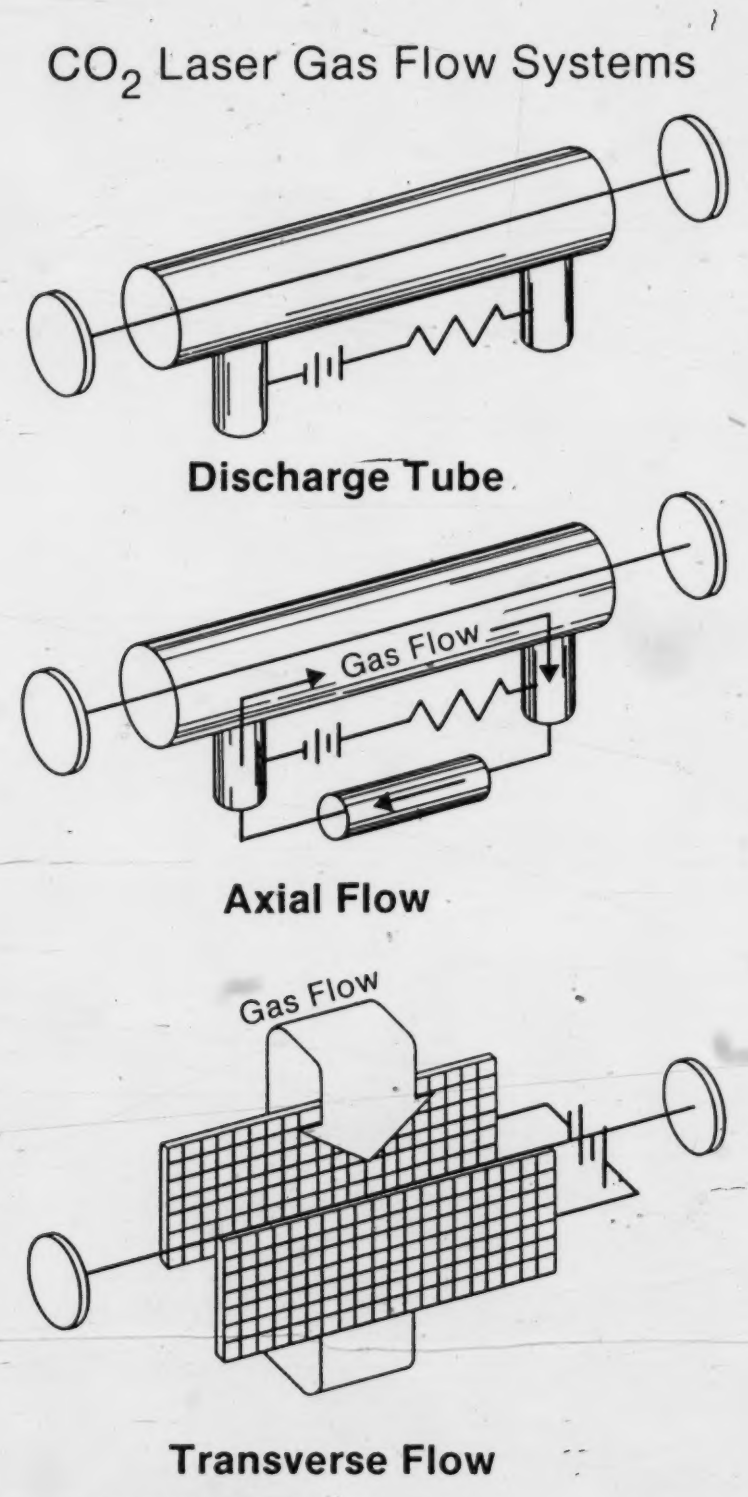

Fig. 1.1 CO_2 Laser Gas Flow Geometries

mixture and the thermal molecular speed respectively. The maximum CW laser output power density, P_D, attainable with such a device, has been shown to be inversely proportional to this characteristic diffusion time[3], namely:

$$P_D \alpha \rho \frac{\lambda_m c}{D^2} \tag{1.2}$$

where ρ is the mass density. Since the mean free path is inversely proportional to pressure, the enhanced heat transfer benefits normally expected from an increased pressure, are unfortunately negated by the reduced mean free path. Similarly, increasing the tube diameter also provides no additional benefit, because the power per unit volume decreases at the same rate as the volume itself is increasing. Thus, the power output per unit length of a diffusion-cooled laser has been found to be essentially fixed; typically at ~70 W per meter of discharge length.[4] Consequently, the only means of significantly increasing the power output, for diffusion-cooled lasers, is to increase the tube length. Because of this fact, lasers as long as 220 feet have been reported; providing an output of a few kilowatts.[5] Recently, more practical systems have been developed, that use several parallel mounted laser tubes, optically coupled with folding mirrors.[4]

The next major advance in the evolution of the CO_2 laser transpired when researchers discovered the enormous benefits that could be derived with convection cooling.[6,7] In these devices, the inefficient diffusion-cooling process is replaced by convection of the hot gas, completely out of the active discharge region. The characteristic time for a "convection-cooled" discharge now becomes:

$$\tau_C = \frac{L}{V} , \tag{1.3}$$

where L and V are the discharge length in the direction of gas flow and the gas flow velocity respectively. Hence the achievable laser power output density, P_C, is:[8]

$$P_C \alpha \rho \frac{V}{L} . \tag{1.4}$$

The fast axial flow convection-cooled laser geometry is shown in Fig. 1.1(b), where the discharge tube has simply been modified to permit fast-axial convection of the hot gas out of the active discharge region. As will be discussed in section 1.4.2, the characteristic growth time for thermal instabilities in a 20 Torr laser discharge is ~1 msec. Thus, if the dwell time of the gas molecules in the active discharge region is to be kept below 1 msec, a velocity of 1000 m/sec per meter of discharge length is required. In order to move the gas at these very high velocities through a narrow bore discharge tube necessitates the use of a high static pressure Roots blower. This fact implies that a dramatic increase in the cost and complexity of the system results. However, in spite of this difficulty, commercial lasers up to 2 kW are still generally of the fast axial flow geometry.[9]

Tiffany, Targ and Foster[8] noted that if the discharge length in the direction of gas flow could be reduced to a few cm, then the requirements on the gas transport system were such that conventional blower technology could now be used. Their work led to the development of the transverse flow geometry, shown in Fig 1.1(c). In this configuration, the excitation field, optical axis and the direction of gas flow are all mutually orthogonal. The length of the discharge in the direction of gas flow is simply the width of the electrode structure. Thus, the requirements of the gas transport system are greatly reduced, as revealed by examination of Eq. 1.4. As a consequence of this situation, transverse flow geometries have become standard for most high power (over 5kW) CO_2 lasers available commercially today.[9]

1.2 The Physics of Laser Action

This section will concern itself with the physics of CO_2 laser action. Vibrational energy levels of the CO_2 molecule will be presented first, followed by a discussion of the upper laser level excitation mechanisms. Next, the details of lower laser level relaxation will be presented.

1.2.1 Vibrational Levels of the Carbon Dioxide Molecule

The energy level diagram for a CO_2 laser, presented in Fig. 1.2, reveals that the CO_2 laser is a 4 level system, capable of lasing at 10.6 and 9.4 microns. The 10.6 μm laser transition is between the asymmetric stretch (00^01) and the symmetric stretch (10^00) vibrational levels; while laser action at 9.4 μm results from the transition between the asymmetric stretch (00^01) and the bending (02^00) vibrational levels. Depopulation of the lower laser levels (10^00 and 02^00) is by collisional relaxation to the ground state (00^00) via the bending vibrational level (01^10).

1.2.2 Upper Laser Level Excitation Mechanism

Excitation of the upper laser level, $CO_2(00^01)$ is either by resonant energy transfer from the excited nitrogen molecules, which is given by:[10]

$$e + N_2(v=0) \rightarrow N_2(v=n\leq 8) + (e - K.E.)\,, \qquad (1.5)$$

followed by:

$$N_2(v=n) + CO_2(00^00) \rightarrow N_2(v=n-1) + CO_2(00^01)\,, \qquad (1.6)$$

or else by direct electron impact of the CO_2 molecules in the ground state:

$$e + CO_2(00^00) \rightarrow CO_2(00^01) + (e - K.E.)\,, \qquad (1.7)$$

where K.E. is kinetic energy. Elliot, Judd, Lockett and Rockwood have presented comprehensive lists of the cross-sections for both of these mechanisms.[11]

If CO is present in sizeable quantities, then the vibrationally excited CO may also provide some excitation for the upper CO_2 laser level by resonant energy transfer. However, the energy difference between $CO_2(00^01)$ and $CO(v=1)$ is greater than that between $CO_2(00^01)$ and $N_2(v=1)$. Hence, resonant energy transfer between CO and CO_2 is a less efficient process.[12]

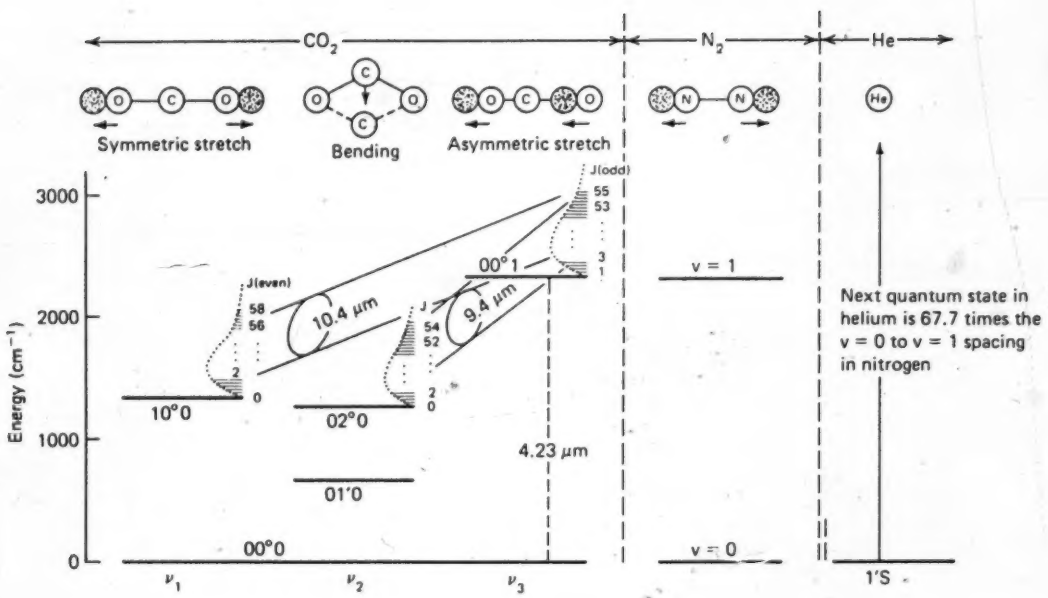

Fig. 1.2 Energy Level Diagram of the CO_2:N_2:He Laser[10]

1.2.3 Collisional Relaxation Mechanisms

The collisional relaxation mechanisms for the upper laser level, which compete directly with stimulated emission of laser radiation, are given below, with their rate coefficients for a temperature of 300K.[12]

$$CO_2(00^01) + He \rightarrow CO_2(04^00) + He \qquad k < 85\ sec^{-1}\text{-}Torr^{-1} \qquad (1.8)$$

$$CO_2(00^01) + N_2(v=0) \rightarrow CO_2(00^00) + N_2(v=1) \qquad k \simeq 106\text{-}110 \qquad (1.9)$$

$$CO_2(00^01) + CO_2(00^00) \rightarrow CO_2(00^00) + CO_2(11^10) \qquad k \simeq 350\text{-}365 \qquad (1.10)$$

$$CO_2(00^01) + CO(v=0) \rightarrow CO_2(00^00) + CO(v=1) \qquad k \simeq 993 \qquad (1.11)$$

Nitrogen and helium, which account for ~80% of a typical laser gas mixture, have relatively low rate coefficients, and therefore are poor at relaxation of the upper laser level. Carbon dioxide and carbon monoxide have higher rate coefficients. However, the coefficients are mixture weighted, and these constituents typically account for less than 20% of a CO_2 laser gas mixture.

Collisional relaxation of the lower laser level is a two part process. The first is a fast vibrational relaxation to the $CO_2(01^10)$ level given by:[12]

$$CO_2(10^00,02^00) + CO_2 \rightarrow 2CO_2(01^10) \qquad k > 6(10)^5\ sec^{-1}\text{-}Torr^{-1} \qquad (1.12)$$

This is followed by a somewhat slower collisional relaxation of the $CO_2(01^10)$ vibrational level to the ground state, $CO_2(00^00)$. These processes and their rate coefficients, again for 300K, are given by:[12]

$$CO_2(01^10) + CO_2 \rightarrow 2CO_2(00^00) \qquad k \simeq 175\text{-}210\ sec^{-1}\text{-}Torr^{-1} \qquad (1.13)$$

$$CO_2(01^10) + CO \rightarrow CO_2(00^00) + CO \qquad k \simeq 4(10)^3 \qquad (1.14)$$

$$CO_2(01^10) + He \rightarrow CO_2(00^00) + He \qquad k \simeq (3.5\text{-}5.3)10^3 \qquad (1.15)$$

Eq. 1.15 demonstrates the effectiveness of the majority constituent, helium, in deactivating the $CO_2(01^10)$ vibrational level. This benefit, in addition to the improvement in thermal conductivity and the adjustment of discharge E/N are the primary reasons for adding helium

to a laser gas discharge.

1.2.4 Effect of Gas Temperature on the Lasing Process

Collisional relaxation is a strong function of gas temperature. Because the $CO_2(01^10)$ vibrational level is close to the ground state, any increase in the gas temperature tends to increase the population of the $CO_2(01^10)$ vibrational level from the ground state, $CO_2(00^00)$. This in turn reduces the depopulation rate of the lower laser levels, $CO_2(10^00)$ and $CO_2(02^00)$. Furthermore, the collisional relaxation of the upper laser level increases with increasing gas temperature, thereby decreasing the upper laser level population.[13]. This temperature effect, known as "thermal bottlenecking", results in a reduced population inversion and concomitant drop in laser power output. It is for this reason that some of the pioneering work with CO_2 lasers was done with gas discharge tubes cooled to temperatures as low as -60°C.[14] Unfortunately, this option is of value only for narrow bore diffusion cooled gas discharges. Detailed studies of the laser power output as a function of gas temperature have been made by Franzen and Collins[15], and by Bullis, Nighan, Fowler and Wiegand.[16]

1.3 Plasma Chemistry

The same electrons used to excite the vibrational modes of N_2 and CO_2 are also involved in a host of other chemical reactions that produce a number of secondary species. An analysis by Wiegand and Nighan[17], has shown that the principle secondary species in an electrically excited CO_2:N_2:He gas discharge are CO, O and N. These disassociation products accumulate rapidly, reaching concentrations of 1% of the initial species within ~0.01 seconds.[17] The principal ionic secondary species is O^-, which leads to the formation of CO_3^- ions through a three body collision reaction. In this section, the basic chemical reactions occuring in a CO_2:N_2:He laser discharge are presented. These reactions may be grouped into five major types: ionization, dissociative attachment, dissociative recombination, ion-ion recombination and associative detachment.

The ionization reactions and their rate coefficients (for an electron temperature, T_e, of 1eV) for a typical CO_2:N_2:He discharge are as follows.[17]

$$e + CO_2 \rightarrow CO_2^+ + 2e \qquad k_i \simeq 1(10)^{-14}\text{–}2(10)^{-12}\text{cm}^3/\text{sec} \qquad (1.16)$$

$$e + N_2 \rightarrow N_2^+ + 2e \qquad k_i \simeq 1(20)^{-15}\text{–}2(10)^{-13} \qquad (1.17)$$

Only those electrons in the high energy tail of the electron distribution can cause ionization. Thus, the ionization rate coefficients are a strong function of electron temperature[17]. Few ionizations of He occur because the ionization energy for He is 24.6 eV compared with 13.79 eV and 15.58 eV for CO_2 and N_2 respectively.[18]

The principle dissociative attachment reaction for a CO_2:N_2:He discharge, which is also a strong function of electron temperature, is given by:[19]

$$e + CO_2 \rightarrow CO + O^- \qquad k_a \simeq 5(10)^{-13}\text{cm}^3/\text{sec} \qquad (1.18)$$

The secondary species generated by ionization and dissociative attachment are themselves involved in further reactions. Dissociative recombination reactions, which have a weak dependence on electron temperature[17] are presented below, together with their rate coefficients:[19]

$$e + CO_2^+ \rightarrow CO + O \qquad k_r^e \simeq 6.0(10)^{-8}\text{cm}^3/\text{sec} \qquad (1.19)$$

$$e + N_2^+ \rightarrow N + N \qquad k_r^e \simeq 2.8(10)^{-7} \qquad (1.20)$$

Ion-ion recombinations and associative detachment reactions have no dependence on electron temperature, since they do not have electrons as their reactants. The reactions that involve the secondary products of ionization and dissociation attachment are given below:[19]

$$O^- + N_2^+ \rightarrow O + N_2 \qquad k_r^i \simeq 2.0(10)^{-7}\text{cm}^3/\text{sec} \qquad (1.21)$$

$$O^- + CO \rightarrow CO_2 + e \qquad k_d \simeq 6.5(10)^{-10} \qquad (1.22)$$

$$O^- + N_2 \rightarrow N_2O + e \qquad k_d \simeq 2.0(10)^{-19} \qquad (1.23)$$

The oxygen ions are also involved in a clustering reaction with CO_2 in the three body collision

given by:[20]

$$O^- + 2CO_2 \rightarrow CO_3^- + CO_2 \qquad k_c \simeq 1.1(10)^{-27} cm^6/sec \qquad (1.24)$$

Formation of the O^- ion has a large influence on the discharge operating conditions, even when external ionization is used.[20] The relation between negative ion production and the ionization instability in covered is section 1.4.1.

1.4 Discharge Instabilities

As indicated previously, convection cooling represented a major advance in the engineering of CO_2 electric discharge lasers. However, when researchers scaled these devices to larger volumes and higher pressures, they found that the achievable plasma power density was severely limited by the onset of plasma instabilities. The most common instabilities observed in low pressure glow discharges are the occurrence of ionization waves (striations) and discharge constriction.

1.4.1 Ionization Instabilities

In a comprehensive paper, Haas has investigated the hydrodynamic instability processes for weakly-ionized, volume-dominated glow discharges.[21] Further studies, by Haas, Nighan and Wiegand, revealed that negative ion formation plays an important role in promoting ionization instabilities.[22] The next few paragraphs will discuss how this instability forms, and more importantly, how it may be prevented.

The formation of ionization waves in a plasma is fundamentally related to the production and loss mechanisms of electrons and negative ions in the plasma. For a weakly ionized, volume-dominated glow discharge, the electron conservation equation may be written:[20]

$$\frac{\partial n_e}{\partial t} = n_e n k_i - n_e n_p k_r^e - n_e n k_a + n_n n k_d + nS \qquad (1.25)$$

where n_e, n_n, n_p, and n are the number densities for electrons, negative ions, positive ions

and the neutrals respectively. The parameters k_i, k_r^e, k_a and k_d are the mixture weighted rate coefficients[20] for ionization, dissociative recombination, dissociative attachment and associative detachment respectively. Parameter S is the source of external ionization. Similarly, the negative ion conservation equation is:[20]

$$\frac{\partial n_n}{\partial t} = n_e n k_a - n_n n k_d - n_n n_p k_r^i \,, \tag{1.26}$$

where k_r^i is the rate coefficient for ion-ion recombination. The balance between electron production and loss mechanisms determines the value of E/N (electric field/neutral density) that is required to sustain the discharge. Sensitivity of the rate coefficients for a representative gas mixture are shown in Fig. 1.3.

For a self-sustained discharge, electron production by ionization and detachment must be balanced by the loss mechanisms of recombination and attachment, as suggested by Eq. 1.25. The relative importance of the detachment reaction given by:

$$O^- + CO \rightarrow CO_2 + e \,, \tag{1.27}$$

determines which loss mechanism is dominant.

If the concentration of the detaching species, CO, is low, then in the steady state, the electron conservation equation reduces to:

$$k_i = k_a + (n_p/n) k_r^e \,. \tag{1.28}$$

Fig. 1.3 reveals that for a self-sustained discharge, $k_a >> (n_p/n) k_r^e$, and so $k_i \simeq k_a$. The point at which electron production by ionization balances the electron loss by attachment occurs at the point labelled "A" in Fig. 1.3, where the electron temperature is ~1.5eV.

Conversely, in the strong detachment limit, the high concentration of the detaching species, CO, is large enough to immediately convert O^- back to CO_2 and a free electron. With a small negative ion concentration, ion-ion recombination will be negligible compared with the detachment loss mechanism. Thus, in the steady state, electron loss by attachment is balanced by the detachment process, and the negative ion conservation equation may then be written

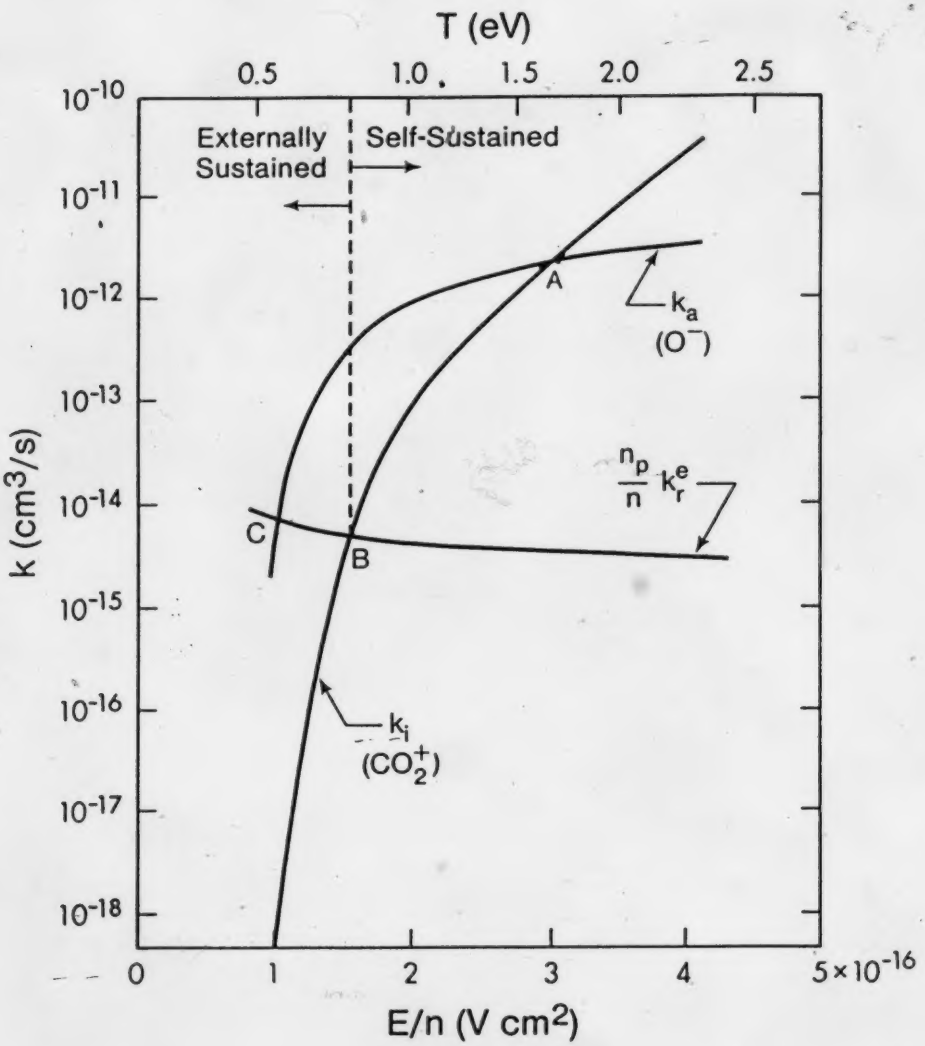

Fig. 1.3 Ionization, Attachment and Recombination Coefficients vs. Electron Temperature[20]

as:

$$n_e n k_a = n_n n k_d \ . \tag{1.29}$$

Upon substitution into the electron conservation equation,

$$k_i = (n_p/n) k_r^e \ . \tag{1.30}$$

Refering again to Fig. 1.3, the strong detachment operating point where electron production by ionization is balanced by recombination, occurs at the point labelled "B". Hence, in the strong detachment limit, the discharge can be sustained at a much lower electron temperature.

Wiegand, Fowler and Benda[23] have shown that CO is readily produced in discharges containing CO_2. Wiegand and Nighan, in a study of CO_2 plasma chemistry, determined that in ~0.01 sec, the accumulation of CO by CO_2 dissociation may reach concentrations on the order of 1% of the initial CO_2 density.[17] In a later study, they showed that if the CO concentration has time to accumulate to a concentration greater than 10% of the initial CO_2 density, then negative-ion processes are insignificant.[20] Thus, the concentration of the detaching species, CO, determines where, (between points "A" and "B"), the discharge operating point will be. Operation at the no detachment limit (point "A"), is only possible for fast-flow convection cooled lasers with a residence time less than ~0.01sec. In sealed-off or slow-flow lasers, where the CO concentration has time to accumulate, or else in discharges containing CO as a primary species, operation is typically at the strong detachment limit (point "B"). Experimentally, the entire range from "A" to "B" is accessible, by varying the dwell time of the CO_2 molecules in the active discharge.[23]

The major disadvantage of self-sustained operation is that E/N, (and the electron temperature), are dependent on the electron production and loss mechanisms. Because only the high energy tail of the electron distribution is capable of providing ionization, the discharge E/N is somewhat higher than optimum for maximum efficiency of upper laser level excitation.[24] A further drawback of self-sustained operation is the difficulty in providing uniform ionization in large volumes. This has resulted in the development of high-energy

electron beams[25], as well as photoionization techniques[26,27,28] to provide external sources of ionization. Generally, for externally sustained discharge, operation is to the left of point "B" in Fig. 1.3, at an E/N that is inaccessible under self-sustained operation. Under these conditions, the ionization from the external source is almost totally responsible for electron production ($S >> n_e k_i$). In the strong detachment limit, where the electron loss mechanism is dominated by recombination, the use of external ionization results in both the electron loss and production mechanisms being relatively insensitive to electron temperature. In the no detachment limit, the electron loss mechanism by attachment is still a strong function of electron temperature. This strong dependence on electron temperature may lead to ionization instabilities, as will be discussed below. Refering to Fig. 1.3, it is clear that if the discharge is attachment dominated, then it is necessary to operate to the left of point "C", where recombination again becomes the dominant loss mechanism.

Nighan and Wiegand, in their investigation of negative-ion processes in a glow discharge, have determined that the ionization instability mechanism is related to the electron temperature dependence of the electron production and loss mechanisms.[20] The ionization instability processes and their characteristic times are shown in Fig. 1.4. Consider a discharge perturbation that results in local fluctuations in the electron density. Haas shows that in a volume dominated discharge, the resulting fluctuation in electron temperature is 180° out of phase with the fluctuation in electron density.[21] This results from the electron temperature dependence of the energy exchange collision frequency being stronger than that of the momentum transfer collision frequency.[22] Thus, a positive local fluctuation in electron density is accompanied by a negative fluctuation in electron temperature. How the discharge reacts to this perturbation is dependent on the effectiveness of the detachment mechanism.

Consider first, the recombination dominated discharge, where the detachment mechanism is strong. Fig. 1.3, reveals that the electron loss mechanism, k_r^e, is relatively insensitive to changes in electron temperature. However, the electron production mechanism, k_i, is strongly dependent on electron temperature, and a decrease in electron temperature is accompanied by a sharp decrease in k_i, with concomitant decrease in electron density. Thus,

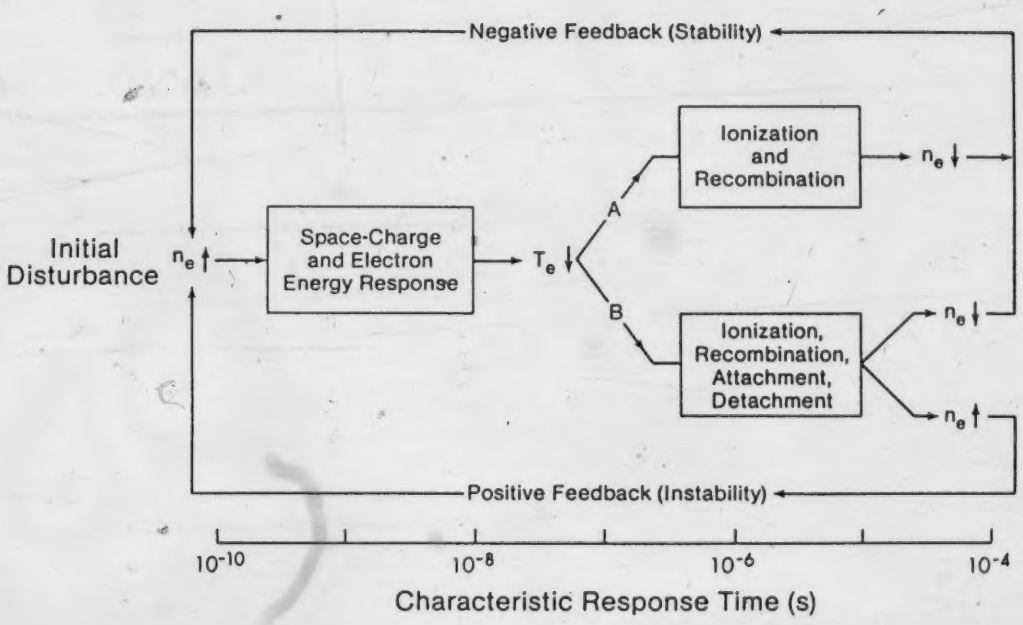

Fig. 1.4 Sequence of Events Following an Initial Disturbance in Electron Density[20]

the recombination dominated discharge responds to a positive local perturbation in electron density by reducing the production of electrons. This is negative feedback, and so an ionization instability will not occur in a recombination dominated discharge.

Now consider an attachment dominated discharge. In this case, both the electron production and loss mechanisms are strong functions of electron temperature. Thus, the stability of the discharge is not only dependent on the magnitudes of k_i and k_a, but also on their rate of change with respect to the electron temperature. Nighan and Wiegand[20] have shown that a necessary condition for an ionization instability to occur may be expressed as:

$$\frac{k_a \hat{k}_a}{k_i \hat{k}_i} > 1, \tag{1.31}$$

where $\hat{k}_{a(i)} = \partial ln k_{a(i)} / \partial ln T_e$. Nighan and Wiegand[22] calculated that this condition was easily met for conditions typical of an attachment dominated CO_2 laser discharge. A local positive fluctuation in electron density results in an increased negative ion population due to dissociative attachment. This in turn increases the electron density as a result of associative detachment. If recombination can dissipate this increase in electron density, then the discharge remains stable. However, if not, then the increased electron density reinforces the initial disturbance. This is positive feedback, which results in an ionization instability, as shown in Fig. 1.4. In a theoretical study, Shapiro[29] has shown that the ionizational instability may be suppressed using a rotating electric field. His analysis was based on the results reported by Nighan, Wiegand and Hass[22] showing that the formation of striations was a peaked function of the electric field direction. A later experimental investigation, by Lipatov, Mineev, Myshenkov, Pashinin and Prokhorov[30], demonstrated that an alternating magnetic field was also effective in suppressing the ionizational instability in an attachment dominated discharge.

In conclusion, ionization instabilities which manifest themselves as discharge striations do not occur if the discharge is recombination dominated. That is, if the detaching species, CO, concentration is at least 10% that of CO_2, the ionization instability is entirely preventable.

1.4.2 Thermal Instabilities

The second, and most troublesome, instability common to glow discharges is a thermal instability which eventually results in discharge constriction. Numerous authors have studied this phenomena for high pressure noble gas discharges.[31,32,33] Discharge constriction in high-power volume-dominated CO_2 lasers has been studied by Jacob and Mani[34], Nighan and Wiegand[35], and later again by Nighan.[36]

Jacob and Mani[34] present an analysis of the discharge constriction phenomena based on the effects of a spatially non-uniform electrical conductivity. Their analysis, which assumes that the input electrical energy in converted instantly into translational energy of the gas, finds that the growth rate of the thermal instability varies as the cube root of the power density for high input power. They present the following physical description for the conditions leading to the formation of a constricted arc discharge. Consider a density perturbation that results in a localized increase in plasma conductivity. Additional current flows into this enhanced conductivity area resulting in gas heating, and concomitant decrease in the gas density. Conductivity increases further, thereby providing a positive feedback mechanism for the initial perturbation, until the originally diffuse glow collapses into a constricted discharge.

Nighan and Wiegand[35] analyzed this constriction phenomena, by considering a discharge having a single diatomic species with a vibrational temperature, T_V, and a translational temperature, T. The sequence of events leading to a thermal instability in such a system is shown in Fig. 1.5, and may be explained as follows. Consider a localized decrease in neutral density with concomitant increase in neutral temperature. This immediately leads to an increase in the electron and vibrational temperatures, as shown by the solid lines. An increased electron temperature and density promotes direct electron gas heating (path #2), as well as vibrational excitation of the diatomic species (path #1). Vibrational relaxation of the molecules also leads to increased gas heating (path #3). Thus, there are two positive feedback mechanisms for the initial disturbance. If thermal conductivity is unable to dissipate this additional heat load, then the process depicted by Fig. 1.5 will lead to discharge

constriction.

Haas[21] has shown that external ionization enables the electron production and loss mechanisms to be decoupled from perturbations in electron temperature or gas density. Nighan and Wiegand[35], in an experimental study, documented that external ionization has a moderating influence on electron density perturbations, and thus improves gas discharge stability.

Electrothermal instability growth times, as a function of discharge power density for a recombination dominated discharge, are shown in Fig. 1.6. Results are presented for 20 and 200 Torr for a series of disturbance scale lengths, ℓ. This figure reveals a number of interesting features. Firstly, the growth time for thermal instability formation varies inversely with discharge power density. Secondly, the growth times are reduced with an increased pressure. Thirdly, since the growth times are always positive, the discharge is inherently unstable, regardless of power density; a result that is confirmed by Nighan in a later report.[36] Thus, in order to maintain a stable and diffuse discharge, one must ensure that the residence time of the gas molecules in the active discharge region is less than the time for electrothermal instability growth. For a pressure of 20 Torr, this means a maximum residence time of ~1 msec. If the residence time is longer than 1 msec, a situation can occur where the upstream end of the discharge is a well behaved glow discharge, while further downstream, the discharge is constricted.[37]

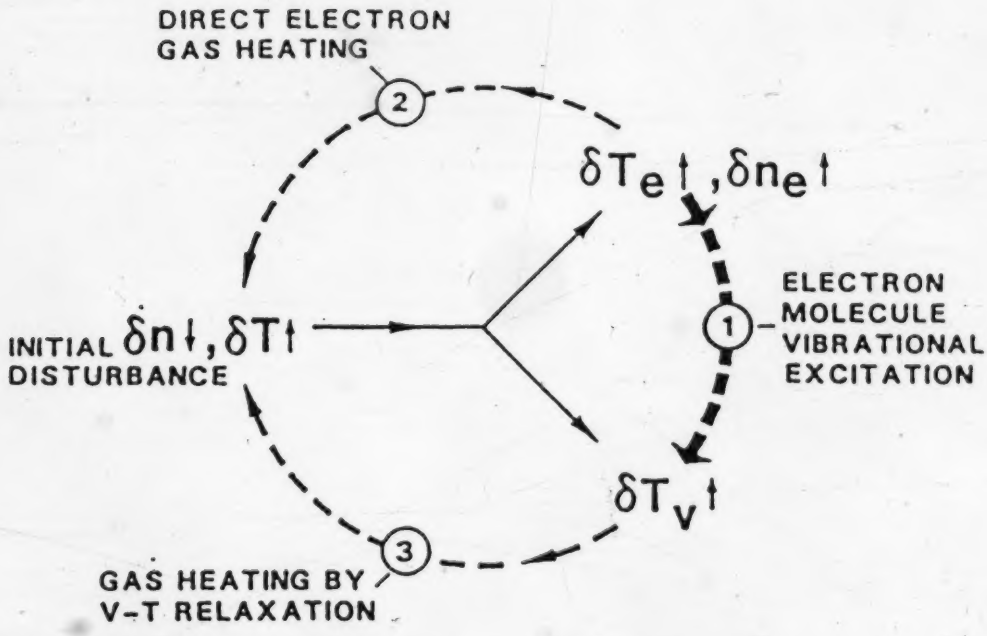

Fig. 1.5 Sequence of Events Leading to Discharge Thermal Instabilities[35]

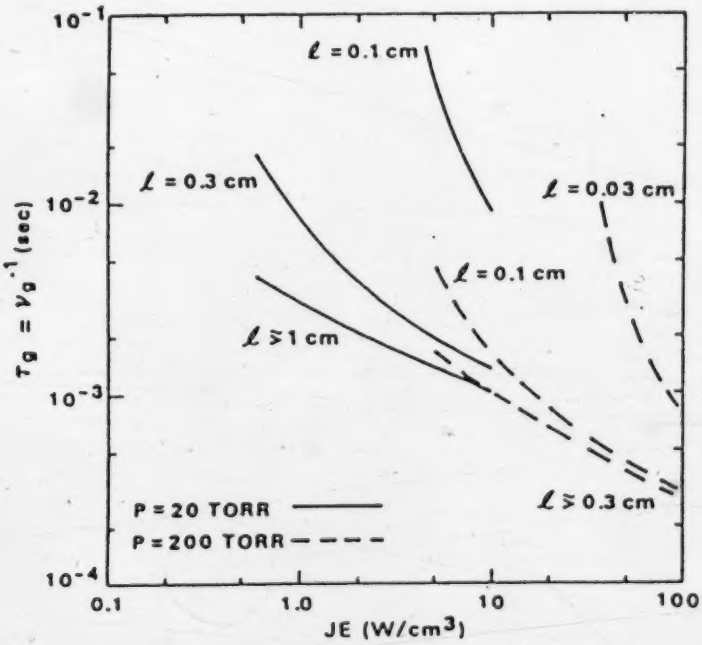

Fig. 1.6 Electrothermal Instability Growth Times[35]

1.5 Discharge Stabilization Mechanisms

In the previous section, the reasons for the onset of plasma instabilities were discussed. This next section reviews two important gas discharge stabilization techniques which have been developed to prevent the onset of these instabilities; namely external ionization and magnetic stabilization.

1.5.1 External Ionization

External ionization, as a means of producing large volume glow discharges, represented a major improvement over self-sustained operation. The more important external ionization methods developed for high power CO_2 lasers are: electron beam preionization, photoionization and photo-plus-impulse ionization.

Electron beam preionization was first demonstrated by Fenstremacher, Nutter, Leland and Boyer[25] for a pulsed CO_2 TEA laser. A high energy electron beam (150 keV) was generated and injected into the interelectrode volume. The beam energy ionized the gas volume, and thereby provided a uniform and homogeneous background electron density; which greatly improved discharge stability and uniformity. The main shortcomings of this method of external ionization, are the difficulties associated with passing the high energy electron beam, from the vacuum chamber into the high pressure gas discharge volume.

In the photoionization method, the active volume is irradiated by ultraviolet (UV) radiation. The UV photoionizes some of the neutral particles, and a uniform background of electron density results. This external ionization technique was first applied to CO_2 TEA lasers by Seguin and Tulip[38] and Judd.[26] Seguin, Nam and Tulip[27,39] extended this technique for CW operation with the development of the 1 kW P.I.E. (Photoinitiated, Impulse-enhanced, Electrically excited) laser. This external ionization system featured a high repetition rate pulser, which produced 10 - 12 kV impulses, 200 nsec in width, having a repetition rate of up to 10 kHz.[28] These impulses were applied to both a UV spark source array and a multielement, fluid-ballasted cathode.[40] A much larger P.I.E. laser, with an output power of up to 20 kW has subsequently been developed for a variety of industrial applications.[2]

1.5.2 Magnetic Stabilization

Magnetic stabilization, developed at the University of Alberta by Seguin and Capjack[41], inhibits the development of glow-to-arc transitions through the use of magnetic fields of appropriate profile and strength. This stabilization method was first applied to the transverse discharge geometry pictured in Fig. 1.7. A discharge was struck between two planar, water cooled electrodes, with an interelectrode spacing of 5 cm. The electromagnet, positioned over the cathode, and whose magnetic field profile is shown in Fig. 1.8, provided a field that varied from 700 Gauss near the cathode surface to 90 Gauss near the anode. In operation, the transverse discharge current, J_z, interacts with the radial component of the magnetic field, B_r, to produce a Lorentz force on the charged species in the azimuthal direction. This results in a sheared rotation flow structure for both the charged and neutral species. A theoretical analysis by Capjack, Seguin and Antoniuk[42], which included the secondary flow effects, was done to study the azimuthal motion of the charge carriers, and their subsequent effect on the bulk gas. Their results showed that the peak azimuthal velocity, V_θ, of the bulk gas was 35 m/sec. Experimental analysis, showed that a specific power loading of 20 kW/ℓ was readily achievable and was restricted only by power supply limitations and not by a glow-to-arc transition.

Based on these encouraging results, this same magnetic stabilization scheme was applied to the coaxial discharge configuration, shown in Fig. 1.9. Two coaxial water-cooled electrodes were assembled, with the inner and outer electrodes being the anode and cathode respectively, and with the interelectrode gap being 3.6 cm. The required magnetic field, up to 600 Gauss in strength, was provided by a simple external solenoid. In operation, the radial current density, J_r, interacts with the axial magnetic field, B_z, thereby producing an azimuthal Lorentz force, F_θ, on the charged particles. Experiments showed that a specific power loading, up to 40 kW/ℓ was possible without glow-to-arc transitions, and as before this was a power supply limitation.[43]

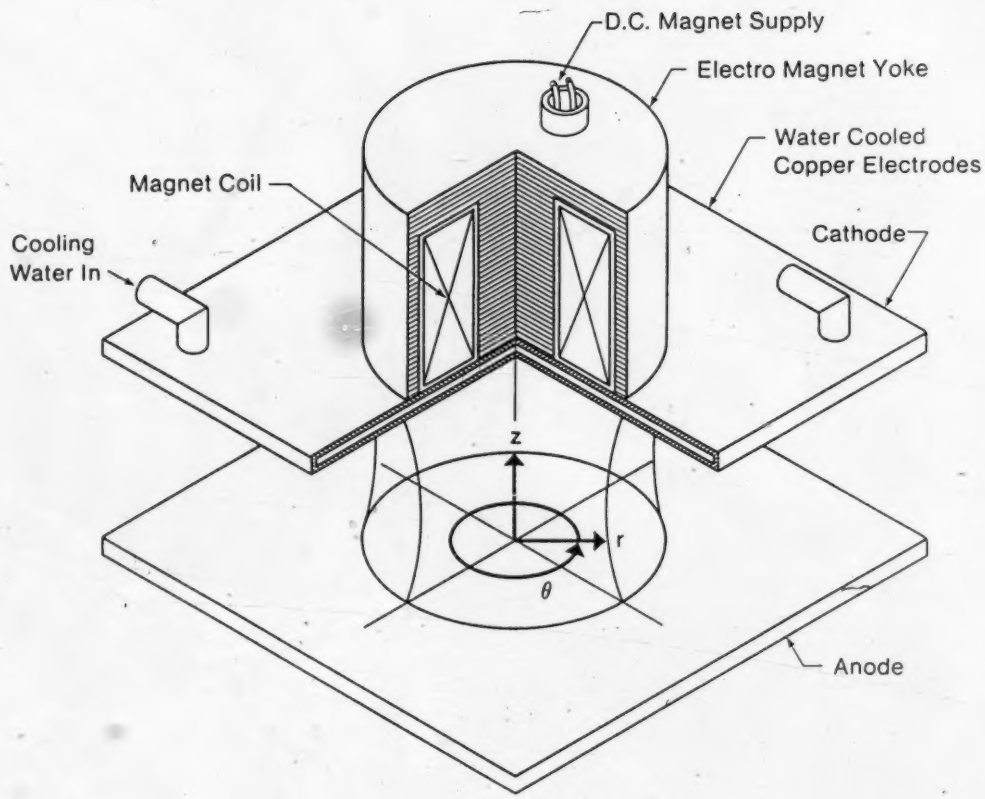

Fig. 1.7 Schematic of the Initial Magnetically Stabilized Transverse Gas Discharge[44]

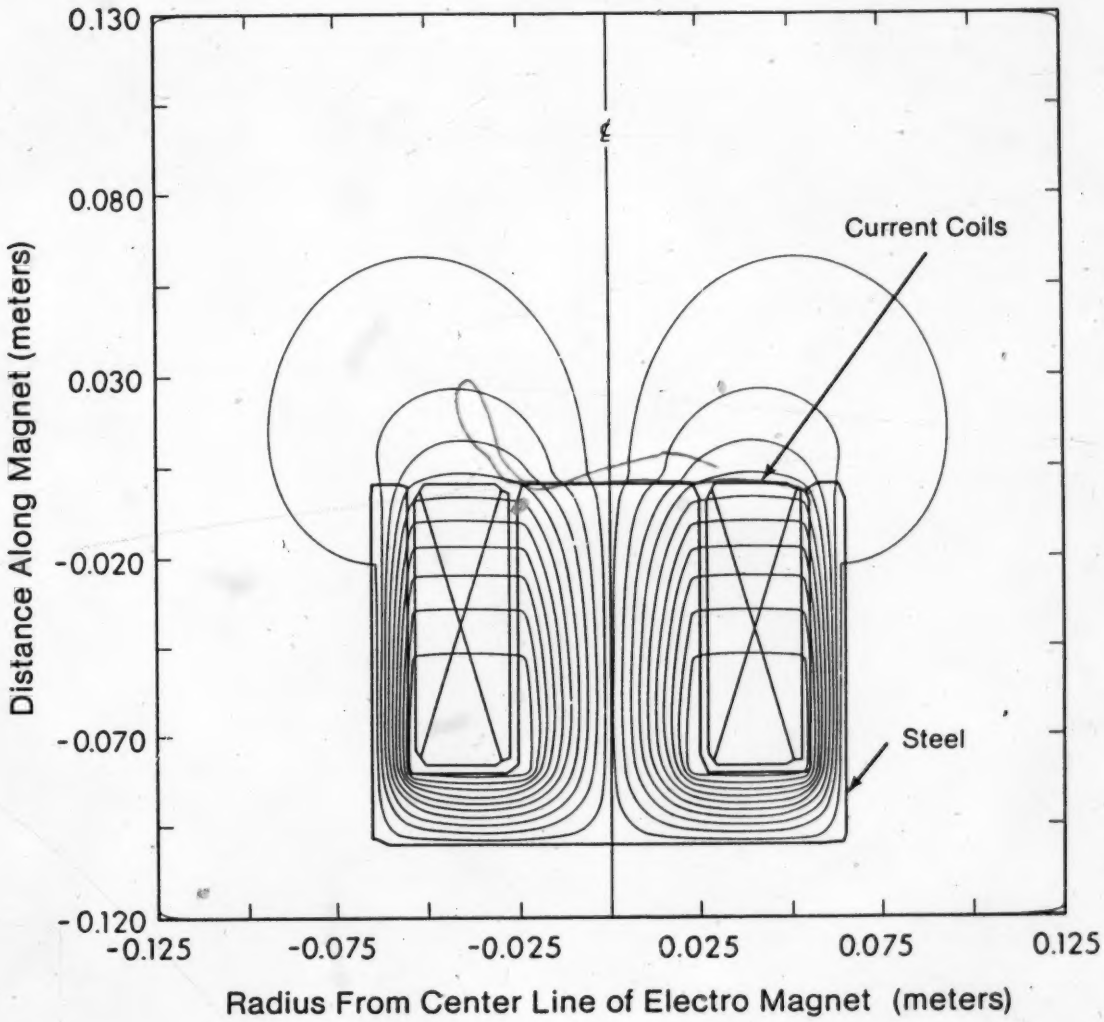

Fig. 1.8 Magnetic Field Profile of the Electromagnet shown in Fig. 1.7[44]

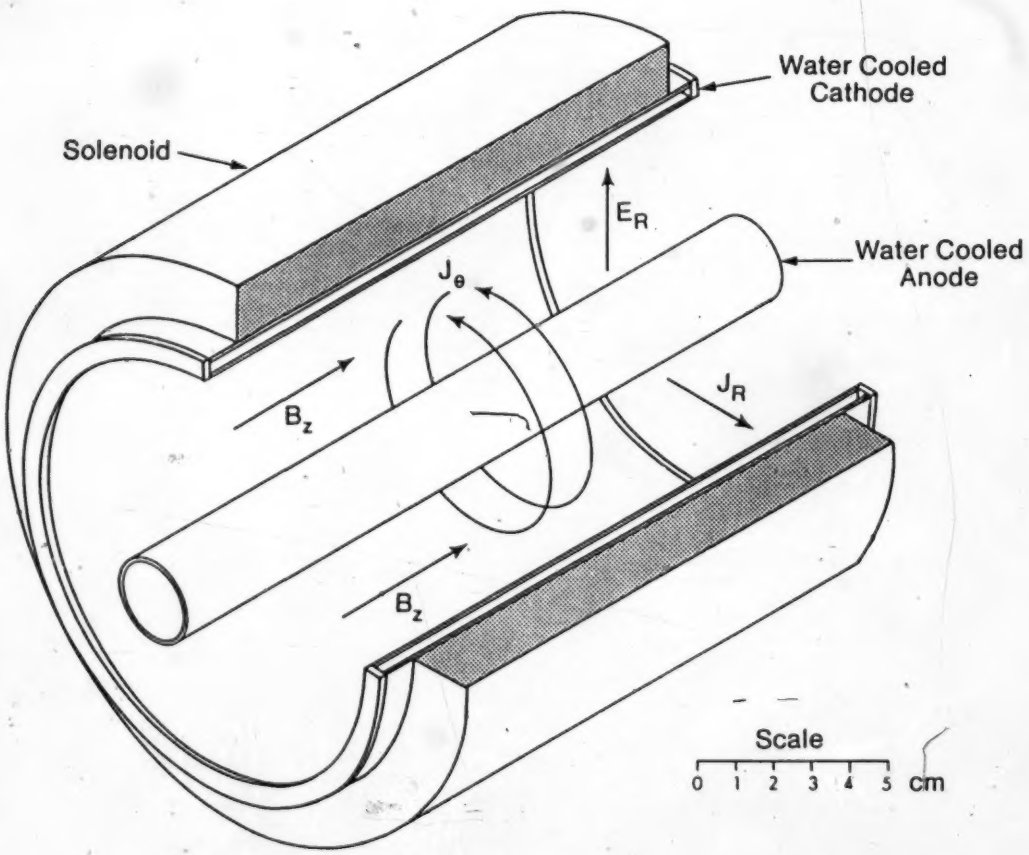

Fig. 1.9 Schematic of the Coaxial Magnetically Stabilized Gas Discharge[43]

A later theoretical analysis, by Razdan, Capjack and Seguin[45,46] examined the drift velocities of charged particles in a magnetized plasma, using a Monte Carlo simulation of the cathode fall region. Their results indicated that the primary stabilization mechanism, in effect for the transverse and coaxial discharges discussed previously, was a Lorentz driven charged particle mixing velocity at the cathode surface. Specifically, with a sufficient magnetic field strength, the induced transverse motion of the charge carriers is sufficiently rapid, such that their residence time, within a spatial region characteristic of the electrothermal instability (~1 cm), is less than the glow-to-arc transition time (~1 msec at 20 Torr). Consequently, these mixing velocities effectively "smooth out" any perturbations in electron density, thereby reducing the susceptibility to glow-to-arc instabilities.

1.6 Scope of this Thesis

The motivation of this investigation is to explore the feasibility of using the magnetic stabilization concept for a large bore (10 cm) axial discharge stabilized with a transverse rotating magnetic field. Preliminary work, done with a 25 cm long sealed discharge tube having a diameter of 10 cm, demonstrated that plasma self-constriction could indeed be prevented through the judicious choice of magnetic field strength. However, as will be subsequently reported, the stabilization mode for this axial discharge differs significantly from those of the previously discussed devices. The driven azimuthal velocity of the bulk gas is insignificant, and as such, gas cooling to the discharge wall is insufficient. Thus, in order to permit a complete study of this new stabilization method, the discharge tube, now 50 cm long, was mounted into a recirculating gas loop. An exhaustive series of diagnostic tests was performed, including an evaluation of the electron density. This was followed by a study of the axial gas discharge optical qualities, including a brief investigation of the laser output power.

CHAPTER II

THEORETICAL ANALYSIS

This chapter is separated into three sections. First is a brief discussion of the fundamental plasma parameters and how these are evaluated. The second topic addresses the question of bulk rotation, where the effect of the transverse rotating magnetic field on the neutral gas velocity is analyzed. Finally, a discussion of the Lorentz forces generated when an axial discharge interacts with a transverse magnetic field is presented.

2.1 Fundamental Plasma Parameters

The next few paragraphs present an introduction to the plasma parameters used for gas discharge analysis. Typical values for these parameters are given in tabular form. Magnetic field effects, if any, on these parameters are also discussed. Topics addressed are; collision frequency, viscosity, thermal conductivity, heat capacity, mobility, electrical conductivity, drift velocity, effective pressure and the ionization coefficient.

2.1.1 Collision Frequency

In general, the average collision frequency for momentum transfer between r and s particles, each with a Maxwellian velocity distribution, is given by:[47]

$$\langle \nu_{rs} \rangle = n_s Q_{rs} [\langle c_r \rangle^2 + \langle c_s \rangle^2]^{1/2} , \tag{2.1}$$

$$\text{where} \qquad \langle c_{r(s)} \rangle = \left[\frac{8 k_B T_{r(s)}}{\pi m_{r(s)}} \right]^{1/2} . \tag{2.2}$$

The quantities n_s, Q_{rs} and $\langle c_{r(s)} \rangle$ are the number density, collision cross-section and mean thermal speed respectively. $T_{r(s)}$, k_B and $m_{r(s)}$ are the temperature, Boltzmann constant and particle mass. The collision cross-section for heavy species, (ions and neutrals), may be approximated with:[47]

$$Q_{rs} = \pi(r_r + r_s)^2 = Q_{sr} \,. \tag{2.3}$$

where $r_{r(s)}$ are the molecular radii of the colliding species. Values of molecular radii for He, N_2, CO, and CO_2 are presented in Table 2.1. The calculated collision cross-sections between these species are given in Table 2.2.

The average collision cross-section for a gas mixture depends on the fractional composition of the individual gases.[47] For neutral particles, this becomes:

$$Q_{nn(mix)} = \sum_{i,j} f_i f_j Q_{ij} \,. \tag{2.4}$$

where $f_{i(j)}$ are the fractional compositions of the $i(j)^{th}$ gases. The average molecular weight for a gas mixture is given by:

$$m_{mix} = \sum_j \frac{f_j M_j}{N_a} \,, \tag{2.5}$$

where M_j is the molecular weight of the j^{th} species and N_a is Avogadro's number. Values of $Q_{nn(mix)}$ and m_{mix} are presented for several typical laser mixtures in Table 2.3.

Using Eqs. 2.4 and 2.5, the collision frequency for momentum transfer for the neutrals may be calculated using:

$$\langle \nu_{nn} \rangle = n_n Q_{nn(mix)} \left[\frac{16 k_B T_n}{\pi m_{mix}} \right]^{1/2} \,. \tag{2.6}$$

The accelerating electric field in the positive column of a gas discharge is small in comparison to the fields that exist in the cathode fall region.[48] For this reason, and also due to many ion-neutral collisions, the ion temperature remains relatively low. A reasonable approximation of the ion-neutral collision frequency results for $T_i \simeq T_n$; in which case, $\langle \nu_{in} \rangle \simeq \langle \nu_{nn} \rangle$.

The collision cross-section between electrons and neutral particles is a function of the electron temperature. Such information has been compiled.[11] An excerpt from a table of electron-neutral cross-sections, for a typical range of electron temperatures found in CO_2 laser gas discharges, is shown in Table 2.4.

Table 2.1 Molecular Radii and Masses of the Laser Gases

Gas	r(A)	mass(a.m.u.)
He	1.10	4.003
N_2	1.89	28.014
CO	1.90	28.010
CO_2	2.33	44.010

Table 2.2 Heavy Particle Collision Cross-Sections

r - s	$Q_{rs}(10^{-20}m^2)$
He - He	15.21
He - N_2	28.09
He - CO	28.27
He - CO_2	36.96
N_2 - N_2	44.89
N_2 - CO	45.13
N_2 - CO_2	55.95
CO - CO	45.36
CO - CO_2	56.21
CO_2 - CO_2	68.22

Table 2.3 Average Molecular Mass and Cross-Sections for Several Typical Laser Gas Mixtures

CO_2:CO:N_2:He	$Q_{nn(mix)}(10^{-20}m^2)$	$m_{mix}(10^{-26}kg)$
1 : 0 : 1 : 8	22.389	1.728
1 : 0 : 1 : 3	30.085	2.791
1 : 0 : 2 : 3	32.422	3.101
1 : 0 : 7 : 30	22.295	1.574
1 : 1 : 4 : 14	24.263	1.994

Table 2.4 Electron-Neutral Momentum Transfer Cross-Sections[11]

Energy(eV)	$Q_{e\text{-}He}(10^{-20}m^2)$	$Q_{e\text{-}N_2}(10^{-20}m^2)$	$Q_{e\text{-}CO_2}(10^{-20}m^2)$
0.5	6.59	9.95	7.70
0.7	6.73	9.98	6.30
1.0	6.85	9.98	5.60
1.2	6.91	10.51	5.20
1.3	6.92	11.00	5.10
1.5	6.96	11.96	5.00
1.7	6.97	13.43	5.00
1.9	6.98	19.83	5.10
2.1	6.98	26.38	5.30
2.2	6.98	28.76	5.40
2.5	6.96	29.60	6.50

For a gas mixture, the electron-neutral collision cross-section is given by:

$$Q_{en(mix)} = \sum_j f_j Q_{ej} , \tag{2.7}$$

where Q_{ej} is the collision cross-section for momentum transfer between the electrons and the j^{th} component of the gas mixture. Using Eq. 2.1, the electron-neutral collision frequency will be given by:

$$\langle \nu_{en} \rangle = n_n Q_{en(mix)} [\langle c_e \rangle^2 + \langle c_n \rangle^2]^{1/2} . \tag{2.8}$$

The mean thermal speed of the electrons is much greater than that of the neutrals. (See Eq. 2.2.) Thus, neglecting the neutral mean thermal speed and substituting for the electron mean thermal speed, the electron-neutral collision cross-section becomes:

$$\langle \nu_{en} \rangle \simeq n_n Q_{en(mix)} \left[\frac{8 k_B T_e}{\pi m_e} \right]^{1/2} . \tag{2.9}$$

The average collision frequency for an individual species is:

$$\langle \nu_r \rangle = \sum_s \langle \nu_{rs} \rangle . \tag{2.10}$$

For a weakly ionized plasma, $n_{e(i)} << n_n$. Thus, the collisions between neutrals and charged particles will be infrequent in comparison to those between neutrals. Hence:

$$\langle \nu_n \rangle = \langle \nu_{ni} \rangle + \langle \nu_{ne} \rangle + \langle \nu_{nn} \rangle \simeq \langle \nu_{nn} \rangle . \tag{2.11}$$

Similarly, the species collision frequency for a charged particle will be dominated by its collisions with the neutrals. Thus:

$$\langle \nu_i \rangle = \langle \nu_{in} \rangle + \langle \nu_{ie} \rangle + \langle \nu_{ii} \rangle \simeq \langle \nu_{in} \rangle , \text{ and} \tag{2.12}$$

$$\langle \nu_e \rangle = \langle \nu_{en} \rangle + \langle \nu_{ei} \rangle + \langle \nu_{ee} \rangle \simeq \langle \nu_{en} \rangle . \tag{2.13}$$

2.1.2 Viscosity and Thermal Conductivity

Viscosity is a macroscopic measure of the frictional and tangential forces involved in transmitting momentum in a fluid. For a gas consisting of a single species, the coefficient of shear viscosity is given by:[49]

$$\mu_s = \tfrac{1}{2} m_s n_s \langle c_s \rangle \ell_s \,, \tag{2.14}$$

where $\langle c_s \rangle$ is the mean thermal speed and $\ell_s = (2^{1/2} n_s Q_{ss})^{-1}$. The viscosity for a gas mixture is:[49]

$$\mu_{mix} = \sum_s \left[\frac{n_s}{\Sigma_r n_r M_{sr}} \right] \mu_s \,, \tag{2.15}$$

$$\text{where} \qquad M_{sr} = \frac{Q_{sr}}{Q_{ss}} \left[\frac{2m_{sr}}{m_s} \right]^{1/2} . \tag{2.16}$$

The reduced mass, m_{sr}, is given by:

$$m_{sr} = \frac{m_s m_r}{m_s + m_r} \,. \tag{2.17}$$

The thermal conductivity, λ_s, is a measure of how well the gas transmits heat. For a single species gas[49],

$$\lambda_s = \tfrac{15}{4} \mu_s \frac{k_B}{m_s} \left[\frac{9\gamma_s - 5}{15(\gamma_s - 1)} \right] \,. \tag{2.18}$$

where $\gamma_s = c_p / c_v$. c_p and c_v are the heat capacity at constant pressure and volume respectively. Values of γ_s for monatomic(He), diatomic(N_2 and CO), and polyatomic(CO_2) gases are 1.67, 1.4 and 1.3 respectively.[50]

For a mixture of gases, the thermal conductivity is:[49]

$$\lambda_{mix} = \sum_s \left[\frac{n_s}{\Sigma_r n_r M_{sr}} \right] \lambda_s \,. \tag{2.19}$$

Values of pure gas viscosity and thermal conductivity for He, N_2, CO and CO_2 are shown in Table 2.5. The viscosity and thermal conductivity for several CO_2 laser gas mixtures are presented in Table 2.6.

Table 2.5 Pure Gas Viscosities and Thermal Conductivities for He, N_2 and CO_2 (T = 150°C)

Gas	$\mu_s(10^{-6}kg/m\cdot s)$	$\lambda_s(kg\cdot m/s^3K)$
He	23.119	0.1801
N_2	20.717	0.0292
CO	20.498	0.0289
CO_2	17.086	0.0180

Table 2.6 Viscosity and Thermal Conductivity for Several Typical Laser Gas Mixes (T = 150°C)

CO_2:CO:N_2:He	$\mu_{mix}(10^{-6}kg/m\cdot s)$	$\lambda_{mix}(kg\cdot m/s^3K)$
1 : 0 : 1 : 8	22.602	0.11603
1 : 0 : 1 : 3	21.345	0.07821
1 : 0 : 2 : 3	21.297	0.06766
1 : 0 : 7 : 30	23.272	0.12012
1 : 1 : 4 : 14	22.789	0.10128

Eqs. 2.15 (and 2.19) show that the viscosity (and thermal conductivity) of a gas mixture is only dependent on the density ratios of its constituents. However, they are both independent of the gas density itself. Thus, the ability of a gas to transmit momentum and heat is not altered with a change in density. (The benefits of increased density are negated by a reduced mean free path between collisions. This is shown clearly in Eq. 2.14.)

2.1.3 Specific Heat Capacity

Specific heats, c_p and c_v, are thermodynamic properties that give the ratio of heat supplied to a unit mass of a substance, to its consequent rise in temperature. The constant volume specific heat, c_v, is less than the constant pressure specific heat, c_p, because in the latter, the gas is allowed to expand and do work on the system.

For pure gases, c_v and c_p are given by:[51]

$$c_v = \frac{R}{m}\frac{1}{\gamma - 1}, \tag{2.20}$$

$$c_p = \frac{R}{m}\frac{\gamma}{\gamma - 1}, \tag{2.21}$$

where R is the universal gas constant ($R = k_B N_a = 8.3144$ J/mole-K), m is the mass in kg/mole and $\gamma = c_p/c_v$ is found in tables.[51] Values of c_v and c_p for He, N_2, CO and CO_2 are shown in Table 2.7.

The specific heat capacities for a laser gas mixture have been shown to be:[52]

$$c_v = R\frac{\Sigma_i(\gamma_i - 1)^{-1} f_i}{\Sigma_i m_i f_i}, \text{ and} \tag{2.22}$$

$$c_p = R\frac{\Sigma_i \gamma_i(\gamma_i - 1)^{-1} f_i}{\Sigma_i m_i f_i}, \tag{2.23}$$

where f_i is the fractional concentration of the i^{th} species. Values of c_v and c_p for several gas mixtures are presented in Table 2.8.

Table 2.7 Specific Heat Capacity for He, N_2, CO and CO_2

Gas	γ	c_v(J/kg-K)	c_p(J/kg-K)
He	1.668	3109	5186
N_2	1.403	736	1033
CO	1.402	738	1035
CO_2	1.303	624	812

Table 2.8 Specific Heat Capacities for Several Typical Laser Gas Mixtures

CO_2:CO:N_2:He	c_v(J/kg-K)	c_p(J/kg-K)
1 : 0 : 1 : 8	1419	2218
1 : 0 : 1 : 3	1016	1511
1 : 0 : 2 : 3	946	1392
1 : 0 : 7 : 30	1513	2391
1 : 1 : 4 : 14	1270	1962

2.1.4 Mobility and Electrical Conductivity

Mobility is a measure of a charged particle's ability to travel through a background medium. The background medium, for the partially ionized gas mixtures typical of CO_2 laser discharges, is simply the predominantly neutral gas. In the absence of a magnetic field, the electrical mobility of a charged particle is given by:

$$\kappa_s = \frac{q_s}{m_s \nu_s} , \tag{2.24}$$

where q_s, m_s and ν_s are the charge, mass and collision frequency of the species respectively. The ratio of ion mobility to electron mobility is:

$$\frac{\kappa_i}{\kappa_e} = \frac{m_e \nu_e}{m_i \nu_i} << 1 . \tag{2.25}$$

Hence, ion mobility may be neglected when compared to electron mobility.[53]

Electrical conductivity, σ, is related to mobility by:

$$\sigma = n_i q_i \kappa_i + n_e q_e \kappa_e . \tag{2.26}$$

For a neutral plasma, $n_i = n_e$, and for singly charged ions $|q_i| = |q_e|$. Because κ_e is much greater that κ_i, electrical conductivity of a gas discharge is dominated by the electrons, and so:

$$\sigma \simeq n_e q_e \kappa_e . \tag{2.27}$$

In the presence of a magnetic field the electron mobility, κ_e, is a function of magnetic field. Thus, using $\kappa_{||}$, $\kappa_\perp$ and κ_T to represent the parallel, Pedersen and Hall mobilities, one finds that:[54]

$$\kappa_{||} = \kappa_0 = \frac{q_e}{m_e \nu_{en}} , \tag{2.28}$$

$$\kappa_\perp = \kappa_0 \frac{\nu_{en}^2}{\nu_{en}^2 + \omega_{ce}^2} = \kappa_0 \frac{1}{1 + \beta_e^2} , \tag{2.29}$$

$$\kappa_T = \kappa_0 \frac{\omega_{ce} \nu_{en}}{\nu_{en}^2 + \omega_{ce}^2} = \kappa_0 \frac{\beta_e}{1 + \beta_e^2} , \tag{2.30}$$

where $\omega_{ce} = eB/m_e$ (electron cyclotron frequency); $\beta_e = \omega_{ce}/\nu_{en}$ (electron Hall parameter); $\kappa_{||}$ is the electron mobility parallel to the magnetic field; $\kappa_\perp$ is the electron mobility parallel to the electric field, and perpendicular to the magnetic field; κ_T is the mobility perpendicular to both the electric and magnetic fields.

The parameter of most interest, in this context, is the Pedersen mobility, $\kappa_\perp$, which is the axial mobility down the discharge tube. It is clearly a function of the magnetic field strength, B, and the collision frequency, ν_{en}. A low magnetic field strength results in a small Hall parameter, β_e, in which case $\kappa_\perp \simeq \kappa_0$. With a high magnetic field, β_e is large and electron motion along the electric field is restricted. The electrons are "tied" to the magnetic field lines, and $\kappa_\perp$ is greatly reduced.

Electron mobility is shown as a function of collision frequency in Fig. 2.1. At low pressures, where collisions are infrequent, the Hall parameter is large, and $\kappa_\perp$ is therefore small. Again, this is due to the electrons being trapped by the magnetic field. For high pressures and therefore high collision frequencies, the Hall parameter is small, but so is κ_0. Thus, $\kappa_\perp$ is again greatly reduced.

As is revealed in Fig. 2.1, the Pedersen mobility, $\kappa_\perp$, is a peaked function of collision frequency. The maximum value is found by differentiating Eq. 2.29 and setting the result to zero. The solution is $\nu_{en} = \omega_{ce}$, and thus the maximum Pedersen mobility becomes:

$$\kappa_{\perp max} = \frac{q_e}{2m_e\omega_{ce}} = \frac{1}{2B} . \qquad (2.31)$$

Fig. 2.1 shows that Pedersen mobility, $\kappa_\perp$, is a function of collision frequency, ν_{en}. If the collision frequency is in turn a function of radius in the discharge tube, then the judicious choice of magnetic field strength may allow for any desired radial mobility profile.

Experiments have shown that, with zero magnetic field, the discharge establishes itself on the centerline of the discharge tube. Naturally, this promotes a centrally accentuated temperature profile. As a consequence, a hotter and lower density region is invariably created on the tube axis. More current then flows into this highly conductive region, and this regenerative process leads to thermal instabilities, as was shown in section 1.4.2.

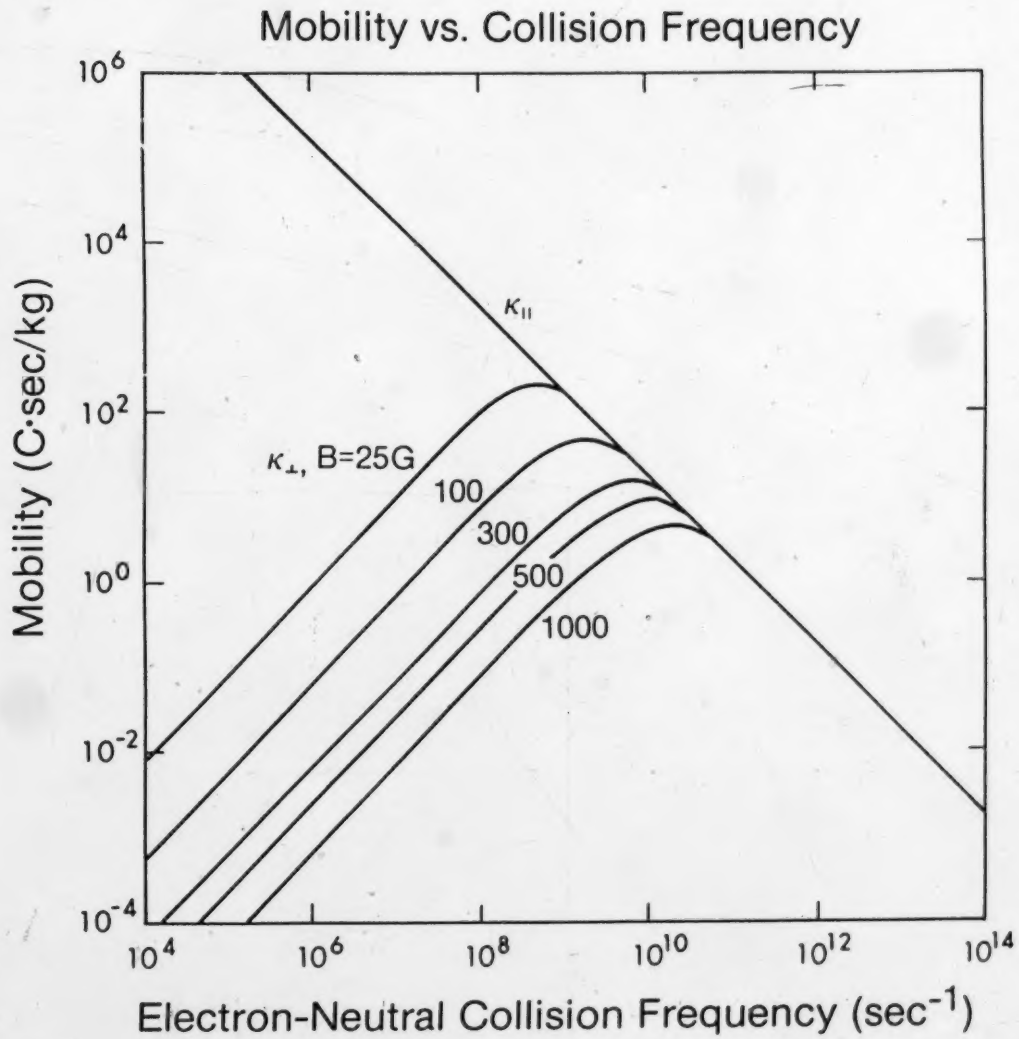

Fig. 2.1 Electron Mobility vs. Collision Frequency: Effect of Magnetic Field

Temperature measurements in section 4.2 show that the use of a magnetic field does not change the fact that the temperature profile is centrally accentuated. A good approximation to the experimental conditions is given by the relation:

$$T(r) = T_{wall} + (T_{axis} - T_{wall})J_0(2.405\ r/R)\ , \qquad (2.32)$$

where T_{wall}, T_{axis}, J_0, r and R are the temperature at the wall, centerline temperature, Bessel function of the first kind, radius and maximum tube radius respectively. With an input power of 3 kW, and gas flow of 10 m/sec, the condition midway between the anode and cathode, is given by T_{wall} = 150°C and T_{axis} = 350°C. This temperature profile is shown in Fig. 2.2.

With the temperature profile in Fig. 2.2, the electron-neutral collision frequency becomes a function of radius; as do the Hall parameter, β_e, and the free-field electron mobility, κ_0. The resultant axial electron mobility profile is shown in Fig. 2.3. With no applied magnetic field, $\kappa_\perp = \kappa_0$, and the mobility is maximum on axis where the gas temperature is highest. Because the mobility is maximum on axis the gas discharge establishes itself down the centerline of the discharge tube. With the application of the magnetic field, the mobility everywhere is decreased. At a field of 50 Gauss/Torr, the mobility profile is seen to flatten out. At this magnetic field, all regions of the cross-section become equally attractive for current flow. This magnetic field value corresponds to the condition that β_e is ~1. A further increase in the magnetic field strength results in a mobility profile that is inverted from the case with no magnetic field. Fig. 2.3 also reveals that as the pressure is increased, the magnetic field required for an inversion in electron mobility also increases.

2.1.5 Effective Pressure

The application of the magnetic field causes the electron to gyrate around the magnetic field lines.[53] This makes it more difficult for the electrons to travel between the electrodes, and accounts for the reduced mobility (and therefore also a reduced drift velocity) as discussed in section 2.1.4. With a longer time in transit between the electrodes, the electrons undergo more inelastic collisions. This is similar to the effect of a pressure increase;

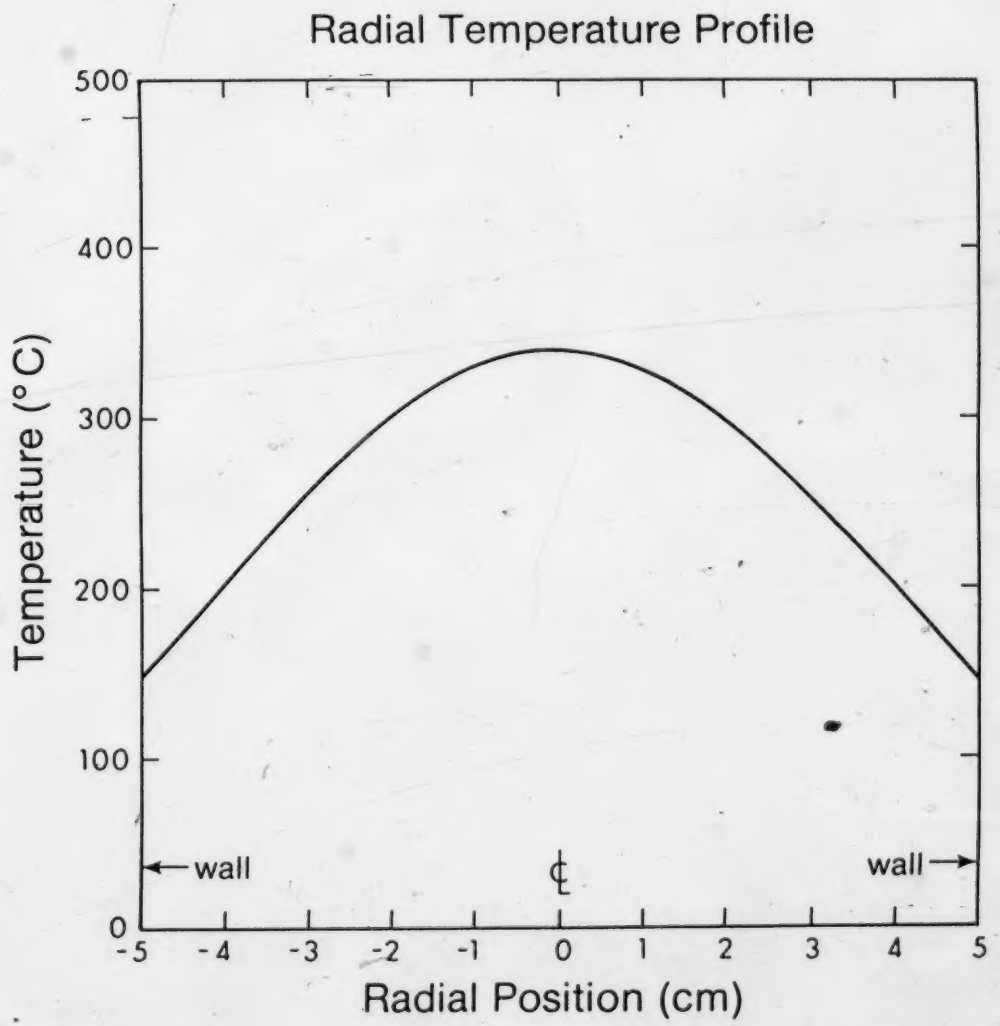

Fig. 2.2 Radial Temperature Profile

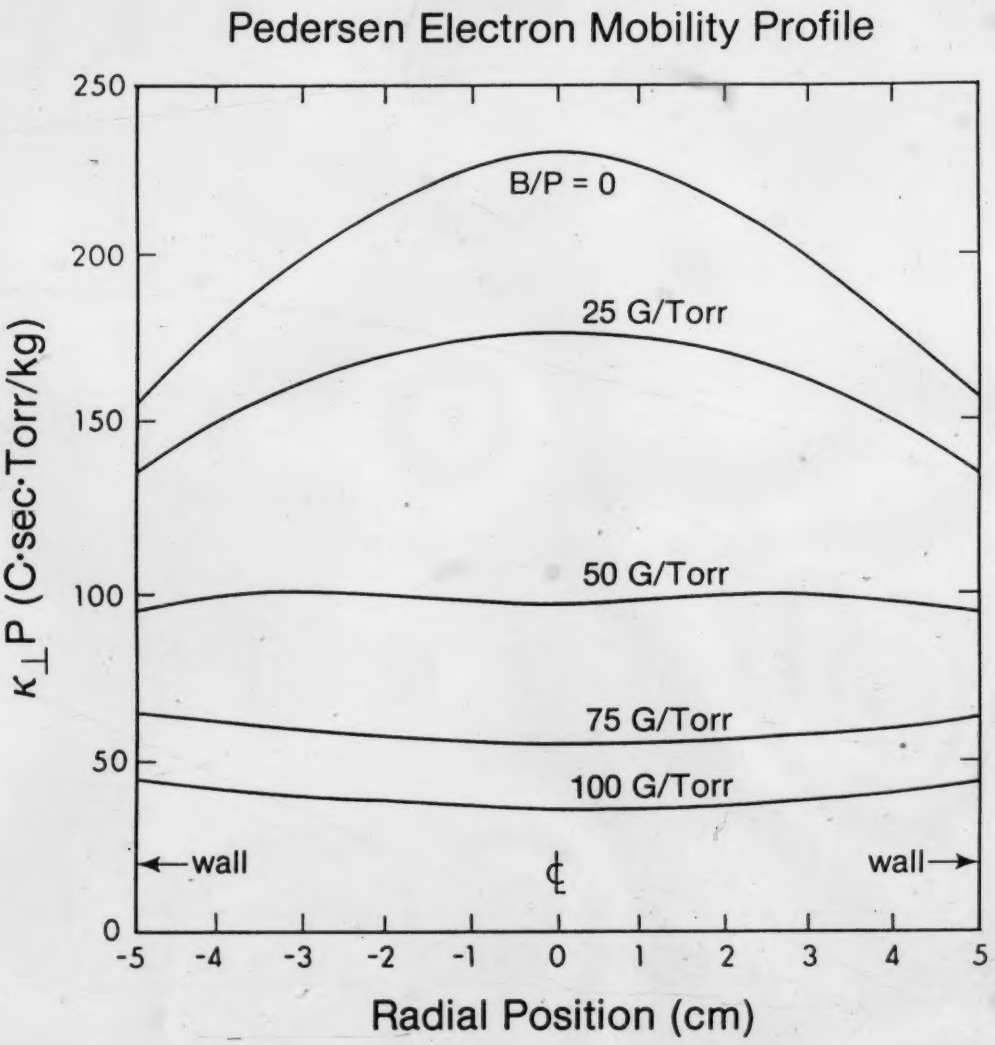

Fig. 2.3 Spatial Variation of Pedersen Electron Mobility vs. Magnetic Field

hence the term "effective pressure".

Blevin and Haydon[55] established that under the influence of a transverse magnetic field, a gas discharge behaves as though only an electric field is present and the pressure has increased from p to p', where

$$p' = p\{1 + (\omega_{ce}/\nu_{en})^2\}^{1/2} . \tag{2.33}$$

Bernstein[56] has verified this experimentally for $20 \leq E/p \leq 150$ V/cm-Torr and for Hall parameters $0 \leq \beta_e \leq 25$.

The concept of effective pressure plays a role in parameters that are a function of E/p (or E/N). As an example, the percentage of power delivered to the upper laser level is a function of E/N. This will be discussed further in section 5.1. Another example is the Townsend ionization coefficient which is discussed below.

2.1.6 Townsend's First Ionization Coefficient

The source of electrons in a gas discharge is ionization of the gas molecules. The number of electrons produced by collisions with neutral molecules, as they travel from cathode to anode, is of vital importance when predicting whether the discharge will require external ionization or be self-sustained.

The number of electrons produced per unit length, in the direction of the electric field, is known as the ionization coefficient or Townsend's first ionization coefficient, α, and is given by:

$$\alpha/p = A \exp(-Bp/E) . \tag{2.34}$$

The coefficients A and B are constants dependent on gas mixture.[48] With an applied magnetic field, p is replaced with p'. Upon substitution:

$$\alpha/p = A\{1 + (\omega_{ce}/\nu_{en})^2\}^{1/2} \exp\left[\frac{-Bp}{E}\{1 + (\omega_{ce}/\nu_{en})^2\}^{1/2}\right] . \tag{2.35}$$

This reveals that α is reduced with the application of a magnetic field. This effect has been experimentally verified.[56] Thus, if a constant voltage is maintained across the discharge, the number of ionizations by electron collision, α, will decrease with the application of the transverse magnetic field. A lower current density results if no external ionization is present.

2.2 Bulk Rotation

Previous investigations, discussed in section 1.5.2, demonstrated that the use of crossed electric and magnetic static fields could be used to produce a sheared velocity flow structure in the bulk gas (neutrals) of a transverse gas discharge.[41,44,42] These stabilizing mixing velocities proved effective in the suppression of electrothermal instabilities. This section describes a theoretical investigation that was undertaken to determine if the transverse rotating magnetic field applied to the axial discharge would also generate these stabilizing mixing velocities.

The study of bulk rotation begins with an analysis of the single fluid magnetohydrodynamic equation. This is given by:[57,58]

$$\frac{\partial}{\partial t}(\rho\vec{V}) + \vec{\nabla}\cdot(\rho\vec{V}\vec{V}) + \vec{\nabla}\cdot\hat{\Pi} = \vec{J} \times \vec{B} , \tag{2.36}$$

where ρ, $\vec{V}$, $\hat{\Pi}$, $\vec{J}$ and $\vec{B}$ are the mass density, average velocity, pressure tensor, current density and magnetic field respectively. The pressure tensor in terms of the pressure, P, and a viscous stress tensor, $\hat{\tau}$, is given by:

$$\hat{\Pi} = \hat{\tau} + P\hat{I} , \tag{2.37}$$

where $\hat{I}$ is the unit tensor. The viscous stress tensor, $\hat{\tau}$, is a measure of the frictional and tangential interactions resulting during momentum transfer in a fluid. In vector notation,

$$\hat{\tau} = -\mu(\vec{\nabla}\vec{V} + (\vec{\nabla}\vec{V})^{T}) + (\tfrac{2}{3}\mu - \xi)(\vec{\nabla}\cdot\vec{V})\hat{I} , \tag{2.38}$$

where μ and ξ are the shear and bulk viscosities. Shear viscosity was discussed in section 2.1.2. Bulk viscosity is concerned with the internal state of the gas molecules, and is zero for

a monatomic gas and small for polyatomic gases.[58] $(\vec{\nabla}\vec{V})^T$ is the transpose of the dyadic $\vec{\nabla}\vec{V}$, as defined by Morse and Feshbach.[59]

The quantity of interest is the azimuthal gas velocity as a function of radius. After considerable substitution, the θ-component of the momentum equation, given in Eq. 2.36 becomes:

$$\frac{\partial}{\partial t}(\rho V_\theta) + \frac{1}{r}\left[\frac{\partial}{\partial r}(r\rho V_r V_\theta) + \frac{\partial}{\partial \theta}(\rho V_\theta^2) + \frac{\partial}{\partial z}(r\rho V_\theta V_z) + \rho V_r V_\theta\right] + \frac{1}{r}\frac{\partial P}{\partial \theta}$$
$$- \frac{\mu}{r}\left[\frac{\partial}{\partial r}\left[r\frac{\partial V_\theta}{\partial r}\right] + \frac{\partial}{\partial \theta}\left[\frac{1}{r}\frac{\partial V_\theta}{\partial \theta} + \frac{V_\theta}{r}\right] + \frac{\partial}{\partial z}\left[r\frac{\partial V_\theta}{\partial z}\right] + \frac{1}{r}\frac{\partial V_r}{\partial \theta} - \frac{V_\theta}{r}\right]$$
$$- (\zeta + \tfrac{1}{3}\mu)\frac{1}{r}\frac{\partial}{\partial \theta}\left[\frac{1}{r}\left[\frac{\partial}{\partial r}(rV_r) + \frac{\partial V_\theta}{\partial \theta} + \frac{\partial}{\partial z}(rV_z)\right]\right]$$
$$= (\vec{J} \times \vec{B})_\theta . \qquad (2.39)$$

Thankfully, the following assumptions may be made to reduce this to a manageable form; A steady state solution is sought, so $\frac{\partial}{\partial t} = 0$. The azimuthal velocity, V_θ, is assumed to be a function of r, but not of θ. The driving force is uniform over a large region in z. Thus, there are no secondary flows in the r-z directions, and the dependence in z may be removed. Also, since the plasma is contained by the discharge tube walls, $V_r = 0$. With these assumptions, Eq. 2.39 reduces to:

$$-\mu\left[\frac{\partial^2 V_\theta}{\partial r^2} + \frac{1}{r}\frac{\partial V_\theta}{\partial r} - \frac{V_\theta}{r^2}\right] = J_z B_r - J_r B_z . \qquad (2.40)$$

The applied transverse rotating magnetic field may be characterized by the following:

$$B_r = B_\omega \cos(\omega t - \theta) , \qquad (2.41)$$
$$B_\theta = B_\omega \sin(\omega t - \theta) , \qquad (2.42)$$
$$B_z = 0 , \qquad (2.43)$$

where B_ω is the field strength of the transverse rotating field and ω is the angular velocity. The rotating field is provided by a two-pole induction motor stator, hence, the rotating field has angular velocity of 120π radians/sec (3600 RPM).

In the analysis of the gas discharge, it is important to know if the applied magnetic field is distorted by the plasma column. This is determined by an analysis of the magnetic Reynolds number; R_m, which is the ratio of induced to total magnetic induction. When $R_m << 1$, the magnetic field penetrates the medium completely, and the magnetic field lines are not distorted. Any induced magnetic fields generated are negligible compared with the imposed fields. However, if $R_m >> 1$, the magnetic field lines are distorted by the induced fields.[60,61] As $R_m \rightarrow \infty$, as for a perfect conductor, the magnetic field lines are incapable of penetrating the medium.

The magnetic Reynolds number is given by:[49]

$$R_m = \mu_0 \sigma V L \, , \tag{2.44}$$

where μ_0, σ, V and L are the magnetic permeability of free space, electrical conductivity, velocity of the gas and a scale length. For this analysis the scale length, L, is the maximum tube radius, R. The maximum possible angular velocity is ωR. With these substitutions, the magnetic Reynolds number becomes:

$$R_m = \mu_0 \sigma (\omega R) R \, . \tag{2.45}$$

For a 20 Torr pressure and a magnetic field strength of 500 Gauss, the mobility down the centerline of the discharge tube is 8 C-sec/kg (from Fig. 2.3). The electron density is estimated to be $3.5(10)^{18}$ m^{-3} from Fig. 4.27. Thus, the electrical conductivity ($\sigma = n_e q_e \kappa_e$), is 4.48 C^2-sec/kg-m^3. With the angular velocity, $\omega = 120\pi$ radians/sec and the maximum tube radius of 0.05 m, the magnetic Reynolds number, R_m, is $5.3(10)^{-6}$. Thus, we may conclude that the magnetic field lines are not distorted by the plasma, and that any induced magnetic fields are small compared to the imposed fields.

As a consequence of the time varying nature of the magnetic field, an axial electric field is induced. Faraday's Law states that:

$$\vec{\nabla} \times \vec{E} = -\frac{\partial \vec{B}}{\partial t} \, . \tag{2.46}$$

With the assumption that $\vec{E}$ has no variation in z, Eq. 2.46 expands into:

$$(\vec{\nabla} \times \vec{E})_r = \frac{1}{r}\frac{\partial E_z}{\partial \theta} = -[-\omega B_\omega \sin(\omega t - \theta)] \text{ , and} \tag{2.47}$$

$$(\vec{\nabla} \times \vec{E})_\theta = -\frac{\partial E_z}{\partial r} = -[\omega B_\omega \cos(\omega t - \theta)] . \tag{2.48}$$

The solution of these two equations is:

$$E_{z(AC)} = r\omega B_\omega \cos(\omega t - \theta) = r\omega B_r . \tag{2.49}$$

where the subscript AC is added to differentiate this induced electric field from the applied electric field, which shall be refered to as $E_{z(DC)}$. The total electric field is therefore given by:

$$E_z = E_{z(DC)} + E_{z(AC)} . \tag{2.50}$$

The final step in the solution of Eq. 2.40 is to derive an expression for J_z. (Since $B_z = 0$, the second term, $J_r B_z$, is eliminated.) This is found by using the generalized Ohm's law for a plasma in a magnetic field. Neglecting the ion slip and electron pressure gradient terms, this is given by:[47]

$$\vec{J} = \hat{\sigma} \cdot (\vec{E} + \vec{V} \times \vec{B}) . \tag{2.51}$$

With the same assumptions as those used with the momentum equation (Eq. 2.39), the z-component of Eq. 2.51 is:

$$J_z = \sigma_\perp (E_z - V_\theta B_r) , \tag{2.52}$$

where $\sigma_\perp$ is the Pedersen conductivity, which (using Eqs. 2.27 and 2.29) may be written as:

$$\sigma_\perp = n_e q_e \kappa_\perp . \tag{2.53}$$

Thus, the azimuthal force is found to be:

$$F_\theta = J_z B_r = \sigma_\perp (E_z - V_\theta B_r) B_r . \tag{2.54}$$

Substituting for E_z from Eqs. 2.49 and 2.50, yields:

$$F_\theta = \sigma_\perp(E_{z(DC)} + r\omega B_r - V_\theta B_r)B_r \text{ , or} \tag{2.55}$$

$$F_\theta = \sigma_\perp E_{z(DC)}B_r + \sigma_\perp(r\omega - V_\theta)B_r^2 \text{ .} \tag{2.56}$$

Further substitution for B_r, gives:

$$F_\theta = \sigma_\perp E_{z(DC)}B_\omega\cos(\omega t - \theta) + \sigma_\perp(r\omega - V_\theta)B_\omega^2\cos^2(\omega t - \theta) \text{ .} \tag{2.57}$$

At this point, it is important to realize that F_θ is still a function of θ. To derive an average azimuthal force, it is necessary to integrate Eq. 2.57 over 2π radians. Upon doing so, the first term vanishes. Thus the DC applied electric field does not contribute to azimuthal motion. It is only the AC induced electric field interacting with the rotating magnetic field that results in an azimuthal force on the plasma. We are then left with:

$$F_{\theta(av)} = \tfrac{1}{2}\sigma_\perp(r\omega - V_\theta)B_\omega^2 \text{ .} \tag{2.58}$$

Finally, the momentum equation may be completed by substituting for $F_{\theta(av)}$ in Eq. 2.40 to yield, with some manipulation:

$$\frac{\partial^2 V_\theta}{\partial r^2} + \frac{1}{r}\frac{\partial V_\theta}{\partial r} - \frac{V_\theta}{r^2} = \frac{\sigma_\perp}{2\mu}(V_\theta - r\omega)B_\omega^2 \text{ .} \tag{2.59}$$

At this point it is desirable to switch to dimensionless variables, in order to have the momentum equation as a function of the Hartmann number, which is the ratio of the $\vec{J} \times \vec{B}$ force to the viscous force. The following substitutions are made:

$$\eta = \frac{r}{R} \qquad\qquad v_\theta = \frac{V_\theta}{\omega R} \tag{2.60}$$

With these substitutions, the momentum equation becomes:

$$\frac{\partial^2 v_\theta}{\partial \eta^2} + \frac{1}{\eta}\frac{\partial v_\theta}{\partial \eta} - \frac{v_\theta}{\eta^2} = \tfrac{1}{2}H_a^2(v_\theta - \eta) \text{ ,}$$

$$\text{where } H_a = \left[\frac{\sigma_\perp}{\mu}\right]^{1/2} B_\omega R \text{ .} \tag{2.61}$$

This equation may be solved by making the substitution:

$$v_\theta' = v_\theta - \eta \,. \tag{2.62}$$

Eq. 2.61 is then transformed into:

$$\frac{\partial^2 v_\theta'}{\partial \eta^2} + \frac{1}{\eta}\frac{\partial v_\theta'}{\partial \eta} - \frac{v_\theta'}{\eta^2} = \tfrac{1}{2}H_a{}^2 v_\theta' \,. \tag{2.63}$$

which can be rearranged further to give:

$$\frac{\partial^2 v_\theta'}{\partial \eta^2} + \frac{1}{\eta}\frac{\partial v_\theta'}{\partial \eta} - \left[\tfrac{1}{2}H_a{}^2 + \frac{1}{\eta^2}\right] v_\theta' = 0 \,. \tag{2.64}$$

which is a homogeneous modified Bessel differential equation.[62] The boundary conditions assumed for this system are that the azimuthal velocity at the tube axis and at the tube wall is zero. That is: $v_\theta(\eta=0) = v_\theta(\eta=1) = 0$. These boundary conditions, for the primed variables, become: $v_\theta'(\eta=0) = 0$, and $v_\theta'(\eta=1) = -1$. Eq. 2.64 has as its solution:

$$v_\theta' = -\frac{I_1(H_a\eta/\sqrt{2})}{I_1(H_a/\sqrt{2})} \,, \text{ and so:} \tag{2.65}$$

$$v_\theta = \eta - \frac{I_1(H_a\eta/\sqrt{2})}{I_1(H_a/\sqrt{2})} \,. \tag{2.66}$$

where I_1 is the modified Bessel function. This function is plotted in Fig. 2.4 for a range of Hartmann numbers between 1 and 50. This shows that as the Hartmann number increases, more of the neutral gas in the discharge is being spun up. For high values of H_a, the neutrals move at synchronous speed.

Unfortunately, this is not the situation at hand. For a 20 Torr gas mixture (1:1:4:14), the viscosity, μ, is $22.789(10)^{-6}$ kg/m-sec. The conductivity (as derived for Eq. 2.45) is 4.48 C^2-sec/kg-m^{-3}. With the tube radius of 0.05 m and the maximum magnetic field available being 450 Gauss, the Hartmann number (Eq. 2.61), is only ~1. At this low Hartmann number, the maximum generated azimuthal velocity results at $\eta=0.6$ (r=3 cm), where $v_\theta=0.023$. When multiplied by ωR, this corresponds to a mixing velocity, V_θ, of only 0.4 m/sec. Thus, we may conclude that without a significant increase in magnetic field

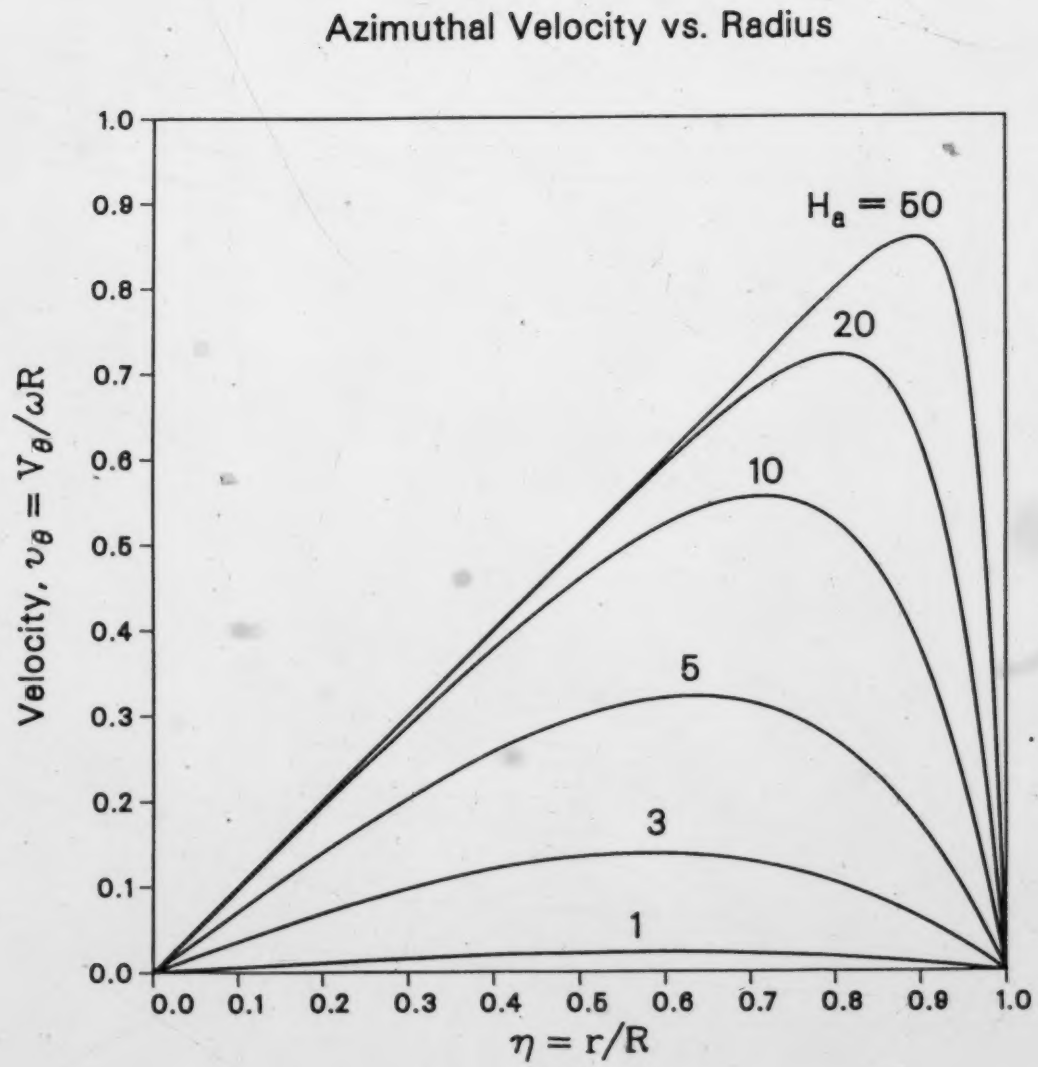

Fig. 2.4 Azimuthal Velocity vs. Radius: Hartmann Number

strength, very little azimuthal rotation of the neutral gas is expected.

2.3 Lorentz Force on the Plasma Column

Initial observations suggested that the magnetic field forced the discharge to assume a much larger cross-sectional area, than is the natural tendency.[63] However, high speed photography revealed that the plasma column is in fact deflected away from the centerline position when the transverse rotating magnetic field is applied. Consequently, as the magnetic field rotates, the plasma column sweeps across the tube cross-section at the same angular velocity as the impressed magnetic field. An analysis of the Lorentz force responsible for this plasma column deflection will now be presented.

Consider the expression for F_θ, derived in the discussion of bulk rotation, and re-written below:

$$F_\theta = \sigma_\perp E_{z(DC)} B_\omega \cos(\omega t - \theta) + \sigma_\perp (r\omega - V_\theta) B_\omega^2 \cos^2(\omega t - \theta) . \tag{2.67}$$

A similar procedure as used in the derivation of F_θ may be used to derive F_r:

$$- F_r = J_z B_\theta = \sigma_\perp E_{z(DC)} B_\omega \sin(\omega t - \theta) + \sigma_\perp (r\omega - V_\theta) B_\omega^2 \cos(\omega t - \theta)\sin(\omega t - \theta) . \tag{2.68}$$

The ratio, A, of the second term to the first, for both F_θ and F_r is:

$$A = \frac{N}{D} = \frac{(r\omega - V_\theta) B_\omega \cos(\omega t - \theta)}{E_{z(DC)}} . \tag{2.69}$$

The results presented in the discussion of bulk rotation showed that $V_\theta \sim 0$, and so the maximum value that the numerator, N, can have is $R\omega B_\omega$; which is ~0.85 V/m. Typically, the denominator, D, is 2500 V/m. (See Eq. 5.4.) Thus, the first term in both Eqs. 2.67 and 2.68 is much larger than the second. Hence, F_θ and F_r may be approximated by:

$$F_\theta \simeq \sigma_\perp E_{z(DC)} B_\omega \cos(\omega t - \theta) , \text{ and} \tag{2.70}$$

$$- F_r \simeq \sigma_\perp E_{z(DC)} B_\omega \sin(\omega t - \theta) . \tag{2.71}$$

The magnitude of the total transverse force may then be written:

$$F_T = \left[F_\theta^2 + F_r^2\right]^{1/2} = \sigma_\perp E_{z(DC)} B_\omega = n_e q_e \kappa_\perp E_{z(DC)} B_\omega \,. \tag{2.72}$$

Upon substituting for $\kappa_\perp$ and B_ω, (by recognizing that $\beta_e = q_e B_\omega / m_e \nu_{en}$), F_T may be written as:

$$F_T = n_e q_e \frac{\beta_e}{1 + \beta_e^2} E_{z(DC)} \,. \tag{2.73}$$

By differentiating Eq. 2.73, it may be shown that F_T has its maximum when $\beta_e = 1$. For $\beta_e < 1$, F_T is an increasing function of magnetic field. Hence, the radius of rotation of the plasma column is an increasing function of magnetic field strength. If $\beta_e > 1$, F_T is a decreasing function of magnetic field. Physically, this phenomena may be explained as follows: Recall that the Lorentz force is a function of the axial drift velocity of the electrons from cathode to anode. The axial drift velocity is a function of Pedersen mobility, which was discussed in section 2.1.4, and was shown to be a decreasing function of magnetic field. However, when the Pedersen mobility, $\kappa_\perp$, is multiplied by the magnetic field strength, B_ω, as in Eq. 2.72, this product is an increasing function of magnetic field for $\beta_e < 1$. Thus, the decrease in axial mobility, $\kappa_\perp$, is more than compensated for by the magnetic field multiplier; consequently, F_T increases with magnetic field strength. Conversely, when $\beta_e > 1$, the decrease in axial mobility, $\kappa_\perp$, is not fully compensated for by the magnetic field multiplier and F_T is then a decreasing function of magnetic field strength.

During experiments under low pressure (3.5 Torr) conditions, a magnetic field of 175 Gauss resulted in what appeared to be a donut shaped annular discharge. High speed photography revealed that this was in fact an azimuthally rotating plasma column forced off the tube axis. Increasing the magnetic field to 250 Gauss caused the discharge to quench on the discharge tube walls. These phenomena are depicted in Fig. 2.5, which shows the effect of magnetic field on the gas discharge radius as it appears to the naked eye. The radial boundaries were not as clear as suggested by Fig. 2.5, but were simply extrapolated from a series of photographs.

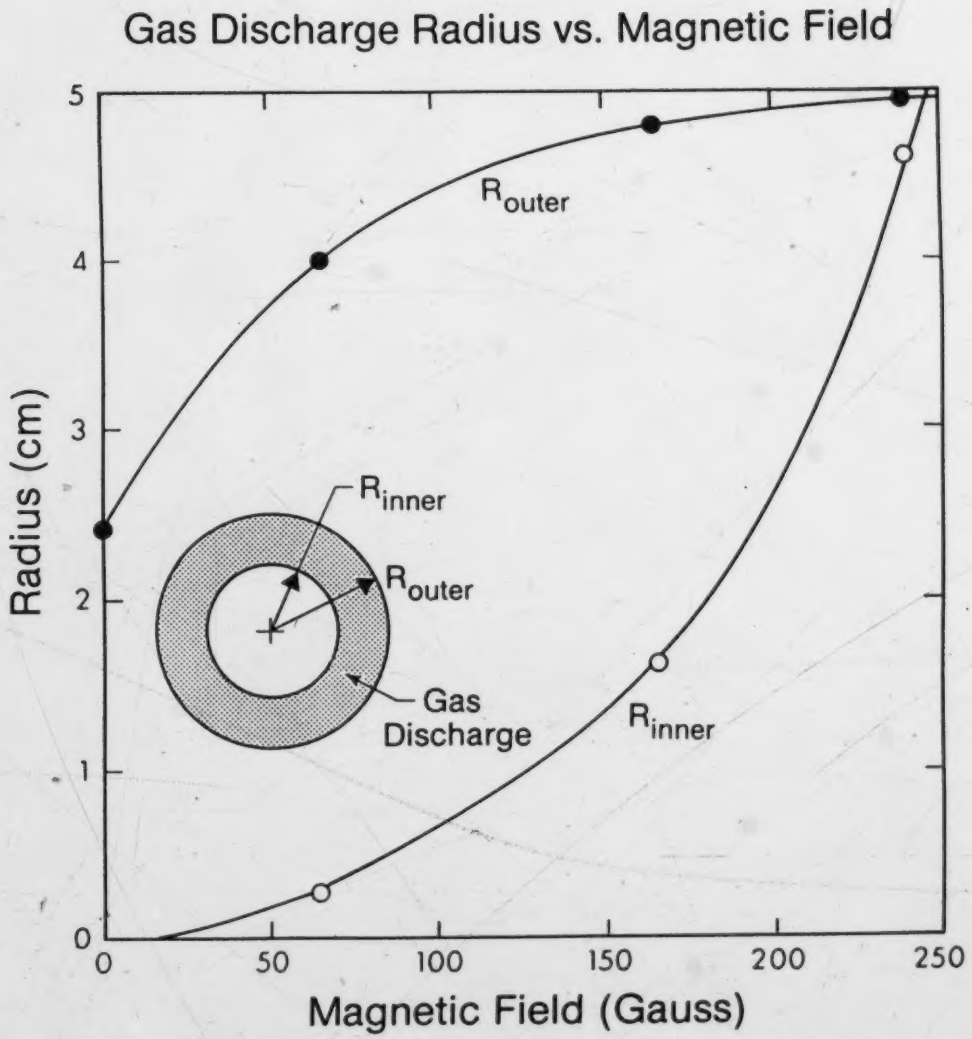

Fig. 2.5 Effect of Magnetic Field on the Apparent Radial Boundary of the Gas Discharge at Low Pressure (3.5 Torr)

Experiments at high pressure (20 Torr) showed that with the magnetic field strength available (450 Gauss), the "annular" discharge could not be demonstrated, nor could the discharge be extinguished by forcing the plasma into the wall. However, this magnetic field was of sufficient strength to force the plasma column away from the tube centerline. A qualitative explanation for the degree of plasma deflection, resulting when the magnetic field is applied, is as follows. The electric field causes a drift of electrons from cathode to anode. When these electrons pass through the transverse magnetic field, they are deflected away from the tube centerline by a Lorentz ($\vec{J} \times \vec{B}$) force, in a direction mutually orthogonal to both the electric and magnetic fields. Thus, the maximum charged particle concentration is located off-axis. However, the electron mobility is still greatest on axis (see Fig. 2.3, 25 G/Torr), and in the absence of this Lorentz force, space charge effects would certainly force the current to become concentrated on the tube bore. Consequently, the final radial position of the plasma is a balance between (i) the natural tendency of the plasma to travel along the highest electron mobility path (on axis), and (ii) the magnetic force which is deflecting the electrons away from the tube axis; thereby reducing the on-axis conductivity ($n_e q_e \kappa_e$). Because the magnetic force is an increasing function of magnetic field strength (see Eq. 2.72), the radial position where the peak plasma conductivity occurs, and thus where the plasma is established, is also an increasing function of magnetic field strength. As will be shown in Chapter 4, this magnetically induced deflection allows for up to a 25% increase in useful power loading into the plasma. In Chapter 5, the implications of these effects on the gain characteristics will be discussed.

CHAPTER III

SYSTEM DESIGN

The initial experiments were conducted with a 25 cm long gas discharge system having no external gas flow. This resulted in the generation of high gas temperatures, unsuitable for lasing; since, as was shown in section 2.2, the Lorentz forces generated negligible flow in the bulk gas. Consequently, an expanded system, that incorporated convective gas cooling, was necessary. The components of this expanded system, in which a recirculating gas loop is used, are shown in Fig. 3.1. The apparatus consists of six major subsections: a vacuum system, gas transport system, rotating magnetic field supply, electrodes, thyratron pulser, and a DC sustainer supply. An expanded view of the magnetized gas discharge test section is shown in Fig. 3.2.

3.1 Vacuum System

The recirculating gas system is constructed of 6 inch diameter aluminum pipe with a 1/8 inch wall thickness. The fan housing is 12 inches in diameter and the heat exchanger housing is fabricated from aluminum channel. Joints are sealed with 1/8 inch O-ring sealed flanges.

The test section consists of two parts. The first is simply an acrylic tube, 6 inches in diameter, with a wall thickness of 1/4 inch. This was necessary to provide electrical isolation for the "hot" electrode in the center of the test section. The second is a double wall, water cooled channel. The outer channel is constructed of $5\frac{1}{2}$ inch diameter acrylic tubing with a 1/4 inch wall. The inner channel is 110mm(4.3in) glass tubing with 6mm(.24in) walls. This left a gap of 0.85cm(.34in) between the tubes through which water was flowed to help cool the discharge, as well as to dissipate any thermal gradients in the glass tube. Delrin was used in the construction of the electrode supports, which will be discussed separately.

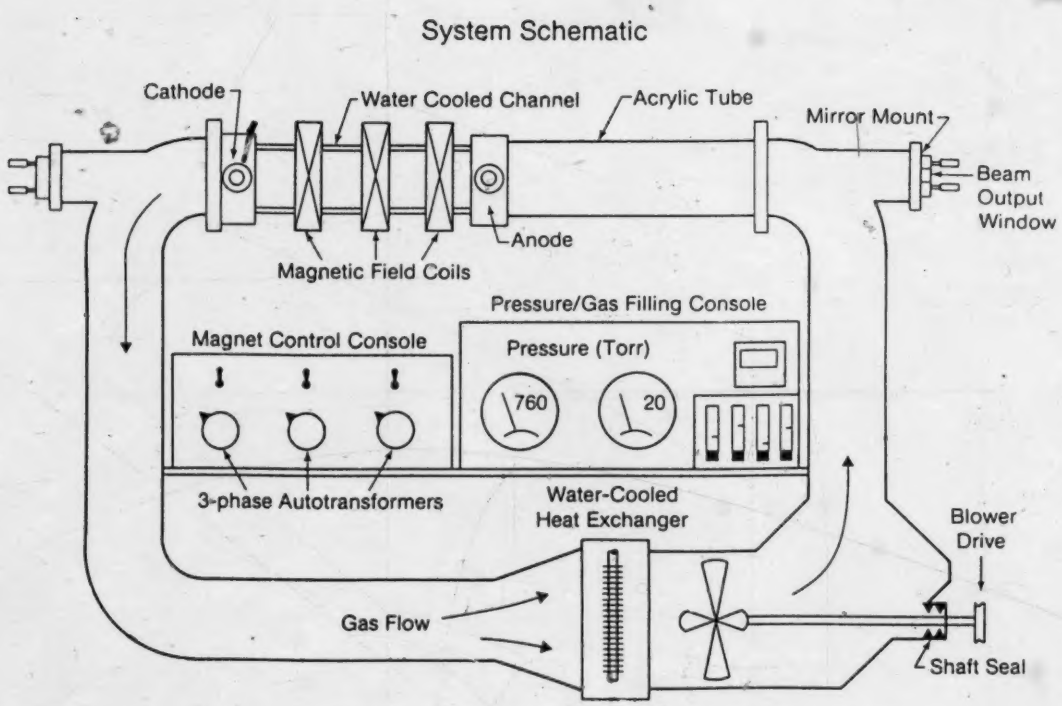

Fig. 3.1 Schematic of System

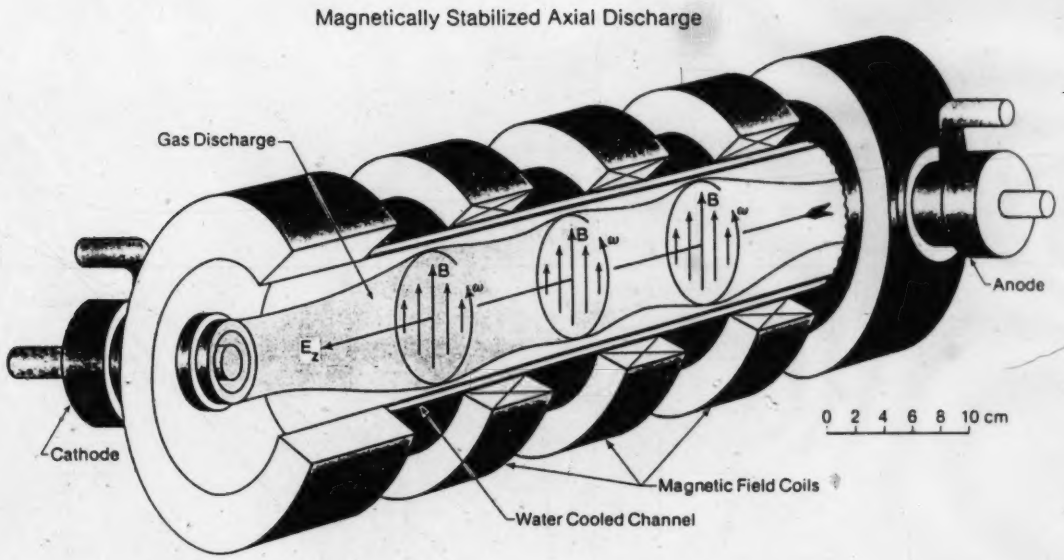

Fig. 3.2 Detail of the Gas Discharge Test Section

Vacuum vessel evacuation prior to backfilling, is achieved with a Welch rotary mechanical pump, having a pumping speed of 500 litres/min. Pumpdown time from atmospheric pressure to 0.1 Torr was 7 to 8 minutes. After several hours of pumping, to allow for outgassing of materials, the lowest attainable pressure was $6(10)^{-3}$ Torr.

Contamination due to leaks is of major concern; since even small quantities of impurities, such as molecular oxygen, from the air can adversly affect the discharge parameters.[20] To determine the leak rate, the system is pumped out and sealed off. The pressure rise is then observed over a period of time. The leak rate is subsequently calculated using the formula:

$$\text{leak rate} = V\frac{\Delta P}{\Delta T}, \tag{3.1}$$

where V is the system volume (180 litres), ΔP and ΔT are the changes in pressure and time respectively. System pressure was observed to rise from $6(10)^{-3}$ to $550(10)^{-3}$ Torr over a period of 20 hours. This corresponds to a leak rate of 5.0 ℓ-Torr/hr. Thus, the system has good vacuum integrity. Over a typical run of 10 minutes, the pressure rise due to leaking is only $4.6(10)^{-3}$ Torr.

3.2 Gas Transport System

In order to provide full flexibility in parameter measurement, a variable gas flow feature was designed into the gas transport system. The principle components of this system are; the motor drive and controller, the shaft seal, and the blower. The simplest method to vary the blower speed was the use of a universal motor with a triac speed controller. A Robbins & Myers 1.25 horsepower, 230 VAC series wound universal motor was selected. Using a simple full-wave triac controller, the motor speed ranged between ~1000 and 6000 rpm.

Since the fan is mounted inside the system, while the motor is external, a shaft seal was required to transfer power to the blower unit. A Volvo hydraulic motor seal with a 1 inch diameter shaft, was utilized for this purpose, and is rated for a top speed of 10,000 rpm. Fan

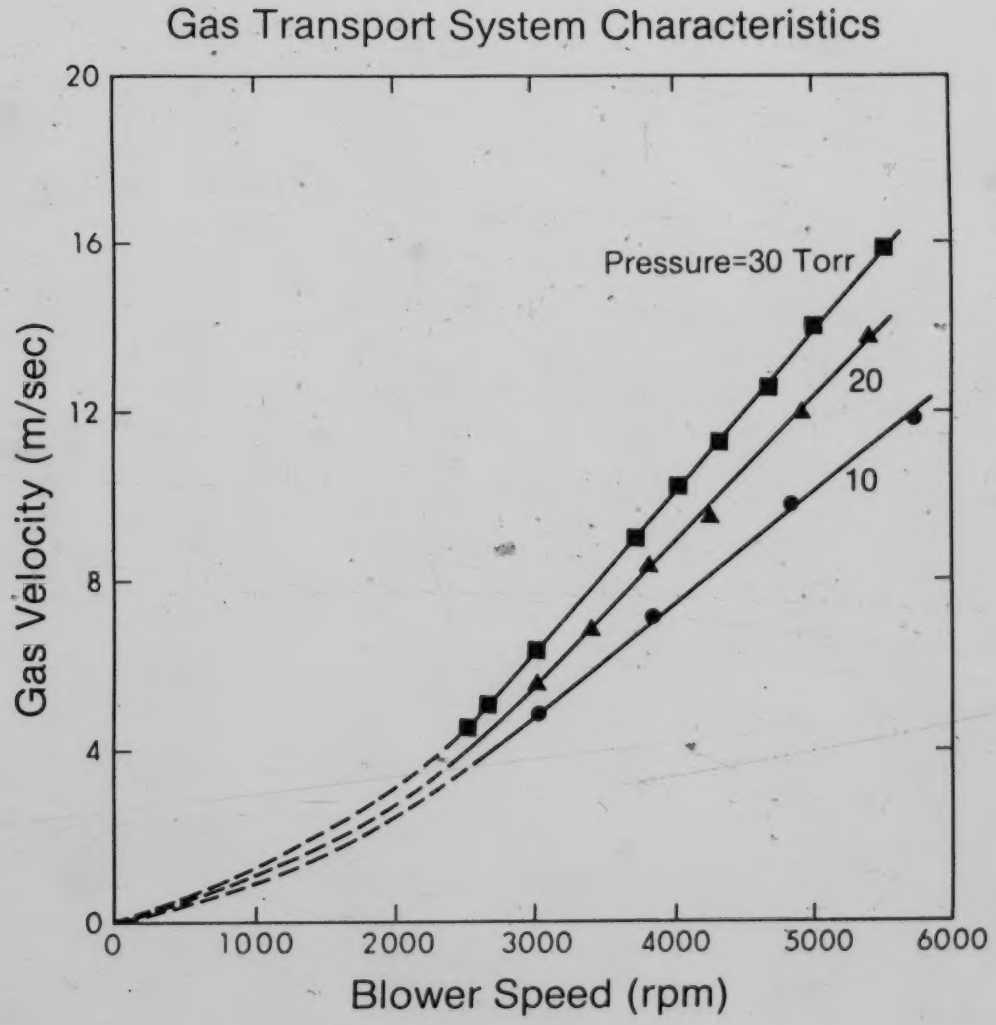

Fig. 3.3 Axial Gas Flow Velocity vs. RPM

shaft drive was accomplished via a 1:1 pulley system with a Polyflex V-belt. Blower speed was monitored with an electro-optic tachometer.

A single stage blower was employed to circulate the gas. The 12 inch diameter fan is comprised of 10 injection molded blades mounted with a 45° pitch angle. Blade clearance between the blade tips and the blower housing was ~1/4 inch.

Evaluation of the gas transport system performance, involved measurements of the gas flow velocities, on axis in the system test section, using a straight pitot tube. The pressure differential was monitored with a capacitance manometer (Datametrics Model 1400). Flow velocities were observed for a typical laser gas mixture (1:1:8) for 10, 20 and 30 Torr total pressure. These observations are presented in Fig. 3.3. A brief study was also made of the radial variation in flow velocity within the test section. The pitot tube was mounted at a radial position midway between the wall and the axis of the test section. Flow velocities so observed were similar to those measured on axis. This feature is characteristic of a fully developed turbulent flow.

3.3 Magnetic Field Supply and Characteristics

The rotating magnetic field was provided by means of three separate modules, as shown in Figs. 3.1 and 3.2. Each module is a three phase, two pole winding similar to that used for an induction motor stator. Because the plasma generates negligible back emf, the magnets were wound with AWG 22 copper wire so as to increase the inductance of each coil. This allowed a larger number of turns to be used than would be possible with the usual winding of AWG 17 or 18. Consequently, a high voltage winding, rather than high current, was obtained, thereby permitting easy magnetic field control with a three phase autotransformer.

It was of paramount importance for an appropriate analysis, that the strength of the rotating field, as well as its distribution be known. Thus, a Sprague UGN-3501T linear output Hall effect sensor was mounted on an adjustable probe, in order to study the features of the rotating magnetic field profile in detail. This Sprague sensor has a sensitivity of 700mV per

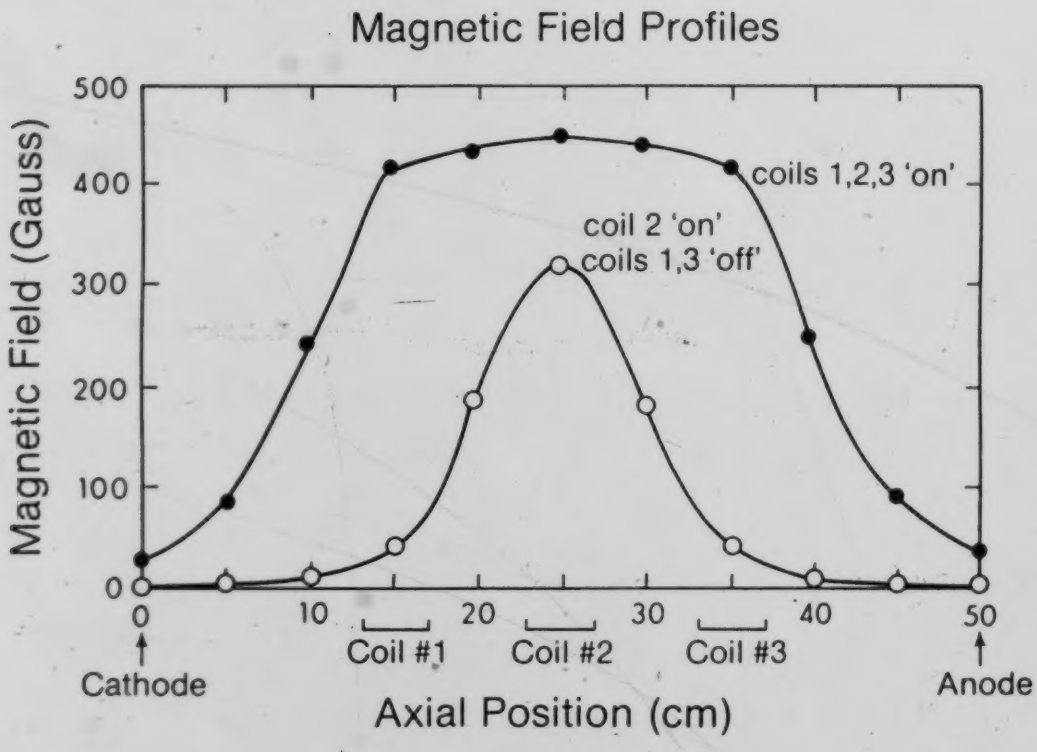

Fig. 3.4 Transverse Magnetic Field Strength Profiles

1000 Gauss of magnetic field. Because the sensor is only sensitive to perpendicular fields, the 3600 rpm rotating magnetic field generates a periodic (60 Hz) waveform at the sensor output. Sensor output was monitored with an oscilloscope, to record the peak magnetic field values. A digital AC voltmeter was used to record the RMS voltage output.

Measurements were made at 35 separate locations, with the probe kept in a horizontal orientation. (Five radial measurements of magnetic field strength were taken at seven axial positions.) These radial measurements confirmed that the magnetic field was relatively uniform across the diameter. Thus, for a given axial position, the transverse magnetic field was found to be essentially uniform throughout the discharge region. The two modules on either side were also energized, to extend the region of influence of the center magnetic module. However, in order for the fields to interact constructively, it was necessary that these side coils have the proper direction of rotation as well as the correct phase orientation. This was confirmed by oscilloscope traces; showing a good sine wave when the coils were properly oriented. In this manner, a nearly uniform transverse rotating magnetic field could be imposed over a 20 cm length of the gas discharge. The maximum magnetic field so obtained, when all three coils are energized, was approximately 450 Gauss. At this magnetic field strength, the total power consumption of the magnetic field structure was 5.7 kW; 1.9 kW per coil. The transverse magnetic field strength profile, measured as a function of axial position, is shown in Fig. 3.4.

3.4 Electrode Design

Four different electrode structures were developed and tested, during the course of this investigation. The first three, shown in Fig. 3.5, are the ring electrode, coaxial pin electrode, and the segmented tube electrode. Each was developed as an improvement on the former. The fourth and final electrode structure is the button electrode, shown in Fig. 3.6. All of these electrode structures have the fluid ballast concept incorporated into their design. This ballast feature took the form of an internal recirculating electrolytic solution comprised of Potassium Carbonate (K_2CO_3) and water. In operation, these ballasting fluid gaps

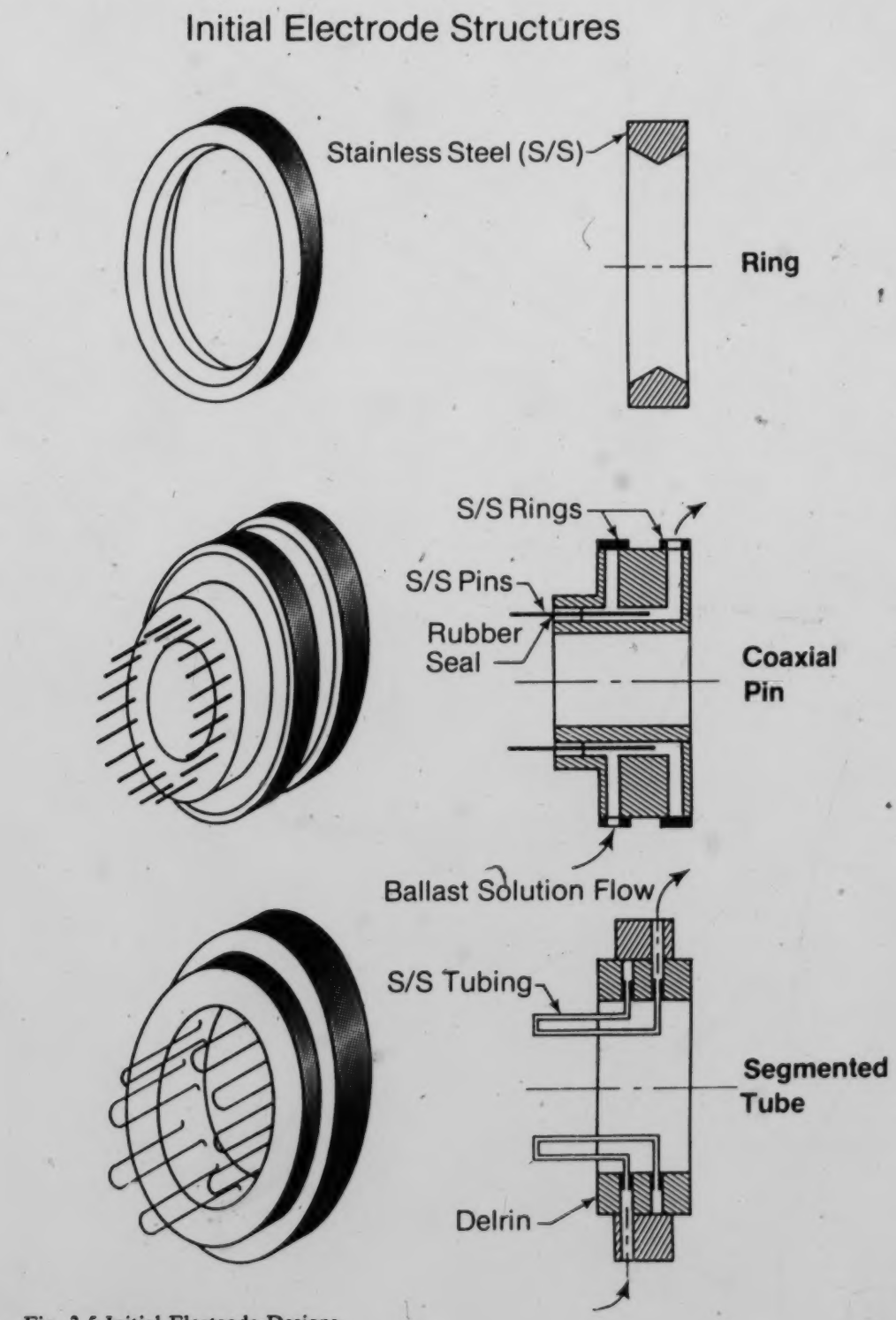

Fig. 3.5 Initial Electrode Designs

balanced the current fed to each sub-electrode ring, pin or tube. This fluid ballast technique, developed within the University of Alberta's laser laboratory[40,64] overcomes many of the disadvantages inherent in using discrete resistors as ballast elements. This technique further provides a cooling feature as a consequence of flowing cooled ballasting solution through the electrode structure.

The stainless steel ring electrode was constructed with a ridge on the inner diameter, so as to constrain the plasma away from the edges of the device. The major shortcoming of this design was that the plasma established itself on one point of the electrode and remained fixed. This resulted in localized overheating and subsequent failure of the seals at the edges of the structure.

The coaxial pin electrode spread the discharge effectively. However, the stainless steel pins were insufficiently cooled and the pin ends would glow red at only moderate currents. Again, this resulted in a failure around the seals on the pins.

In an attempt to cool the segmented type electrode more effectively, tubes with cool ballast solution running through them were employed. These devices worked well until air locks developed in the tubes; thereby blocking the fluid flow, and leading to individual tubes overheating.

All of the previous three electrode structures were tested with a short discharge length of only 20 cm. When the flowing gas transport system was developed, the test section was increased to 50 cm in length. This feature permitted electrode phenomena to be separated from the magnetic field phenomena of interest. With this change in the experimental system, it was found that a segmented electrode was no longer effective. This is because the discharge tended to constrict to the axis of the discharge tube, regardless of electrode structure. For this reason, a single button electrode was developed, both for the anode and cathode structures.

From the experience gained with the initial designs, a number of design criteria are now known. Firstly, the electrode must be adequately cooled. Secondly, all O-ring seals must be positioned sufficiently removed from the discharge area, in order to prevent premature failure, due to melting. Thirdly, the electrode housing must be adequately protected from the

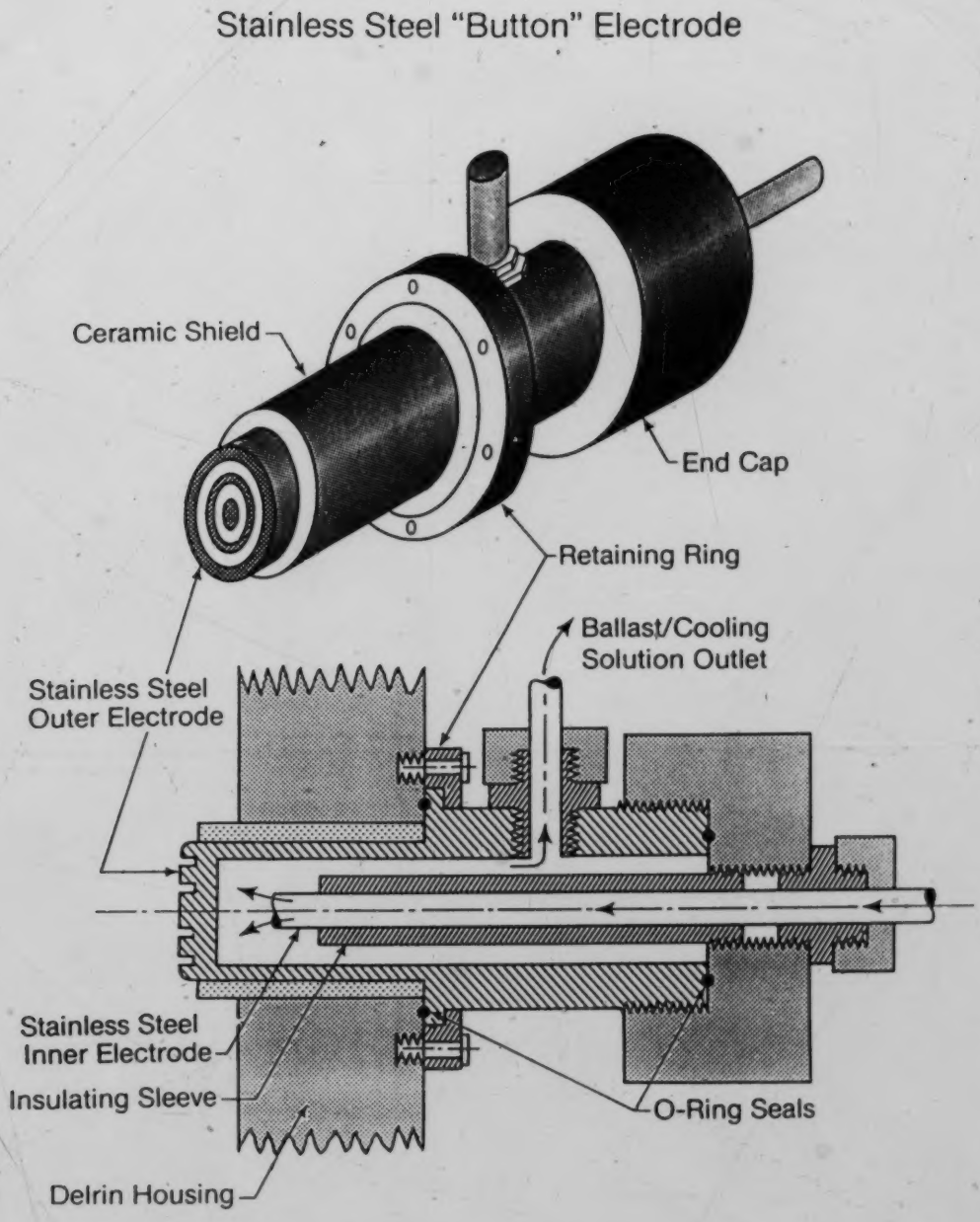

Fig. 3.6 Button Electrode Structure

plasma and its heating effects.

The button cartridge electrode configuration developed and shown in Fig. 3.6, ultimately met all of these design criteria. Cooled ballast solution is forced directly to the end of the electrode so as to ensure maximum cooling. All O-ring seals are far removed from the discharge region and confined to an area of the electrode system that always remains cool. An added bonus provided by the design is that there are no seals between the vacuum and fluid ballast systems. Protection for the electrode housing is provided by means of a ceramic sleeve between the button cartridge electrode and the electrode housing. Hollow cathode grooves were incorporated into the cathode button structure, so as to improve performance.[65] The development of this hollow cathode button electrode proved to be a significant improvement over the initial designs and has been demonstrated to be both rugged and dependable.

3.5 Thyratron Pulser Ionization System

The desirable features afforded by the use of external ionization were discussed in section 1.5.1. A thyratron pulser pre-ionization source was added to the present system for one additional reason; this being that the breakdown voltages needed for the 50 cm long discharge at 20 Torr operating pressure exceeded the normal operating limits of the DC power supply.

The pulser ionization system, which generates impulses up to 20 kV in amplitude, typically 300 nsec in width and with a rise time of 90 nsec, is shown schematically in Fig. 3.7. The system consists of a hydrogen filled ceramic thyratron (EG&G 1802), a thyratron driver (Plasma/Kinetics Model 121) operating at 5kHz, a charging network, two pulse transformers and the discharge electrodes. When the thyratron is in its non-conducting state (between driver pulses), the saturable inductor and the charging capacitor, C_1, form a resonant charging circuit. In a manner similar to an underdamped control system, the voltage across C_1 swings to a value 60% higher than the voltage of the pulser power supply. To prevent the current from reversing, a holdoff diode is placed in series with the resonant charging circuit. In this manner the voltage on C_1 is clamped until the thyratron is fired. When the thyratron

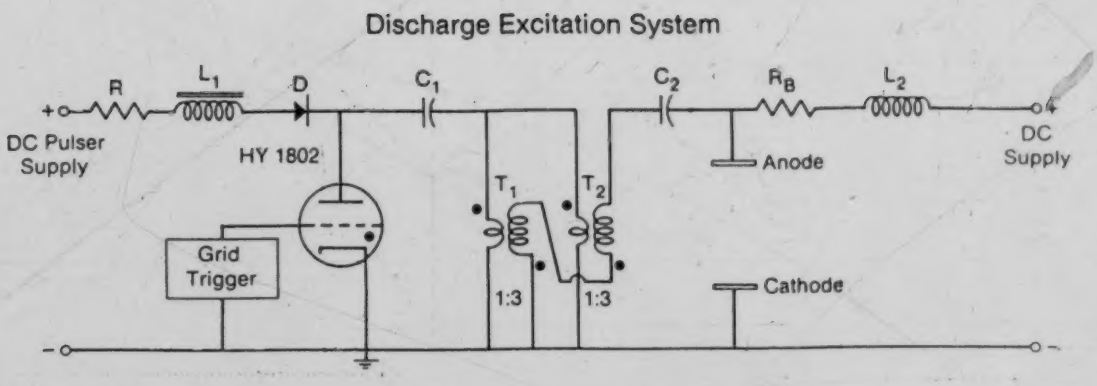

R, Current Limiting Resistor = 1 kΩ
L_1, Saturable Inductor = 1000→20 mH
D, Charging Diode = 20 kV P.I.V.
C_1, Storage Capacitor = 2 nF

T_1, T_2, Pulse Transformers = 1:3
C_2, Coupling Capacitor = 10 nF
R_B, Fluid Ballast Resistor = 600Ω
L_2, Blocking Inductor = 670 μH

Fig. 3.7 Discharge Excitation System

is fired, the high voltage side of the capacitor C_1 is shorted to ground. Because the voltage across a capacitor cannot change instantly, an inverted voltage appears across the primaries of the two 1:3 step-up pulse transformers. The two secondaries, which are in series, re-invert the voltage across C_1, as well as stepping up the output voltage by a factor of six. Thus, the voltage from the pulser power supply is stepped up by a factor of 1.6 by the resonant charging circuit. A further step-up of 6 is achieved with the pulse transformers developed by Merchant, Seguin and Dow.[66] These combined effects give a 9.6 to 1 step-up, with this greatly increased voltage being transferred to the anode through the coupling capacitor C_2.

During operation, it was noted that the step-up of 9.6 to 1 was only realizable when feeding a load of very high impedance (open circuit), and even then for an input voltage of less than 2kV. For a pulser supply voltage of 4kV, a step up of only 6.25 to 1 was obtained. Another reduction in output pulse voltage was noted when the pulser was connected to the system. The discharge impedance proved to be sufficiently low to load the pulse transformer secondaries to the degree that a 6kV input voltage was required to provide a 20 kV output pulse, when the system was filled with a 20 Torr (1:1:4:14) gas mixture.

Furthermore, the pulser efficiency proved to be a function of DC current. As the conductivity of the plasma increases with increased DC current, the output pulse voltage decreases. For a constant pulser input voltage of 4 kV, the output pulse voltage dropped from 15 kV at zero amps DC to only 10 kV at a current of 2 amps DC. The ionization power input to the plasma depends on the amplitude of the pulse output voltage squared. This aspect is illustrated in Fig. 3.8, which features pulser output voltage squared plotted against DC current. As will be seen in section 4.3, this pulser characteristic has interesting consequences for the evaluation of electron density.

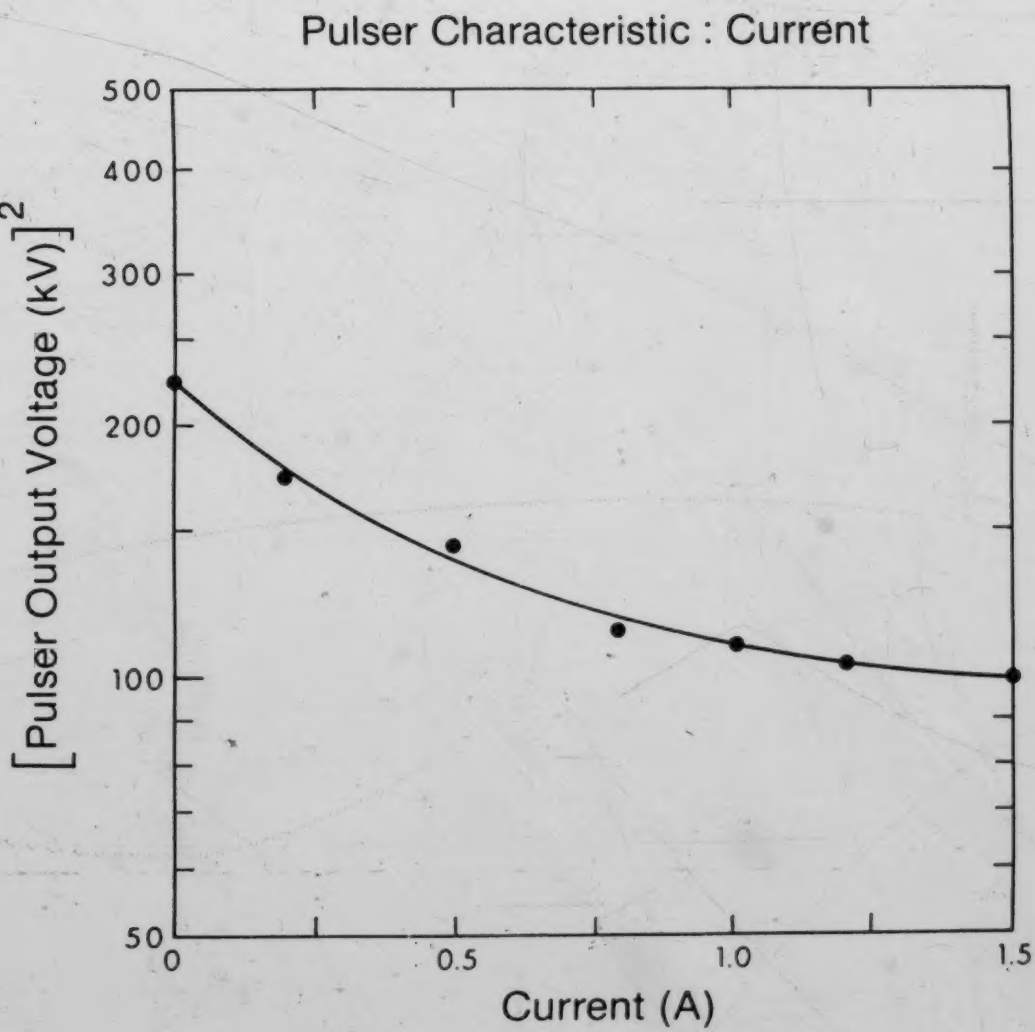

Fig. 3.8 Pulser Characteristic: Effect of DC Current

3.6 Sustainer Power Supply Connections

Connections for the sustainer power supply are shown in Fig. 3.7. The power source is a 40 kVA DC supply, adjustable in voltage up to 4000 V. The series resistor, R_B, is the fluid ballast resistor described in detail earlier. The blocking inductor, L_2, is required to prevent pulser output loading due to the highly capacitive coaxial feed line of the sustainer power supply. Severe pulser loading was noted in the absence of L_2, with the pulser losing over half its energy charging the coaxial line. This aspect resulted in unacceptable losses in the power available to pre-ionize the gas discharge volume.

In conclusion, the experimental design is now complete. A 50 cm long test section is mounted into a recirculating gas loop; with a flow velocity of up to 12 m/sec being available at a 20 Torr pressure. The transverse rotating magnetic field, up to 450 Gauss in strength, is supplied with three individual modules; all having the same direction and correct phase orientation. A reliable electrode structure has been developed and the means of providing external ionization is available. The experimental analysis of the magnetically stabilized gas discharge may therefore now proceed.

CHAPTER IV

EXPERIMENTAL RESULTS AND OPERATIONAL CHARACTERISTICS

Once the system design and construction were complete, a comprehensive series of tests were done to determine the operational characteristics of the magnetically stabilized gas discharge. In this chapter, investigations of the terminal characteristics, gas temperature and electron density will be discussed. Gain characteristics and laser output power, derived from the experimental gas discharge, will be presented in chapter VI.

4.1 Terminal Characteristics

Terminal (V-I) characteristics were the first tests performed on the magnetized plasma column. For all measurements (unless otherwise noted), a gas mixture of 1 Torr CO_2, 1 Torr CO, 4 Torr N_2, and 14 Torr He is used. All voltages, currents and power in the graphical data refer to calculated quantities exclusive of ballast resistance losses.

The effect of gas flow velocity on the V-I characteristics is shown in Figs. 4.1 - 4.4. The performance with zero magnetic field is shown in Fig. 4.1. Operating voltages are observed to be an increasing function of gas velocity. Initially, the V-I curves exhibit a positive slope relationship, indicative of behaviour in the abnormal glow regime.[48] With increased current, the operating voltage is seen to saturate, signalling the impending onset of a glow-to-arc transition. Upon the application of a 450 Gauss transverse rotating magnetic field, the V-I characteristics change to those shown in Fig. 4.2. In this figure, operating voltages for a given gas velocity are seen to be significantly higher than those found when the magnetic field is absent. The V-I curves maintain a positive slope for the range of currents observed. Thus, the discharge remains in the abnormal glow regime to a much higher power loading level when the magnetic field is used. For all flow velocities, the difference in voltage between the magnetized and non-magnetized plasma is observed to be an increasing function of DC current. This effect is shown clearly in Fig. 4.3, which derives its data from Figs. 4.1

and 4.2.

The effect of the transverse rotating magnetic field on the V-I characteristic for a 10 m/sec flow velocity, is shown is Fig. 4.4, for a series of magnetic field strengths. In all cases, an instability is seen to be initiated at the anode, under a DC sustainer current drive of ~2 amps. At the onset of the instability, light flashes were observed to be emitted from the anode. Increasing the sustainer voltage still further resulted in the development of an arc. It is believed that this is primarily an electrode effect; with the bulk gas playing a negligible role in initiating the instability.

Figs. 4.5 and 4.6 are derived from the V-I characteristics. The maximum input power achieved as function of gas velocity is shown in Fig. 4.5, which takes its data from Figs. 4.1 and 4.2. The 450 Gauss magnetic field is seen to allow an increased power loading for all gas flow velocities. As the flow velocity increases, the increase in maximum input power for the magnetized plasma grows at a faster rate; such that at a flow velocity of 10 m/sec, the use of a 450 Gauss transverse rotating magnetic field allows an additional 0.9 kW to be deposited into the plasma. Input power vs. magnetic field for a series of DC currents is shown in Fig. 4.6. This data is derived from Fig. 4.4. At currents of less than 1 amp, the magnetic field is seen to have no appreciable effect. Consequently, the additional power deposited into the plasma was negligible. The beneficial effect of the transverse rotating magnetic field becomes apparent at currents above 1.2 amps. At a current of 2 amps, the rotating magnetic field allows the power loading of the plasma to be increased by a factor of 25%.

Previous experiments were performed with a fixed pulser input voltage of 6kV. Thus, to study the effects of external ionization on the gas discharge, a series of V-I characteristics were taken at 1 kV pulser voltage increments, between 2 and 6 kV. The terminal characteristics so generated, at zero and 450 Gauss magnetic field, are shown in Figs. 4.7 and 4.8 respectively. In Fig. 4.7, a decrease in the pulser input voltage results in an increased terminal voltage. This effect may be explained as follows. The pulser clearly provides preionization for the plasma volume. Consequently, as the amount of external ionization decreases, the sustainer supply voltage must increase to compensate for the reduced

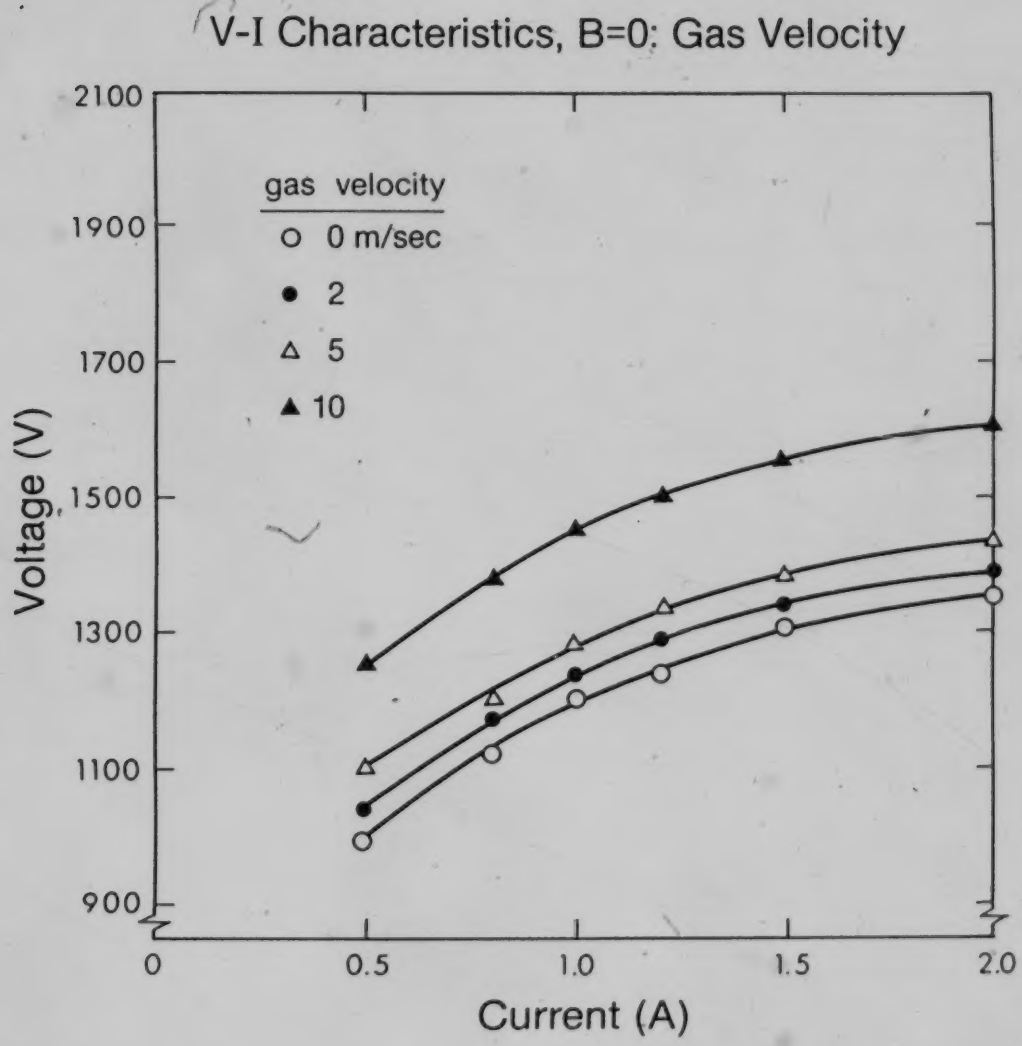

Fig. 4.1 V-I Characteristics, B = 0: Effect of Gas Velocity

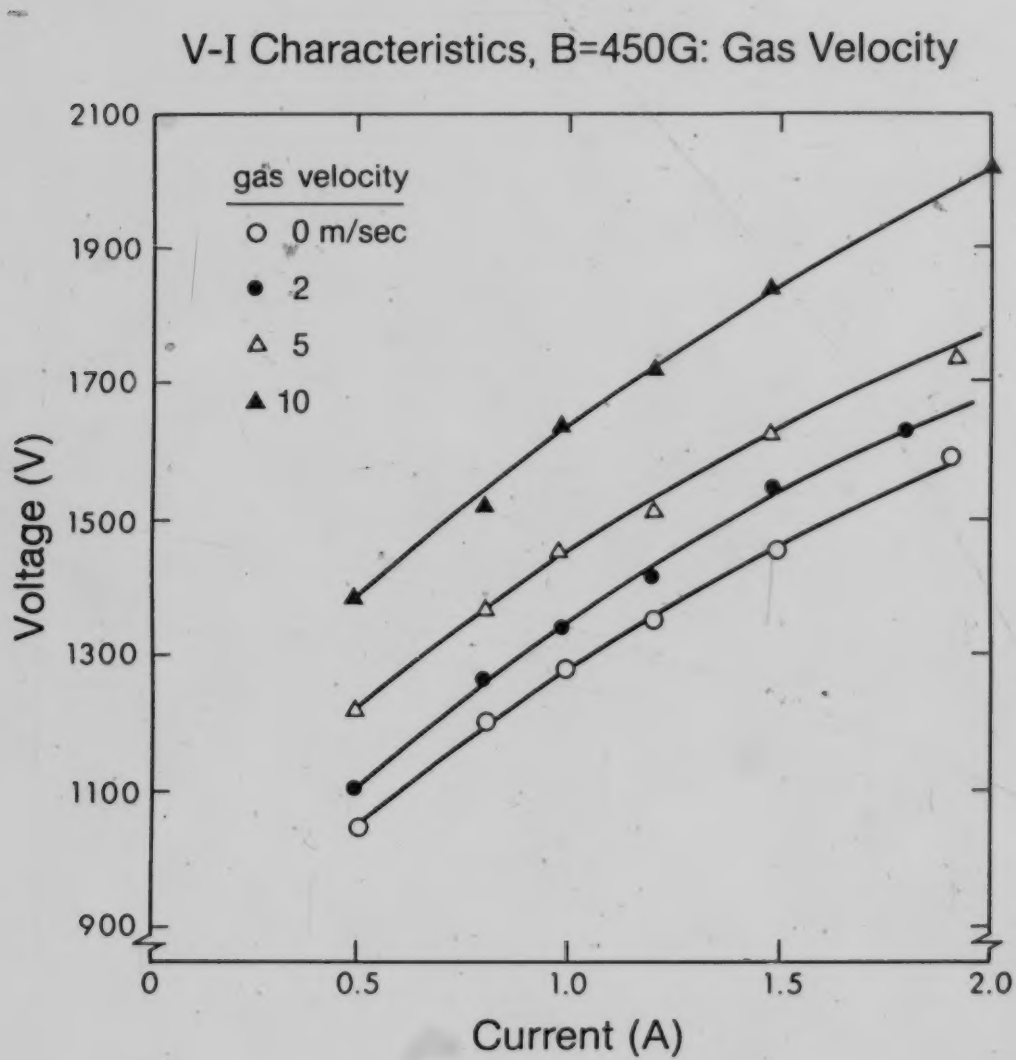

Fig. 4.2 V-I Characteristics, B = 450 Gauss: Effect of Gas Velocity

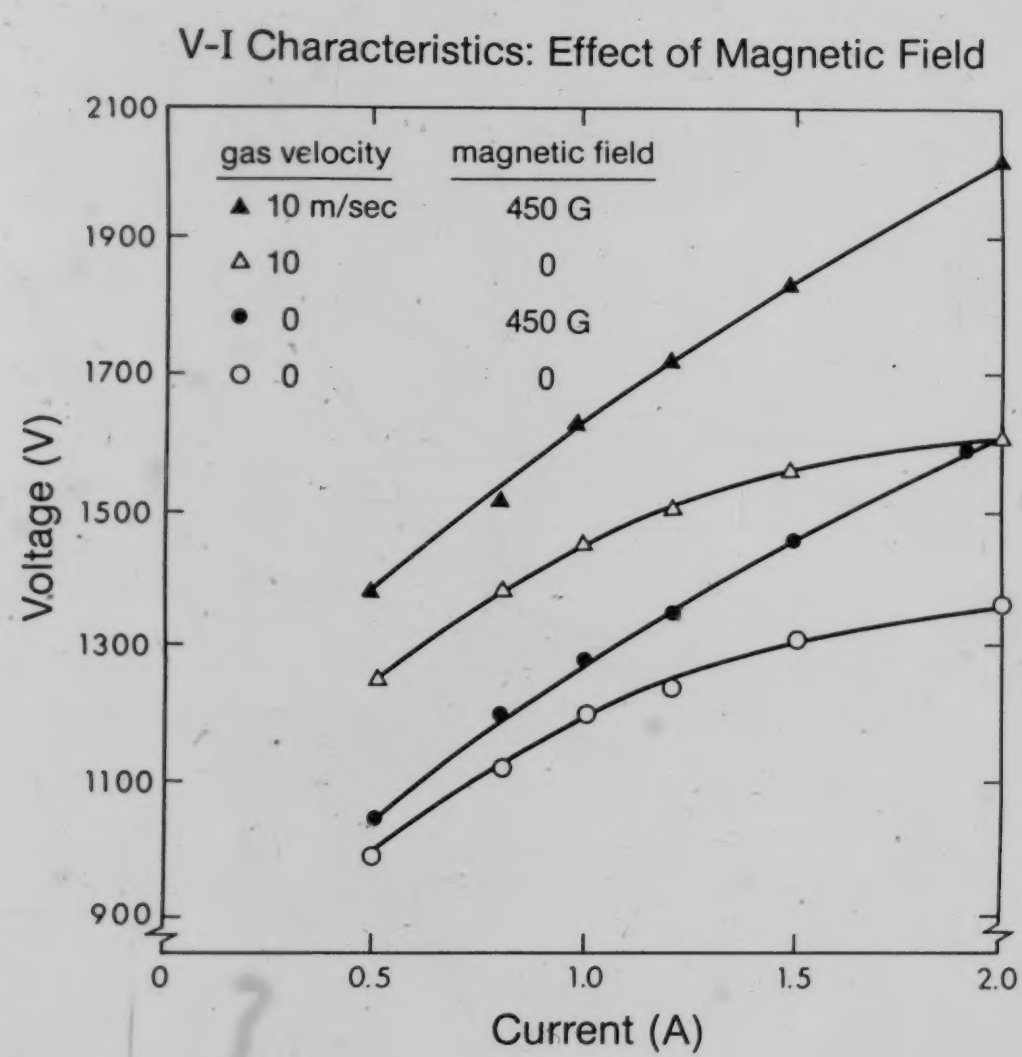

Fig. 4.3 V-I Characteristics: Effect of Magnetic Field

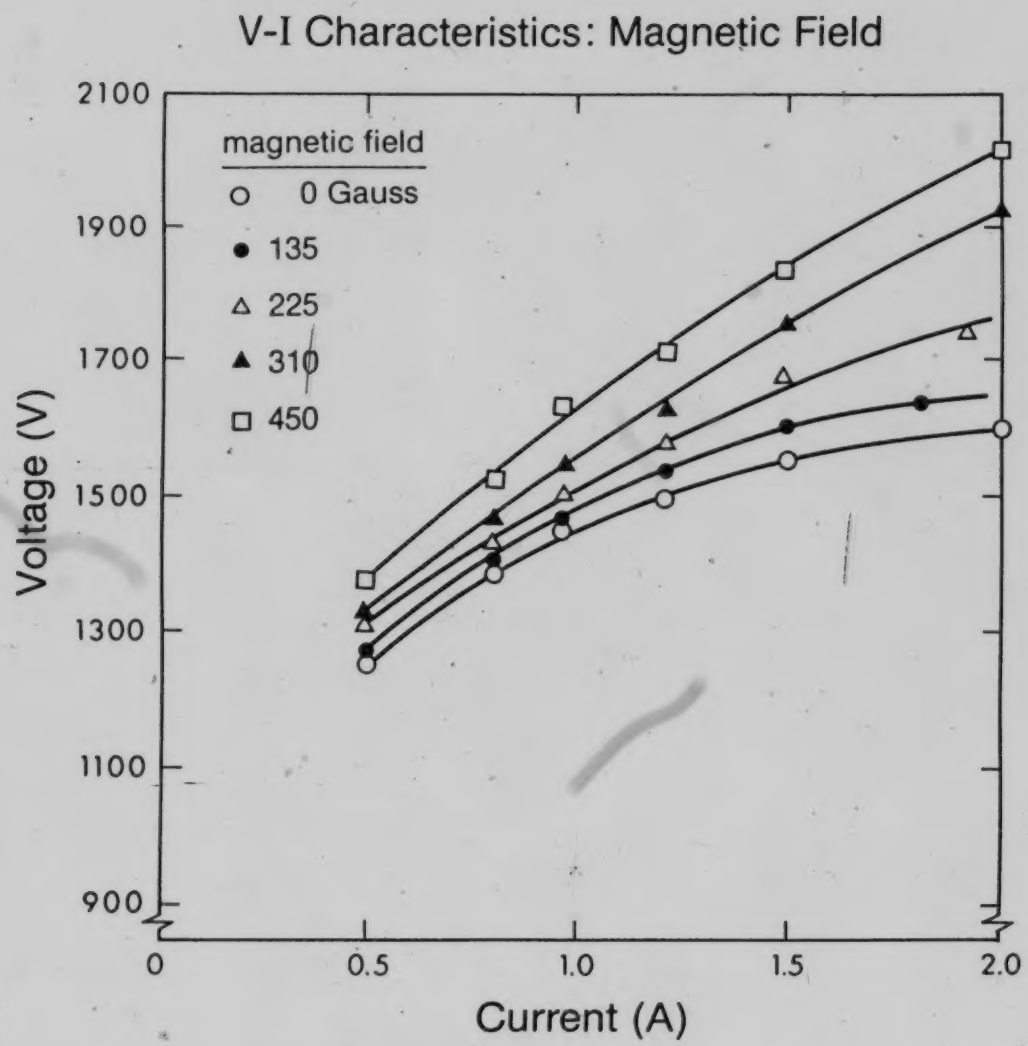

Fig. 4.4 V-I Characteristics: Variation of Magnetic Field

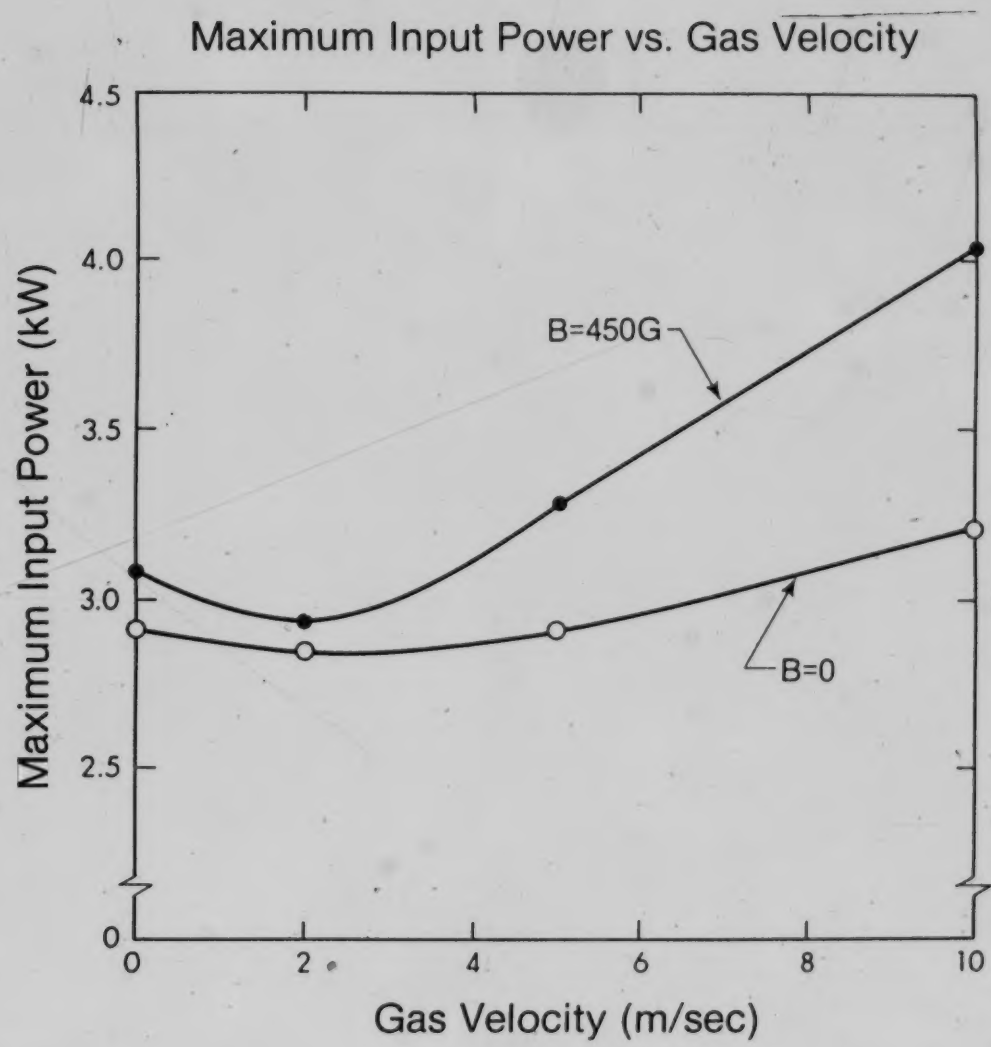

Fig. 4.5 Maximum Input Power vs. Gas Velocity

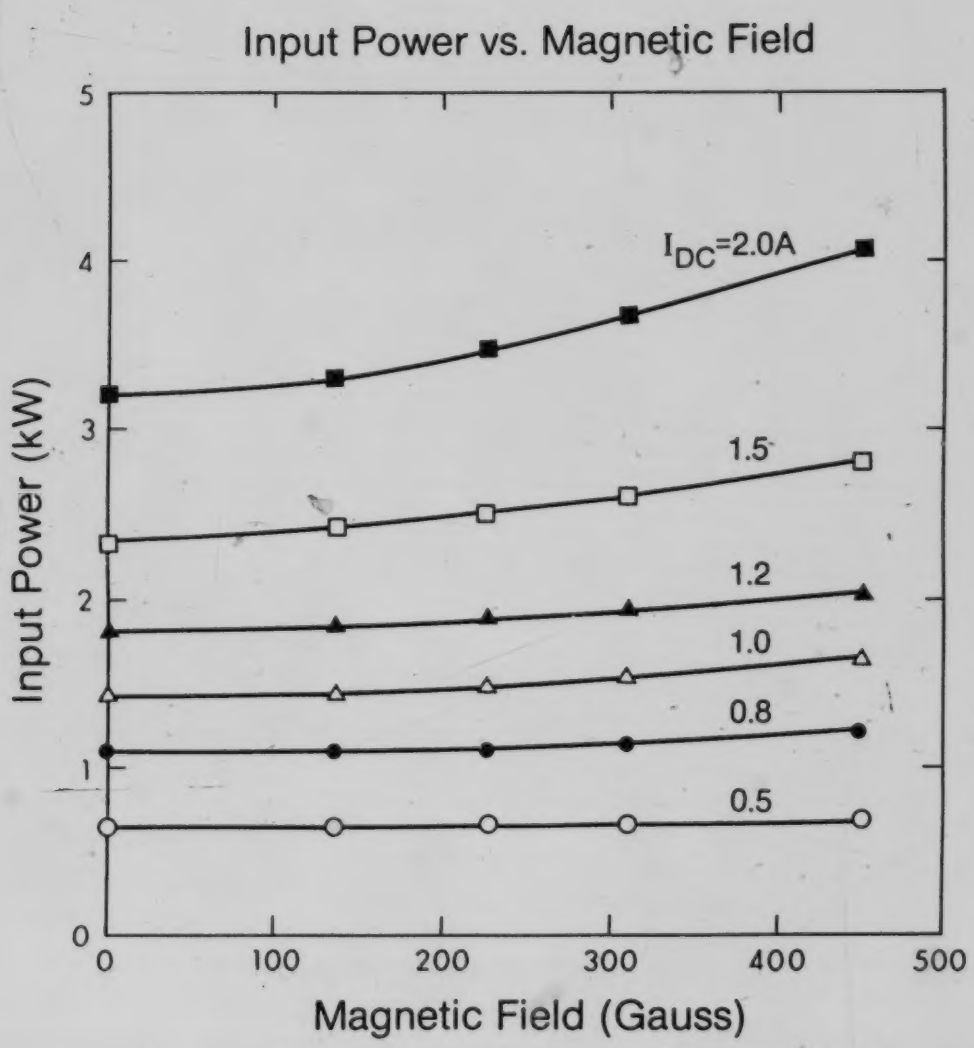

Fig. 4.6 Input Power vs. Magnetic Field

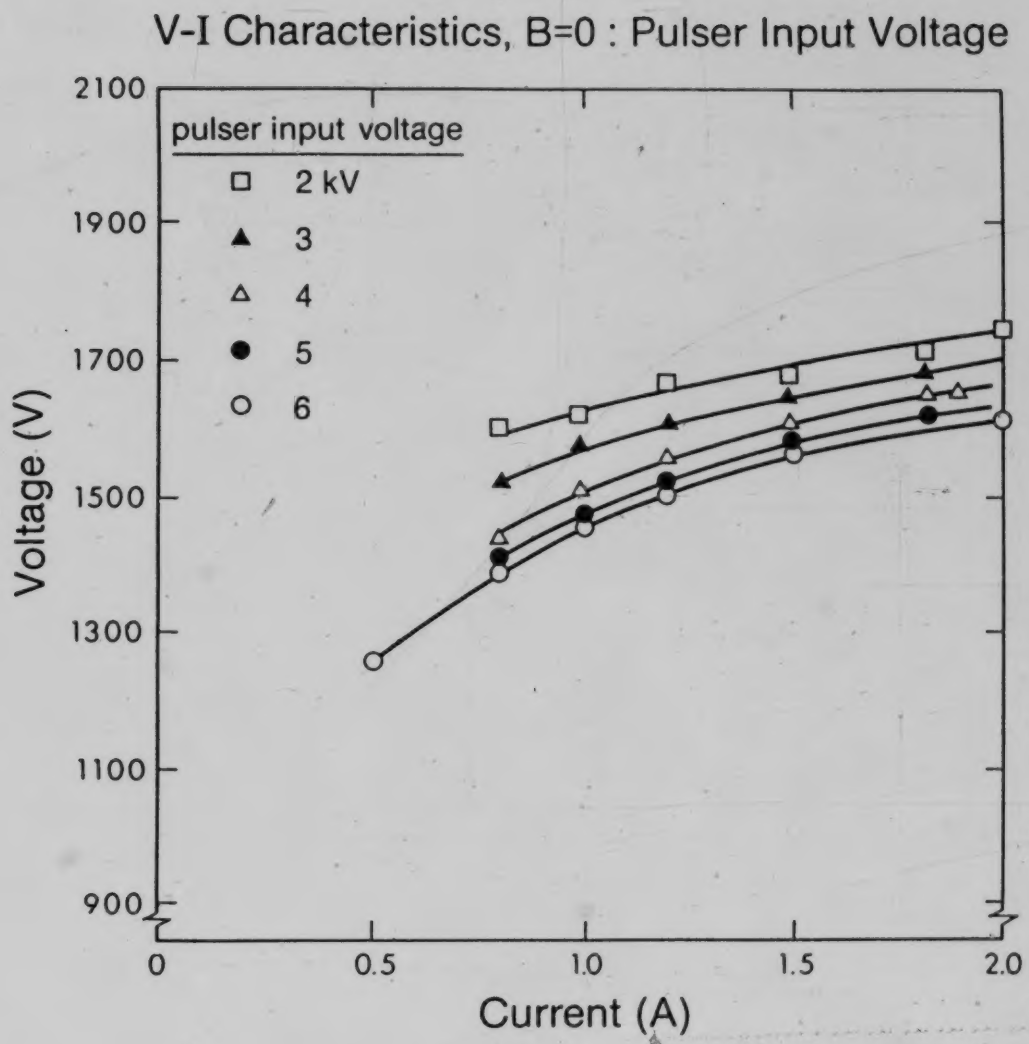

Fig. 4.7 V-I Characteristics, B = 0: Effect of Pulser Input Voltage

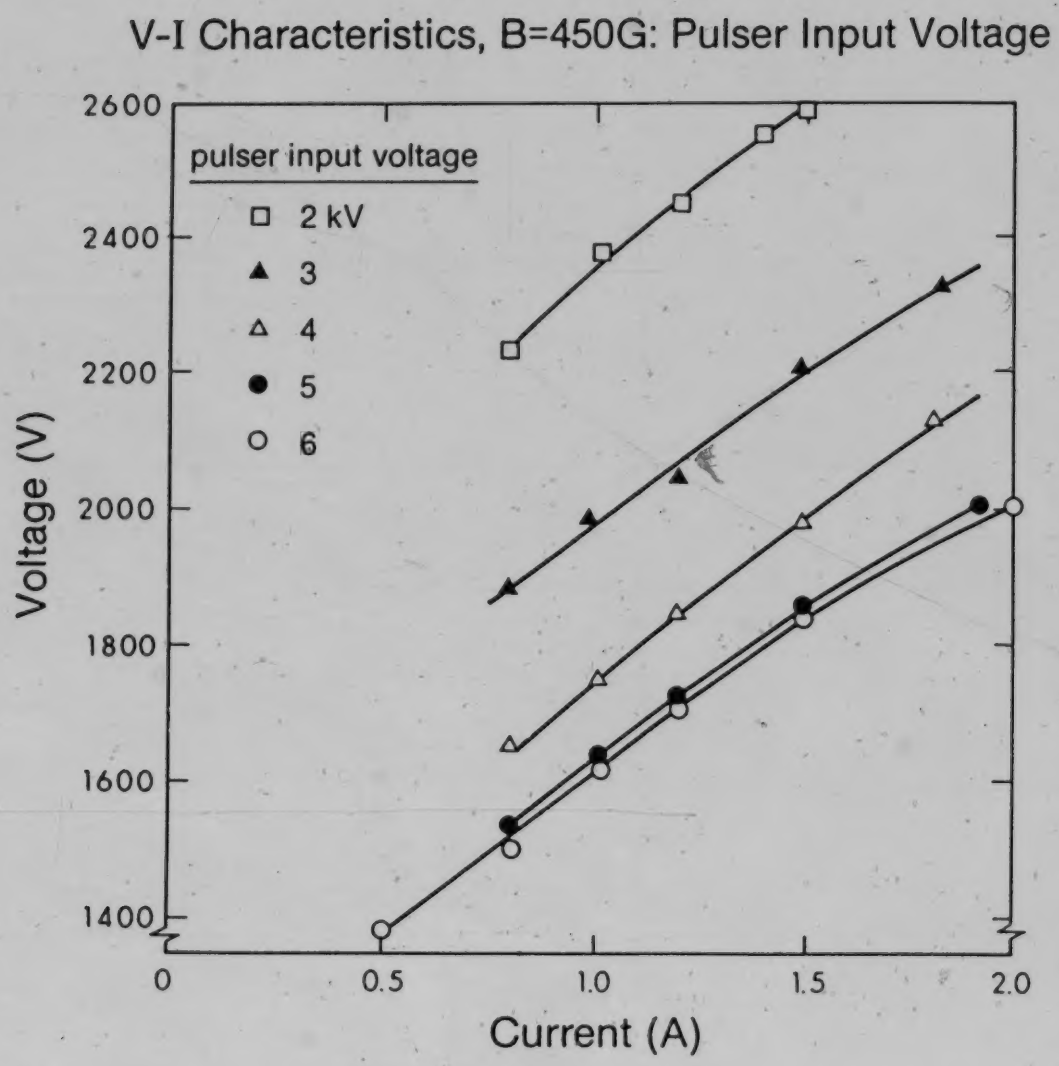

Fig. 4.8 V-I Characteristics, B = 450 Gauss: Effect of Pulser Input Voltage

conductivity of the plasma volume at a given current.

With the application of the transverse rotating magnetic field, the voltage required to sustain the plasma is observed to increase dramatically, particularly for low pulser input voltages. This effect, illustrated in Fig. 4.8, is the result of a further reduction in axial plasma conductivity, resulting from the magnetically induced rotation of the plasma column. This magnetic field effect was discussed in chapter 2.

The variation of discharge power input with pulser power, as derived from the results in Figs. 4.7 and 4.8, are shown in Figs. 4.9 – 4.11. With zero field, the power deposited into the discharge changed only slightly with pulser input, regardless of DC current. However, with a magnetic field of 450 Gauss, the sustainer power deposited into the plasma was substantially higher; especially for low values of pulser ionization and high DC currents. This aspect provides the operator with a convenient means for optimizing the E/N ratio; thereby facilitating maximum power deposition into the upper CO_2 laser level.[24] These results suggested that a low pulser power input, in combination with a transverse rotating magnetic field, could indeed provide an effective means for CO_2 laser excitation.

In order to completely investigate the device terminal characteristics, additional V-I curves were taken for three other gas mixtures. All three experiments were performed at the same total pressure of 20 Torr, and the gas flow velocity for all three tests was held constant at 10 m/sec. Each test was done with and without the applied rotating magnetic field. The data in Figs. 4.12 – 4.14 demonstrates that essentially the same effects are observed with other gas mixtures.

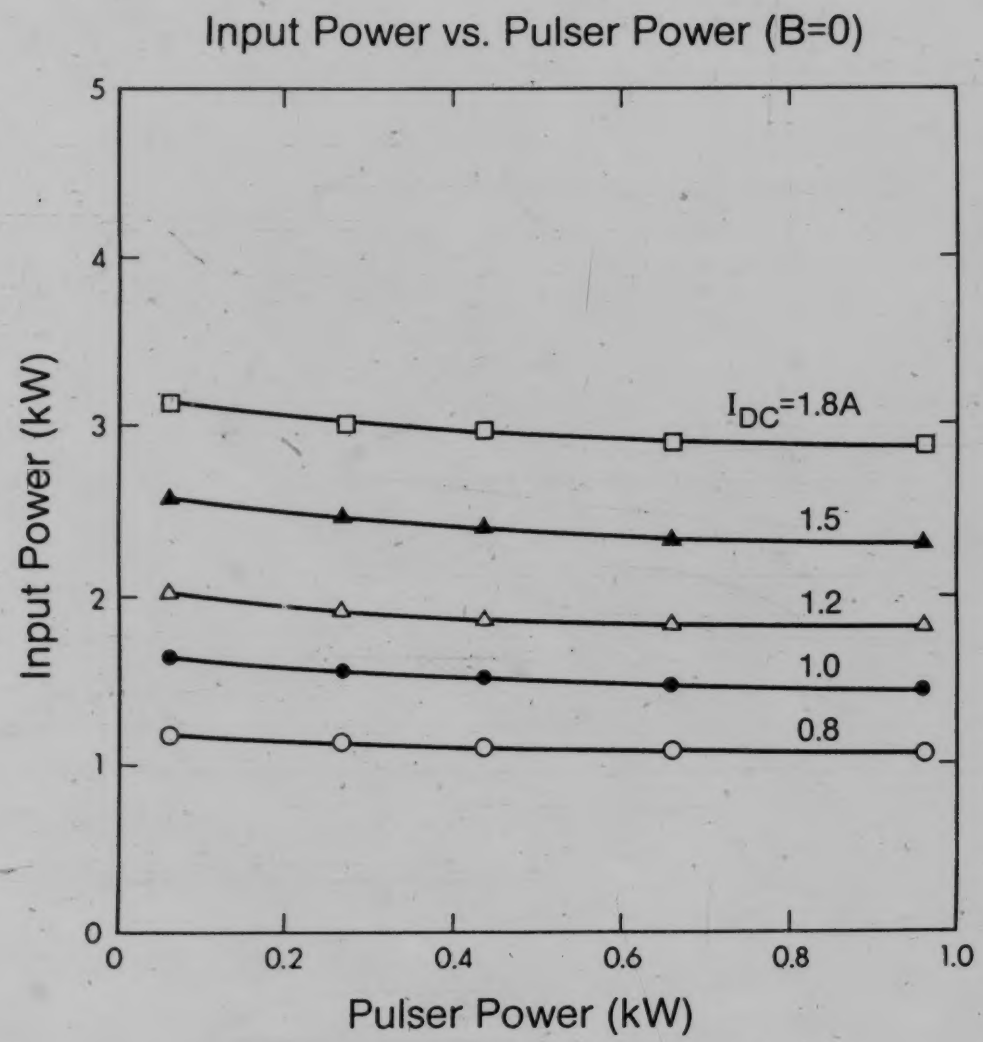

Fig. 4.9 Input Power vs. Pulser Power, B = 0

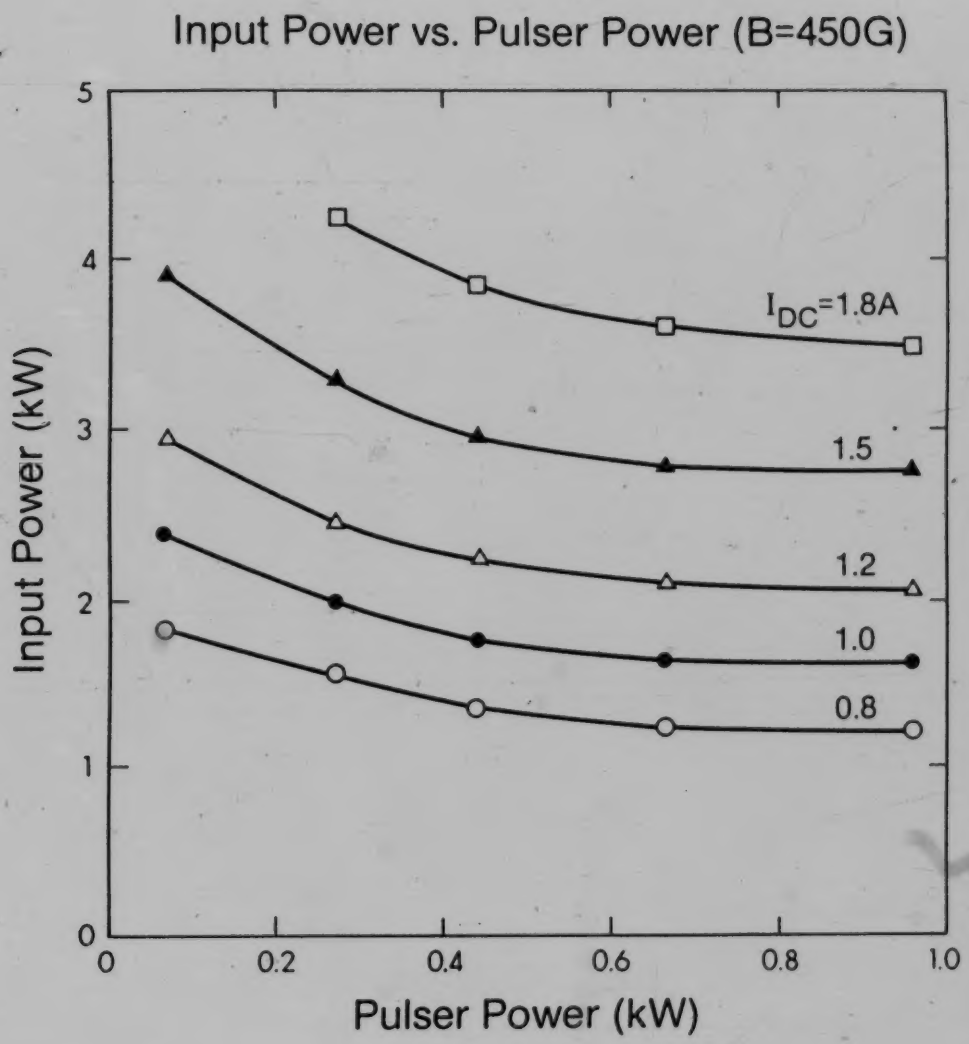

Fig. 4.10 Input Power vs. Pulser Power, B = 450 Gauss

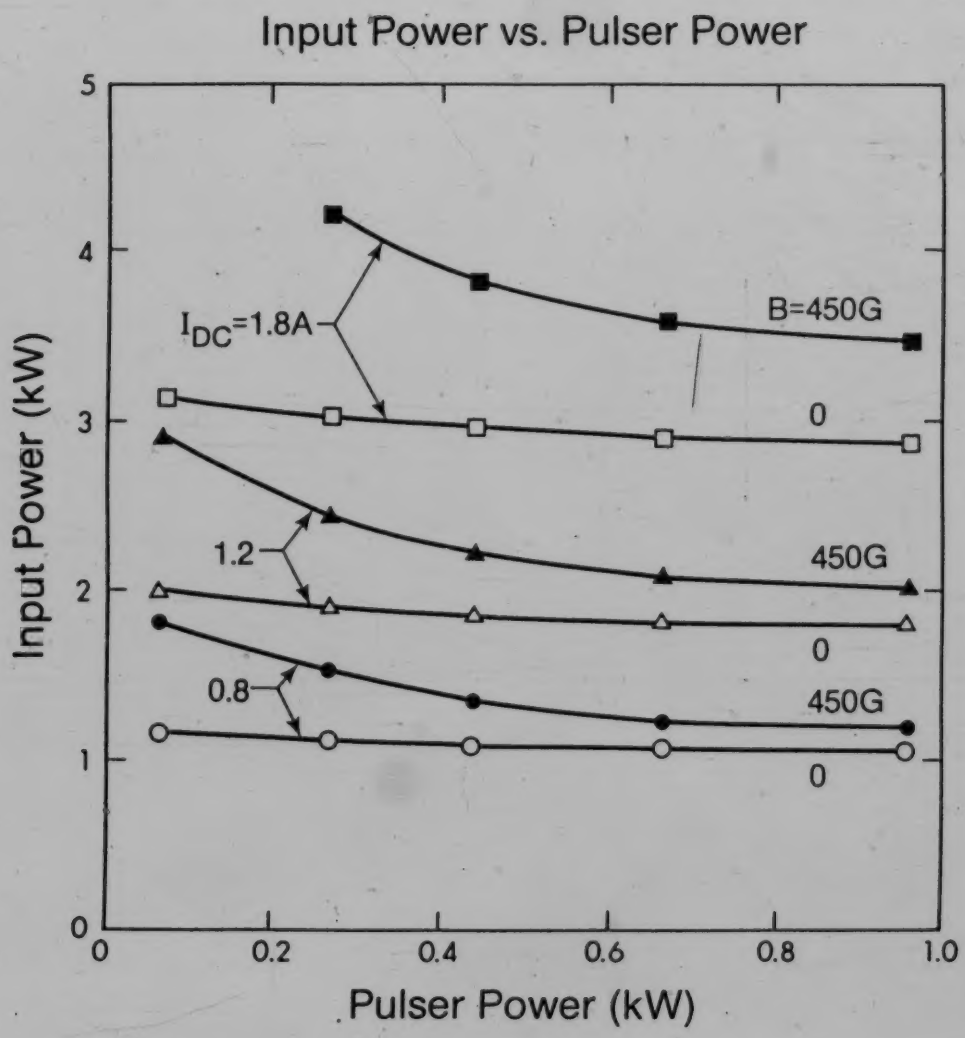

Fig. 4.11 Input Power vs. Pulser Power: Effect of Magnetic Field

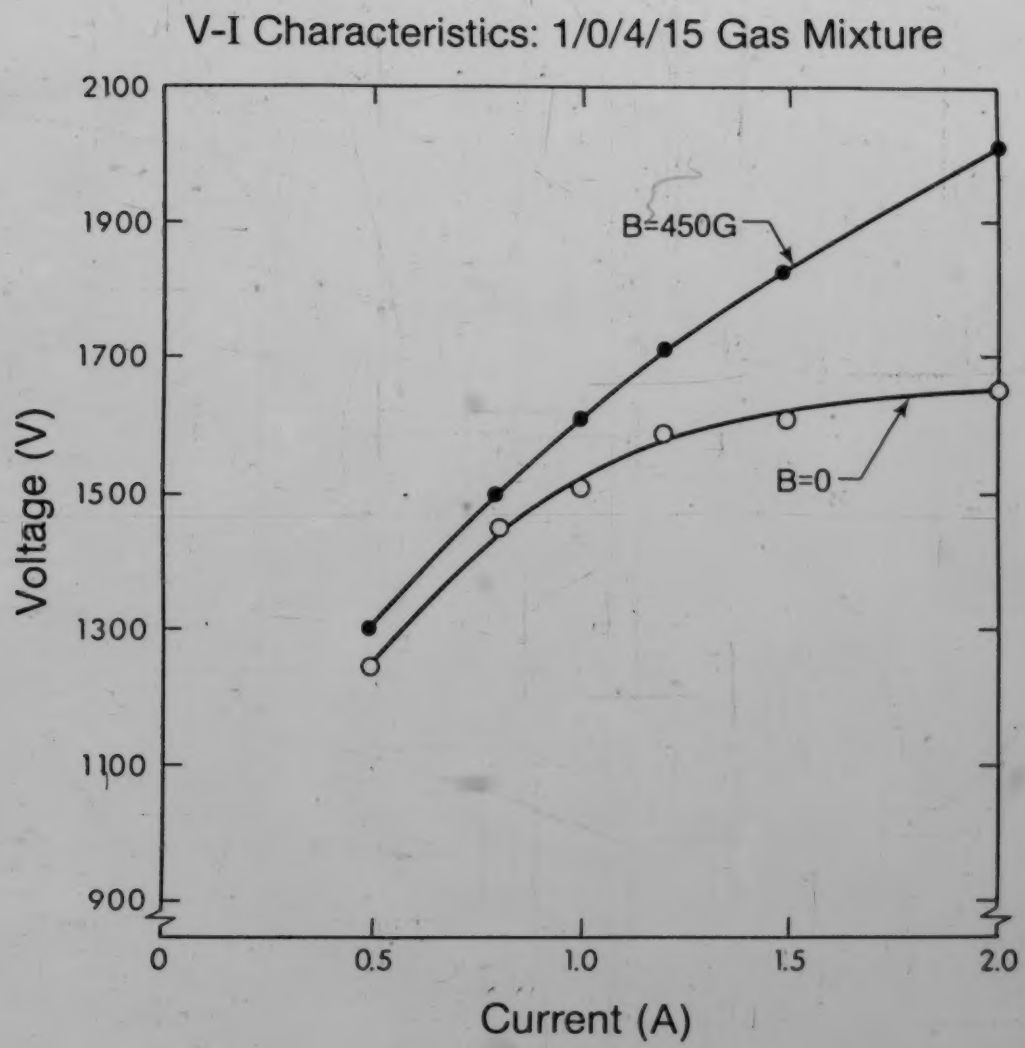

Fig. 4.12 V-I Characteristics: 1/0/4/15 Gas Mixture

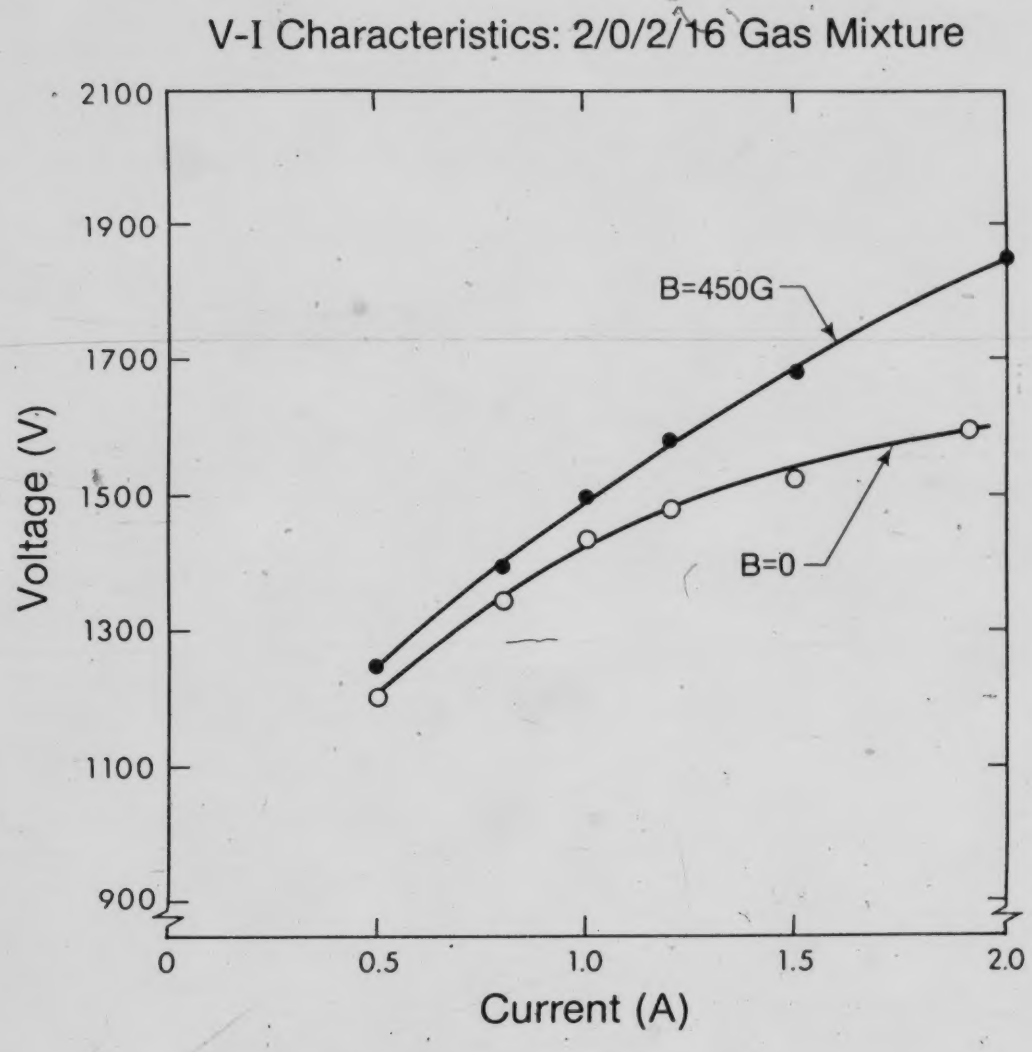

Fig. 4.13 V-I Characteristics: 2/0/2/16 Gas Mixture

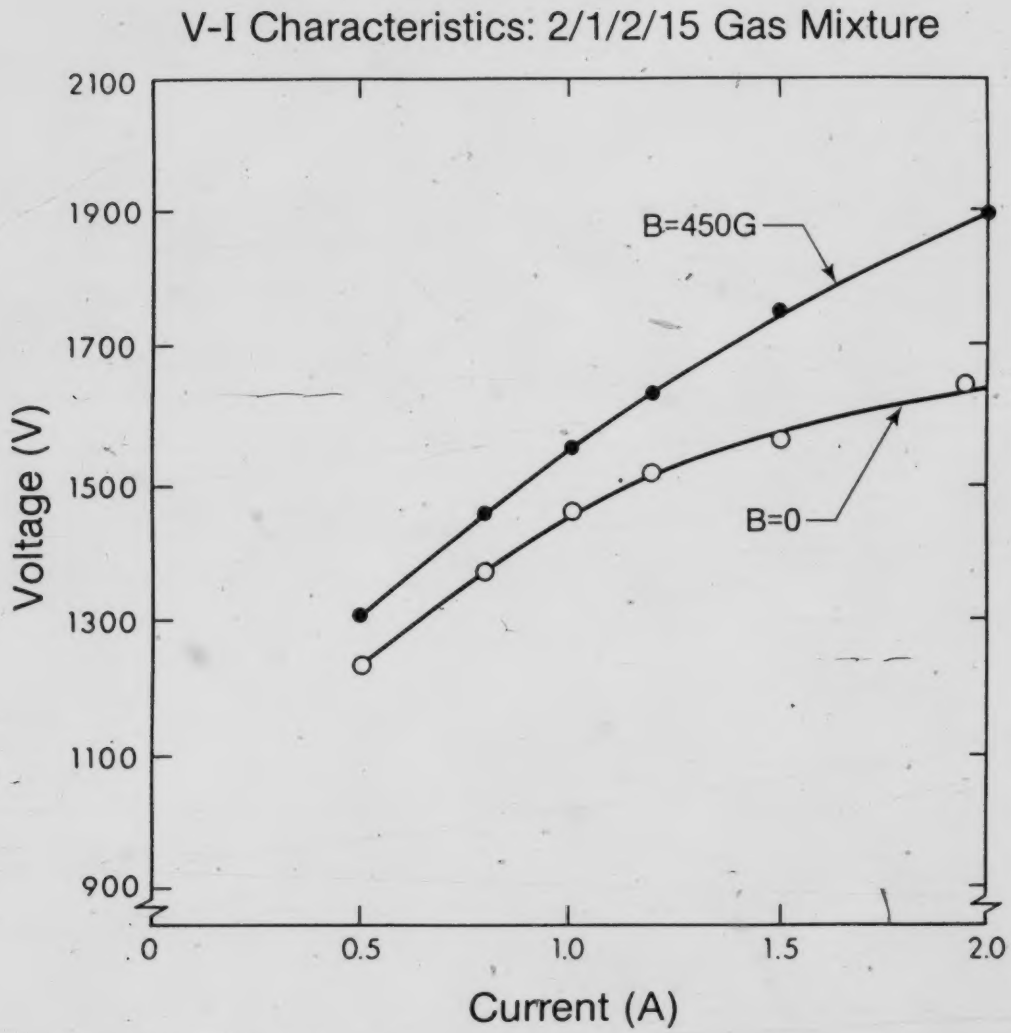

Fig. 4.14 V-I Characteristics: 2/1/2/15 Gas Mixture

4.2 Gas Discharge Temperature Measurements

The second set of measurements made were those of gas temperature. Such data is important, since previous experimentation has shown that the temperature of the gas media must be kept sufficiently low so as to prevent "thermal bottlenecking" of the lasing process.[16] Thermal bottlenecking occurs whenever the $CO_2(01^10)$ vibrational level becomes populated as a result of thermal excitation from the ground state. A discussion of this topic was presented in section 1.2.

Temperature measurements were made 5 cm downstream from the cathode end of the discharge apparatus. Measurements were performed with a type J thermocouple (iron-constantan) having a wire diameter of 0.010 inches (AWG 30). The response time constant for this thermocouple is 0.28 sec; thus providing a sufficiently fast response for accurate temperature analysis. The thermocouple has a useful working range of 0 to 750°C.

The temperature profiles obtained with zero magnetic field are shown in Fig. 4.15. During this test, it was observed that the gas discharge was off-center. This was the result of the discharge column being blown downstream from the side-mounted anode. With the application of a 450 Gauss magnetic field, the rotating plasma column sweeps through a larger cross-section, whose area increases with DC input power. This effect is a manifestation of the stronger Lorentz force, that increases with applied voltage and current. The temperature profiles of Fig. 4.16 are still slightly skewed at low power inputs. However, as power input increases, the temperature profiles adopt the more usual Bessel type distribution.[15] At high power loadings the rotating plasma column is found to sweep though the entire cross-section of the discharge chamber.

In order to complete the investigation, data showing the variation of gas outlet temperature with input power is required. However, since measurements indicated that the temperature distributions are non-axisymmetric for the zero-magnetic field case, the temperature profiles in Figs. 4.15 and 4.16 were integrated across the tube diameter to yield average values. The result, (Fig. 4.17), illustrates the variation of gas outlet temperature with input power, and reveals that the gas output temperature saturates with increased power

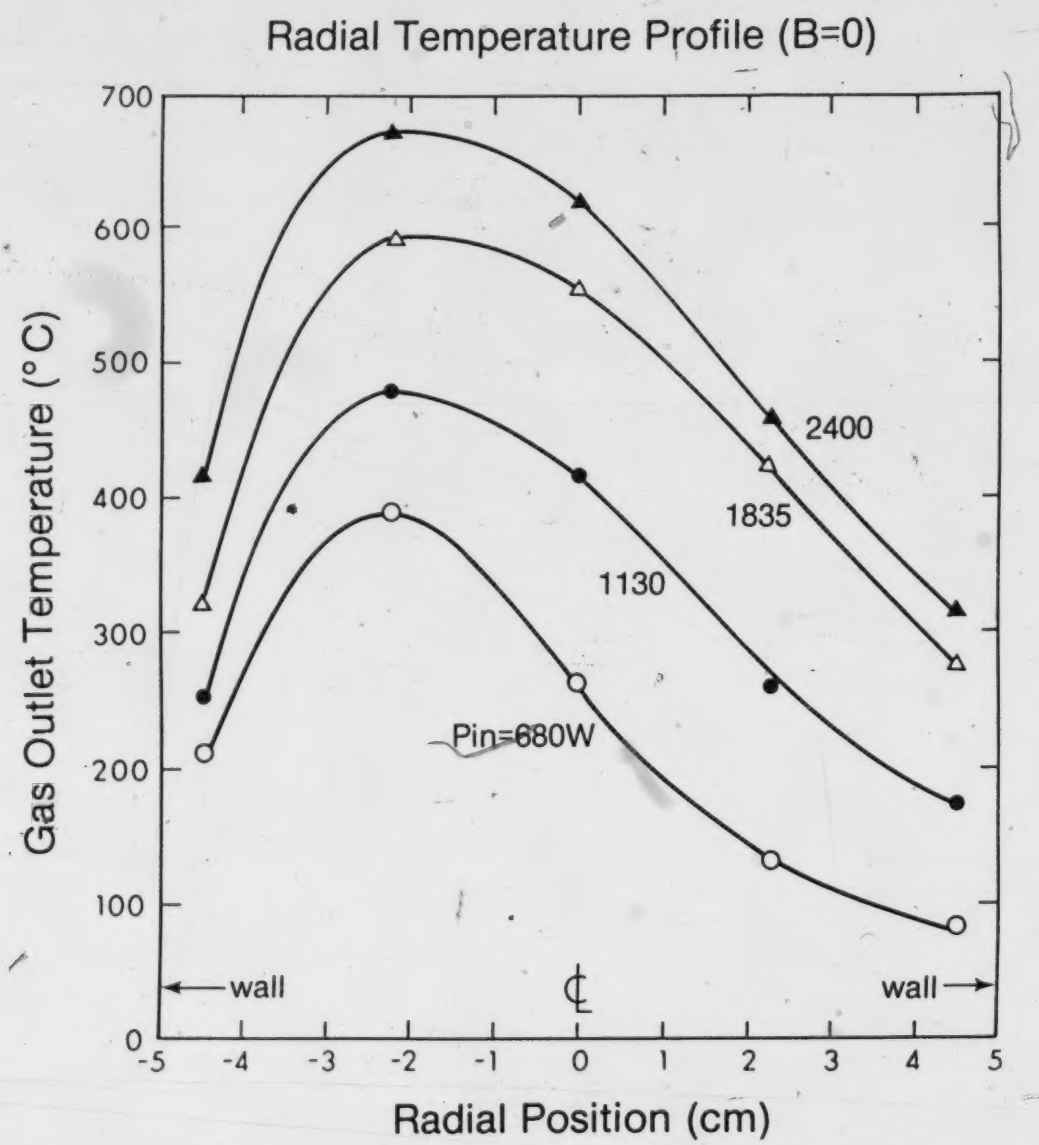

Fig. 4.15 Radial Temperature Profiles, B = 0: Variation of Input Power

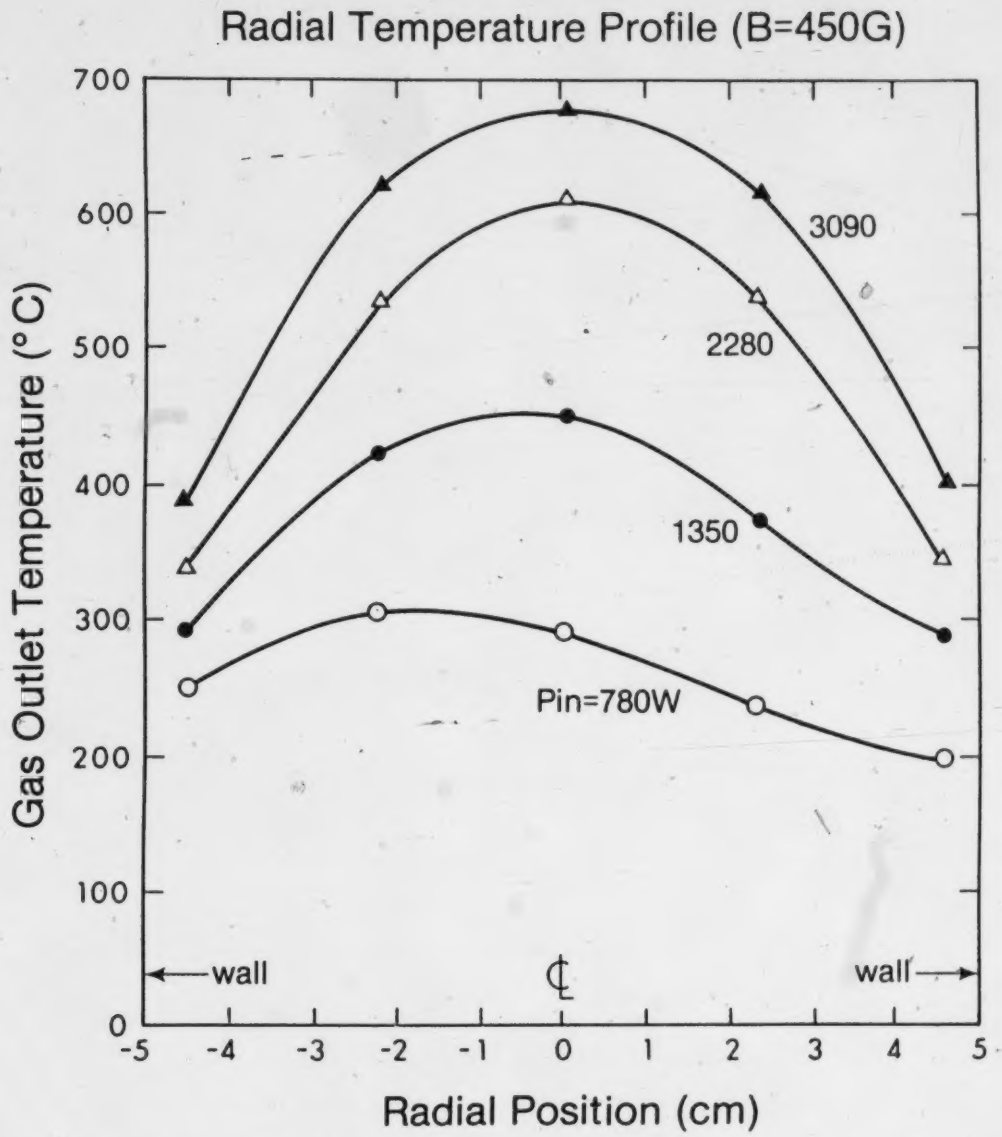

Fig. 4.16 Radial Temperature Profiles, B = 450 Gauss: Variation of Input Power

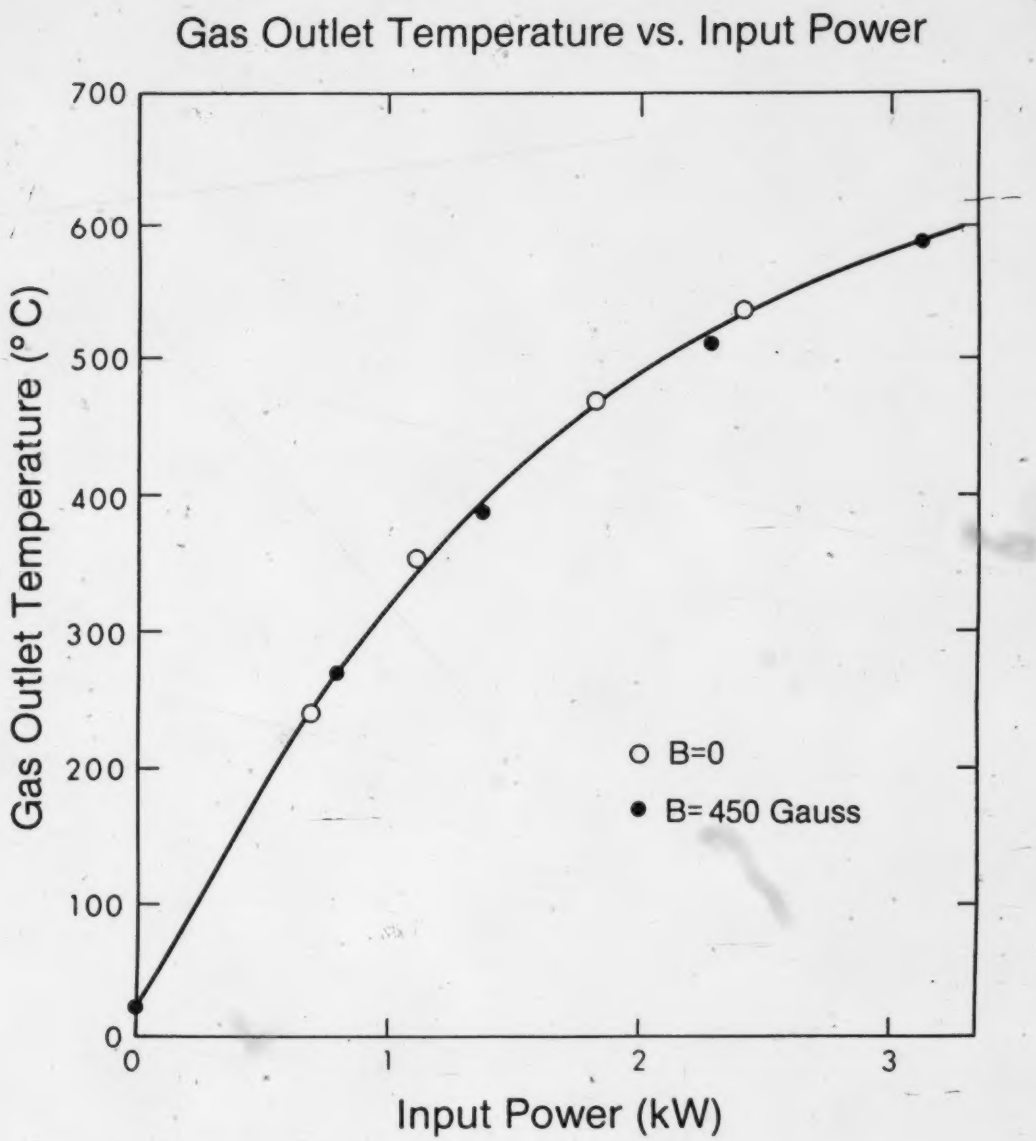

Fig. 4.17 Gas Outlet Temperature vs. Input Power

input. This unexpected feature may be explained by postulating that the cooling efficiency associated with the water cooling jacket improves with an increased gas temperature at the discharge chamber wall. Some justification for this contention is afforded by an examination of the power actually absorbed by the cooled water jacket. Such an absorption is given by:[67]

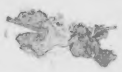

$$P_{wall} = \frac{2\pi k_{glass} L(T_{wall} - T_{H_2O})}{ln(1 + t_{wall}/R)}, \qquad (4.1)$$

where k_{glass}, L, T_{wall}, T_{H_2O}, R and t_{wall} are the thermal conductivity of the glass tubing, the length of the tube, temperature of the discharge tube inner wall, temperature of the cooling water, radius of the tube and wall thickness respectively. Eq. 4.1 shows that as the gas temperature at the discharge tube inner wall increases, (resulting from an increased power input), the difference between T_{wall} and T_{H_2O} also increases. This effect in turn provides a higher heat transfer efficiency. Hence, more heat is removed by wall conduction. This results in a reduced temperature rise of the gas, as it is convected past the thermocouple.

The effect of gas velocity on gas temperature is shown in Fig. 4.18. The input power and the magnetic field strength were kept constant at 2 kW and 450 Gauss respectively. Recordings were taken at the discharge tube axis, as well as at a radius of 4.5 cm. The output temperature, with no gas flow, is low because the thermocouple is physically situated at some distance from the discharge. As the gas velocity increases, hot gas is convected past the thermocouple, and the temperature rises. This effect continues until a gas flow velocity of 8 m/sec is reached. At this point, the thermocouple is being heated by the additional heat transported downstream by the low-speed gas flow. As the gas flow increases still further, past 8 m/sec, convective cooling becomes more effective. Thus, the gas outlet temperature is observed to drop. The shorter gas residence time that is achieved, results in less gas heating. Wall cooling accounts for the lower gas temperature recorded at the 4.5 cm radius.

This series of measurements demonstrated that the gas temperature was far too high to sustain laser action. Thus, a short test was performed to determine how fast the gas outlet temperature rises. Magnetic field strength and DC power input were kept constant at 450 Gauss and 2.5 kW respectively. The temperature rise observed as a function of time is shown

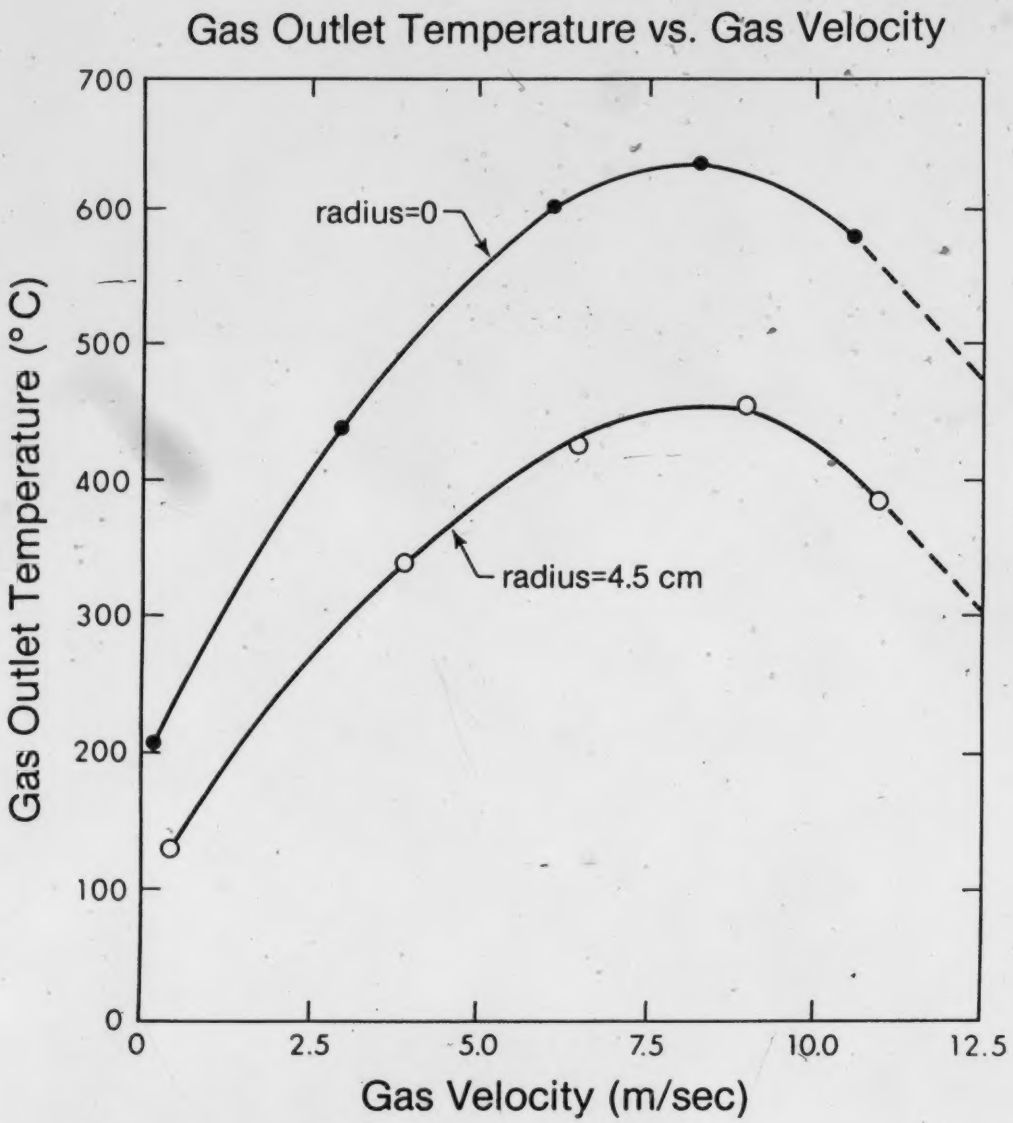

Fig. 4.18 Gas Outlet Temperature vs. Gas Velocity

in Fig. 4.19. The time constant for this exponentially increasing curve is 6.8 seconds. It is important to note that this value is far greater than the response time constant of the thermocouple.

It is clear from the temperature experiments that the plasma is only useful for laser action for 2 to 3 seconds at most. For this reason, it was necessary to do gain measurements of the magnetically stabilized discharge under short pulse conditions, leaving time for gas cooling between pulses. This burst discharge technique is discussed in section 5.3.

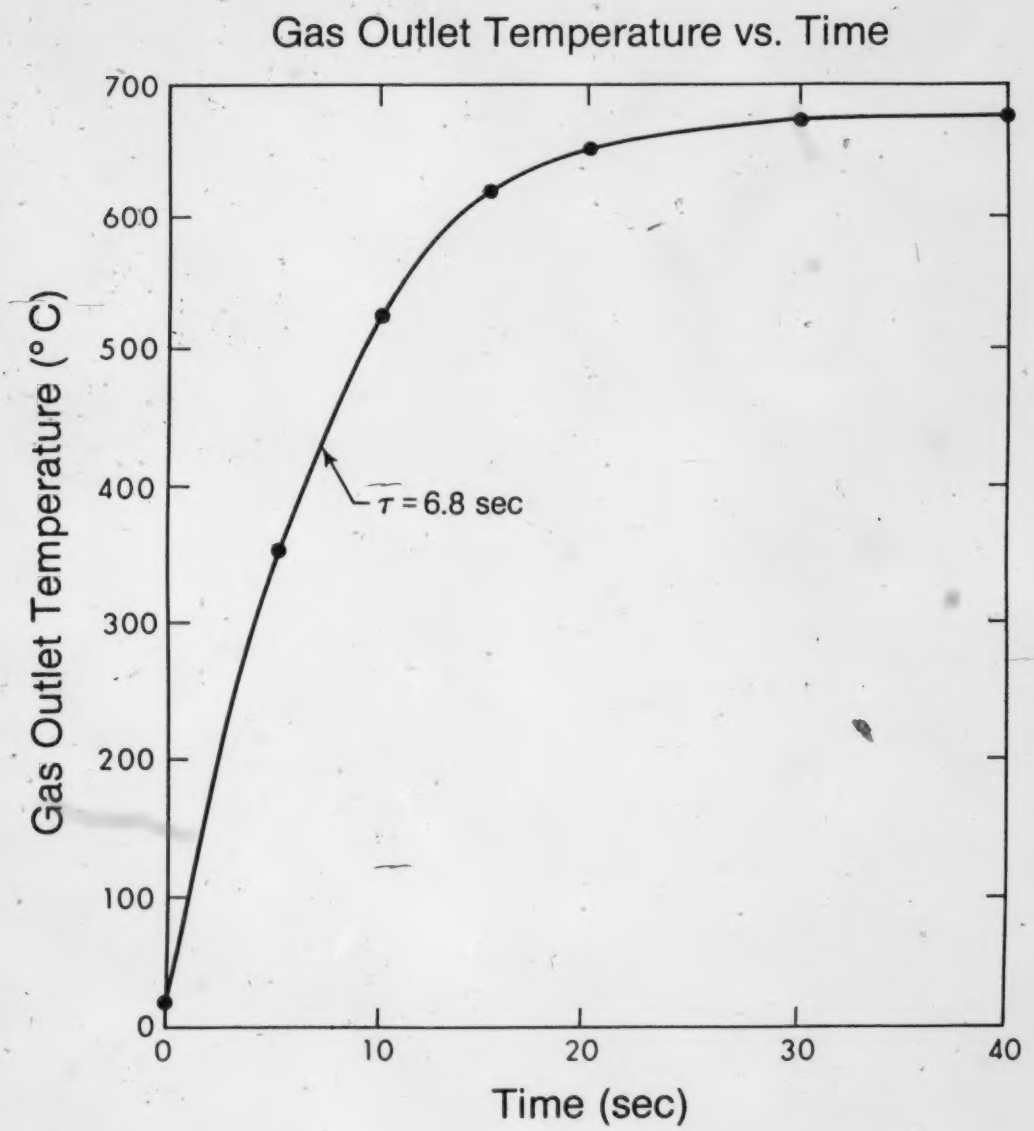

Fig. 4.19 Gas Outlet Temperature vs. Time

4.3 Electron Density Measurements

The next set of measurements undertaken were those of electron density within the discharge volume. Such measurements were first performed by Langmuir and Mott-Smith in the mid 1920's.[68] This data was desired, since extensive research has documented that electron density has a direct bearing on the gain attainable in the gas discharge.[3] In addition, the spatial behaviour of the plasma will affect the optical quality and concomitant power level achievable from the gain volume. This being the case, the electron spatial distribution and the manner in which the externally applied pulser affects the plasma electron density are of great significance to this work.

Measurements were performed using the conventional Langmuir probe apparatus shown in Fig. 4.20. A single conductor probe was inserted into the plasma at a point midway between the electrodes. The probe axis, being off-center, allowed the electron spatial distribution to be studied by simply rotating the probe body, thereby providing a radial scan through the tube axis. A blocking inductor, L, is needed to filter out the high voltage impulses induced into the probe tip by the pulser.

The probe is biased, with respect to the plasma, by using a power supply and voltage divider technique. A voltage divider is necessary to ensure that the power supply voltage is higher than the plasma potential at all times, since current cannot flow into the power supply. The resistor, R_0, is used to provide a low voltage signal (less than 50 V), to a differential oscilloscope. These low voltage signals were used for the low pressure (5 Torr) evaluation of electron density. This will be discussed in section 4.3.7.

The parameters of interest are the probe-to-plasma potential and the probe current. Both are related to the experimental measurements of power supply voltage and current. The power supply used is the Fluke #412B precision variable (0 - 2100V) DC supply. Power supply current was measured with a Hewlett-Packard #428B clip-on DC ammeter. The probe voltage and current, where probe current is defined as that flowing from the probe into the voltage divider, are given by:

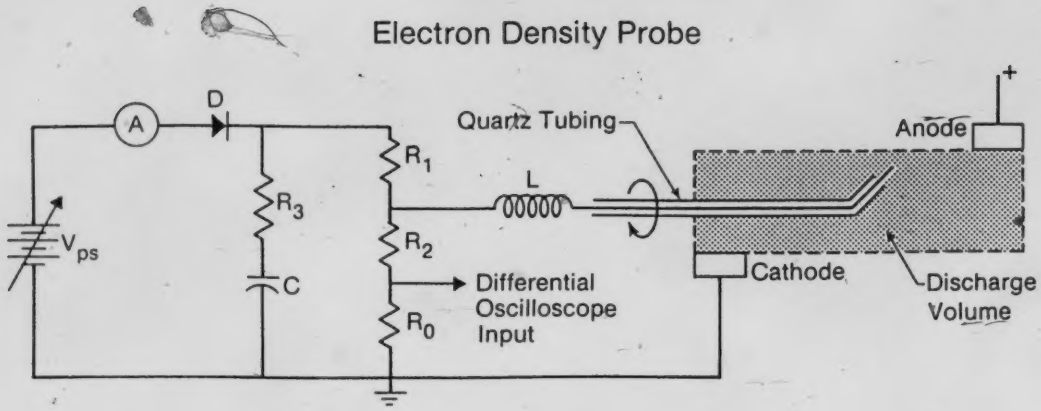

V_{ps}, Variable Power Supply, 0-2000 V_{DC}
C, Isolation Capacitor = 20μF, 3kVDC
R_3, Current Limiter = 120 kΩ, 2W
L, Filter Inductor = 1.16 mH

R_0 = 2.005 kΩ
R_1 = 24.92 kΩ
R_2 = 77.95 kΩ

Fig. 4.20 Electron Density Probe Apparatus

$$V_{probe} = V_{power\ supply} - I_{power\ supply} R_1 \quad \text{and} \tag{4.2}$$

$$I_{probe} = \frac{V_{probe}}{R_0 + R_2} - I_{power\ supply} \cdot \tag{4.3}$$

A knowledge of the floating potential is required, in order to determine the probe-to-plasma potential. By definition, this is the probe voltage for which the probe current is zero.[69] During operation, a series of power supply voltages and currents were recorded. Upon calculating the values of V_{probe} and I_{probe}, the point in the experimental data where $I_{probe} = 0$ may be evaluated by interpolation. The difference between the floating voltage at $I_{probe} = 0$ and the probe voltage for the $I_{probe} \neq 0$ measurements is the bias voltage or probe-to-plasma potential. This is given by:

$$V_{bias} = V_{floating} - V_{probe} \cdot \tag{4.4}$$

Values of V_{bias} and I_{probe} are used in the calculation of electron density.

The plasma, at some distance away from the probe, is assumed to be neutral; being composed of equal numbers of ions and electrons. If the probe is biased sufficiently positive with respect to the plasma, ions will be repelled from the probe. Electrons will however be attracted to the probe; and current will flow from the external circuit to the probe. If the probe is isolated, so that $I_{probe} = 0$, then the probe will be at the "floating" potential. When the probe is negatively biased with respect to the plasma, electrons are repelled. Consequently, current flows from the probe into the external circuitry.

It is desirable to restrict operation to the situation where the probe is biased negative with respect to the plasma. This is done for two reasons. Firstly, a probe biased positively tends to draw large electron currents that perturb the plasma[70], giving questionable results. Secondly, the presence of a magnetic field makes electron current collection a function of probe orientation.[71] A difference in the electron mobility parallel and transverse to the probe is responsible for this effect. This aspect was discussed in section 2.1.4. Because ions are far more massive than electrons, moderate magnetic fields of 500 Gauss will not affect the ion mobility appreciably. Consequently, electron density calculations are based on ion current

collection using a negatively biased probe.

The probe theory developed by Langmuir is particularly useful in the study of very low pressure plasmas, where the ion and electron mean free paths are larger than the probe diameter. In this scenario, the ions and electrons are able to reach the probe in a collisionless fashion. However, at the 5 and 20 Torr pressures used in this experiment, the mean free paths of electrons and ions are much less than the probe radius. Thus, it is necessary to use a high pressure probe theory for a collision dominated plasma sheath. A number of such high pressure probe theories have been developed; each for a specific regime of probe operating conditions.

In the application of this theory, it must first be known if the plasma may be considered stationary. If so, then either the theory developed by Kiel[72] or that by Su and Lam[73] would apply. On the other hand, if the plasma is moving, the theory developed by Clements and Smy[74] would be applicable. In order to resolve this question, a number of dimensionless parameters must be evaluated: the electric Reynolds number (R_e), the Debye number (α), and the dimensionless bias potential (χ).

Evaluation of the electric Reynolds number, R_e, is done to determine if the plasma may be considered stationary. This parameter gives the ratio of the ambipolar ion diffusion velocity to the plasma flow velocity. If R_e is less than 1, then the ions are not being swept out of the probe sheath, and the plasma may be considered stationary. This condition is expressed as:

$$R_e = \frac{v_f 2 r_p e}{\kappa_i k_B T_e} < 1 \quad , \tag{4.5}$$

where v_f, r_p, e, κ_i, k_B, and T_e are the plasma flow velocity, probe radius, electron charge, ion mobility, Boltzmann constant and electron temperature respectively. For the experimental conditions under study, the maximum flow velocity is 10 m/sec. Also, the probe used is constructed of copper wire (AWG 24), with a radius of 0.01 inches ($2.54(10)^{-4}$m). Ion mobility can be calculated using (Eq. 2.24):

$$\kappa_i = \frac{q_i}{m_i \nu_{in}} . \tag{4.6}$$

The average volume weighted mass of the ionized molecules is calculated using Eq. 2.5. From Fig. 4.16, the temperature midway between anode and cathode is estimated to be 610K. The ion-neutral collision frequency is calculated using Eq. 2.6. With these values, the ion mobility is calculated to be 0.0342 m^2/V-sec. Upon substitution into Eq. 4.5, the maximum Reynolds number (at v_f = 10 m/sec) is 0.15; suggesting that for this study, the plasma may be considered stationary.

Having determined that the plasma is stationary, the question remains of whether the thin sheath expression derived by Kiel, or Su and Lam's thick sheath expression is appropriate. An adequate differentiation between these two limits requires knowledge of the remaining two parameters: the Debye number, α, and the dimensionless plasma potential, χ. If $\alpha\chi < 1$, then Kiel's thin sheath expression holds. However, if $\alpha\chi > 1$, then the expression derived by Su and Lam is correct.

The Debye number, or normalized probe radius is given by:

$$\alpha = \frac{\lambda_D}{r_p} = \frac{1}{r_p}\left[\frac{\epsilon_o k_B T_e}{n_o e^2}\right]^{1/2} , \tag{4.7}$$

where λ_D and r_p are the Debye length and probe radius respectively. The parameters ϵ_o and n_o are the permittivity of free space and the charged particle density respectively. As will be discussed in sections 4.3.1 - 4.3.5, the electron density varies between $1(10)^{18}m^{-3}$ and $5(10)^{18}m^{-3}$. With an average value of $3(10)^{18}m^{-3}$, and a typical electron temperature of 1 eV[11], the Debye length is $4(10)^{-6}$m, and the Debye number, α, is 0.02. The normalized probe to plasma potential is given below:

$$\chi = \frac{e}{k_B T_e} V_{bias} . \tag{4.8}$$

For 1 eV electrons, $e/k_B T_e = 1$, and so Eq. 4.8 reduces to $\chi = V_{bias}$.

In principle, either the thin sheath or thick sheath expressions may be used to determine the electron density. However, the repeatability of the experimental data collected is better for bias voltages greater than 100 volts, as is revealed by Fig. 4.27. With

$V_{bias} \geq 100$ V, and a Debye number of 0.02, $\alpha x \geq 2$, and the thick sheath expression is used to evaluate the electron density.

For electron density calculations in the stationary, thick sheath regime the expression derived by Su and Lam is applicable. This is given by:[70]

$$I_{ion} = (4\pi\epsilon_o)^{1/4} (V_{bias} r_{probe})^{1/2} (4\pi n_o k_B T_e)^{3/4} \left[1 + \frac{T_i}{T_e}\right]^{3/4} \kappa_i , \qquad (4.9)$$

where all parameters are as defined previously. An important consequence of the thick sheath regime, is that the ion current does not saturate with increased bias voltage. This is in direct contrast with the very low pressure theory developed by Langmuir.[75]

The expression derived by Su and Lam is for a spherical probe. Since the cylindrical probe used (length of 0.30in = 0.762cm) has a surface area larger than that of a spherical probe of similar radius, Eq. 4.9 must be multiplied by a factor 15.25 to account for the increased collector area of the cylindrical probe.

Upon substitution for the probe radius, ion and electron temperatures, and ion mobility, the electron density (assumed equal to the ion density) for the cylindrical probe in use is given by:

$$n_o = \left[\frac{I_{ion}}{1.5(10)^{-18}(V_{bias})^{1/2}}\right]^{4/3} , \qquad (4.10)$$

where V_{bias} must be at least 100 V for the expression to be valid. This equation is used for all electron density calculations made at 20 Torr in this investigation.

4.3.1 Electron Density: Zero Gas Velocity, Zero Magnetic Field

Initial electron density measurements were made with the probe tip on the axis of the discharge tube. The first two experiments were done with zero gas flow. A study was made of the effect of DC current on the electron density. Fig. 4.21 shows the relationship between ion current and negative bias voltage without magnetic field. Each trace on the curve was done with a fresh gas mixture, to ensure that gas contamination effects did not have a cummulative effect on the data. As seen in Fig. 4.21, higher ion currents are collected at low DC currents than at high DC currents for the same negative bias. Experimental observations of the probe tip during a typical run are as follows.

For negative bias voltages greater than 250V, the probe has a visibly disturbing effect on the plasma. The tip of the probe glows red and instabilities between the probe and the anode are visible in the form of flashes though the bulk gas. For a negative bias of less than 250 V, the sheath around the probe tip is approximately the same thickness as the probe diameter (0.5mm), having a diffuse boundary extending ~1.5mm from the probe. At the floating potential, where the probe voltage and the plasma voltage are equal, the boundaries of the sheath become more clearly defined. For positive bias voltages, the plasma sheath is very sharply defined, and too thin to measure.

The electron density is evaluated in the following manner. For each trace in Fig. 4.21, several points with negative bias voltages greater than 100 V are taken. Upon substitution into Eq. 4.10, consistent values of electron density result, with typical standard deviations of $0.15(10)^{18} m^{-3}$. These are shown in Fig. 4.22. For low DC currents, the electron density is $\sim 6(10)^{18}\ m^{-3}$. It decreases exponentially as DC current increases. At a DC current of 1.5 A, the electron density falls to $\sim 2.4(10)^{18}\ m^{-3}$.

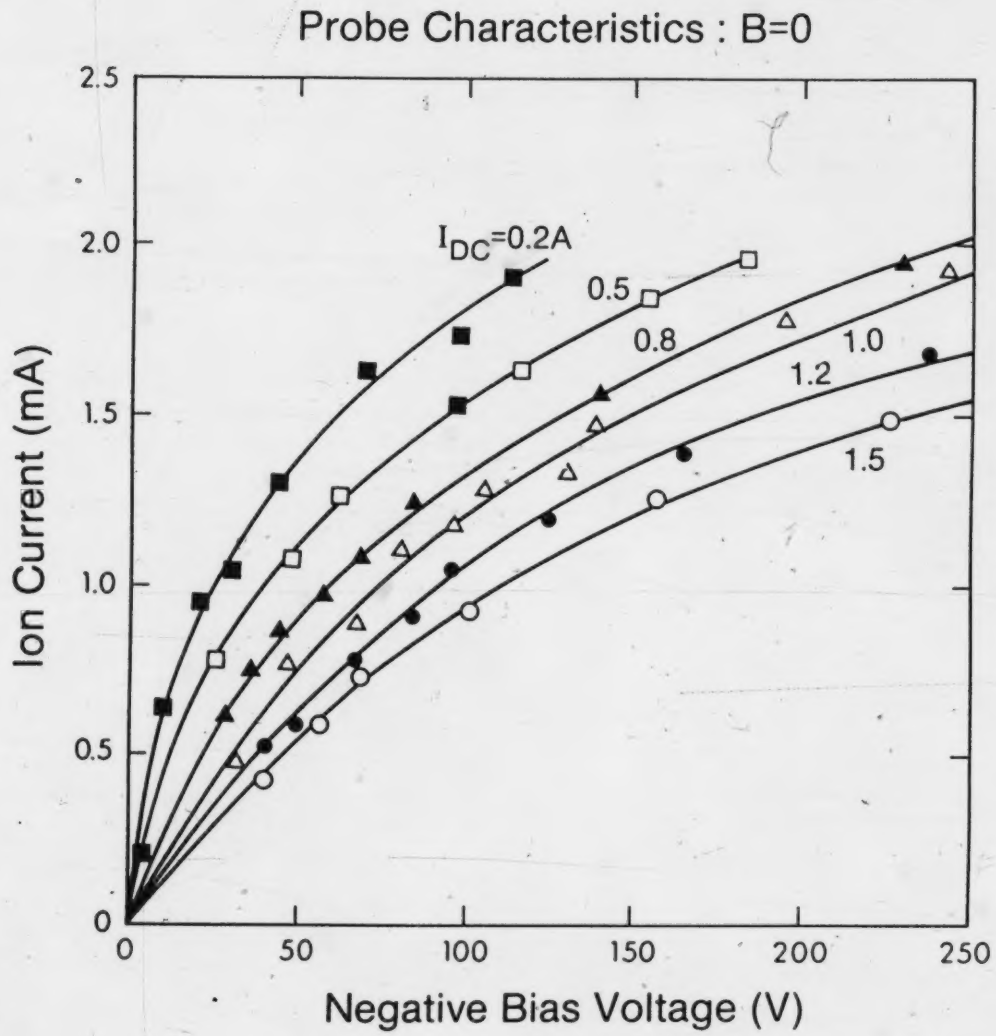

Fig. 4.21 Electron Density Probe Characteristics: B = 0

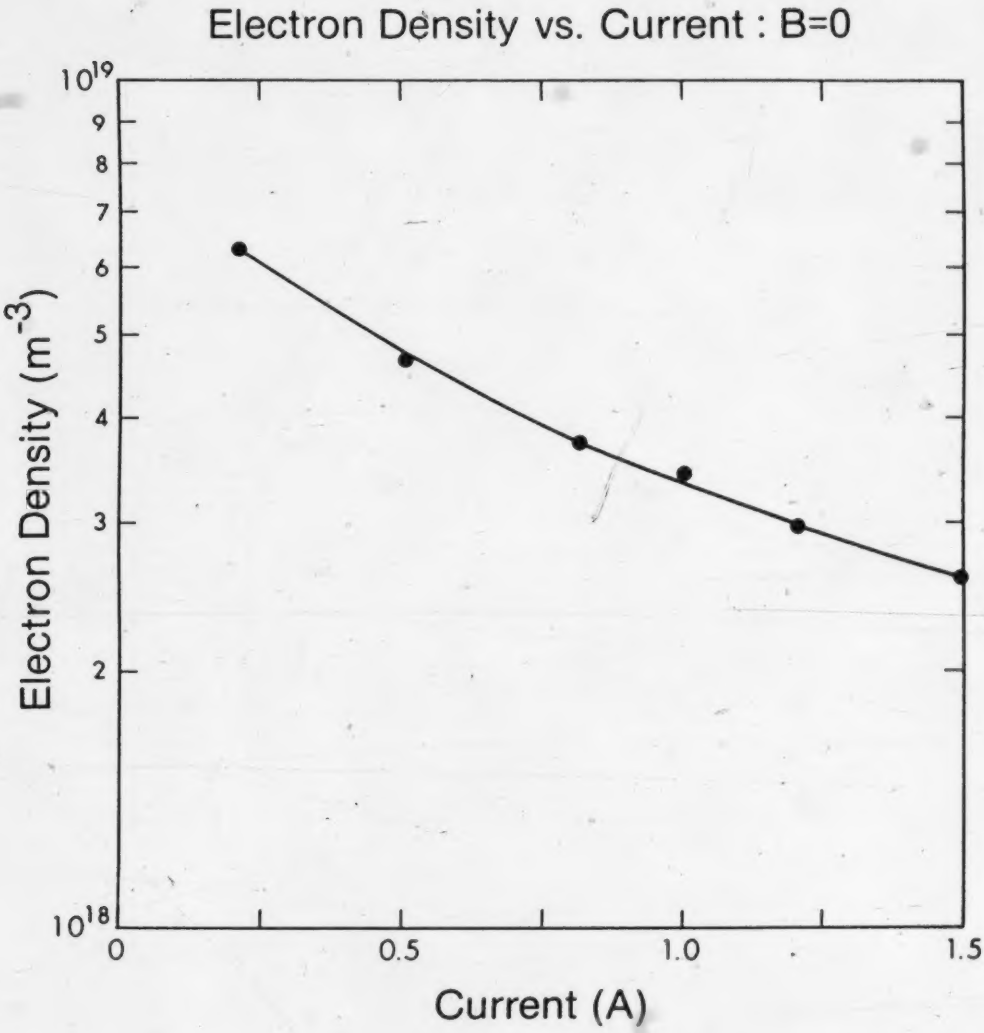

Fig. 4.22 Electron Density vs. Current: B = 0

4.3.2 Electron Density: Zero Gas Velocity, 450 G Rotating Magnetic Field

The previous test was repeated, this time with a transverse rotating magnetic field of 450 Gauss. It was hypothesized that the electron density on axis should decrease, due to the rotating plasma column moving away from the tube axis in the presence of the magnetic field. However, the experimental data obtained with a magnetic field of 450 Gauss, shown in Fig. 4.23, is essentially the same as that in Fig. 4.21 when the magnetic field was not present. Predictably, the electron density, shown in Fig. 4.24, is also similar.

The data obtained thus far raises two questions. Firstly, is the pulser providing such uniform ionization that the presence of the magnetic field has no effect on the electron density? After all, high speed photography has revealed that a plasma column is moving azimuthally through the discharge tube. To answer this question, a radial scanning of the discharge tube was done with the electron density probe. These results are presented in section 4.3.4. The second question pertains to the reason for the exponential decline in electron density as the DC current is increased. This phenomena is explained by recalling the characteristic of the pulser as the load (the plasma) increases in conductivity with increased DC current. The exponential decline in pulser output voltage with increasing DC current was shown earlier in Fig. 3.8. This curve bears a striking resemblance to those of Figs. 4.22 and 4.24. It is believed that the exponential decrease in electron density with DC current is simply a result of the increasing plasma conductivity, and concomitant decrease in pulser efficiency, as discussed in section 3.5.

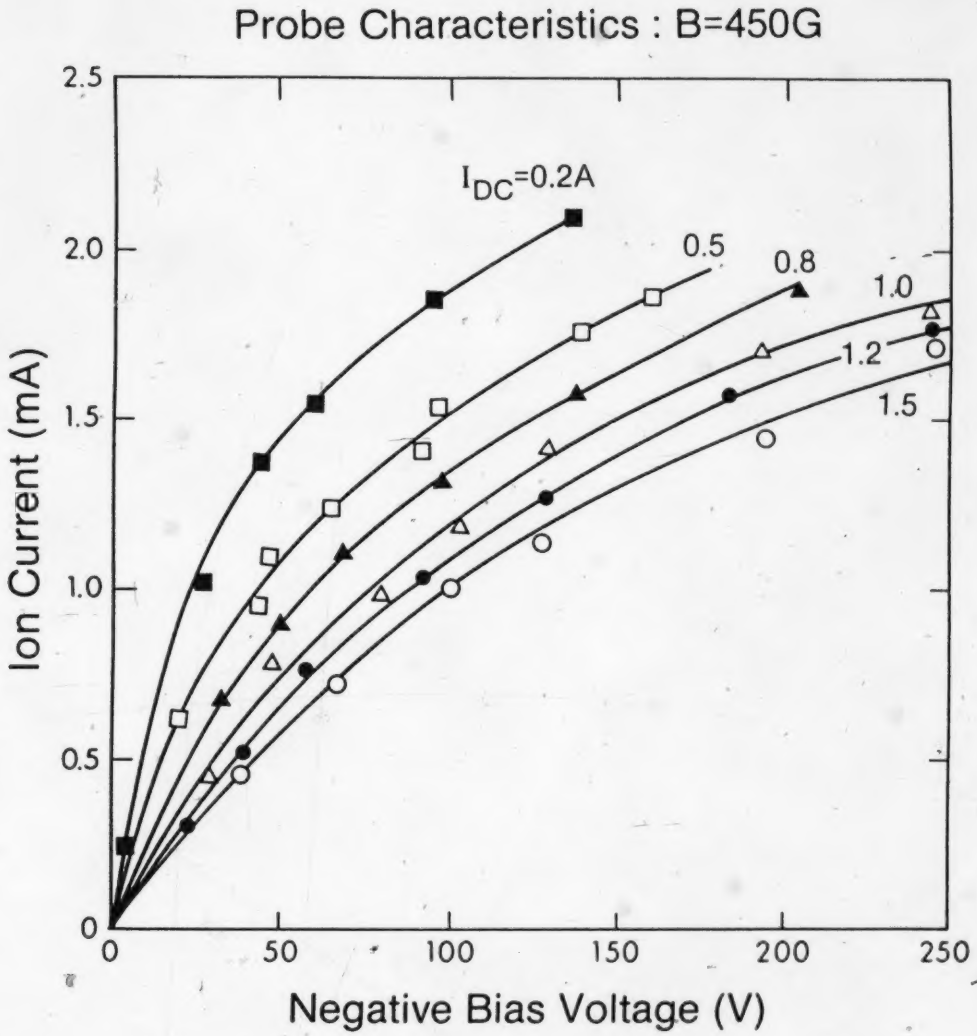

Fig. 4.23 Electron Density Probe Characteristics: B = 450 Gauss

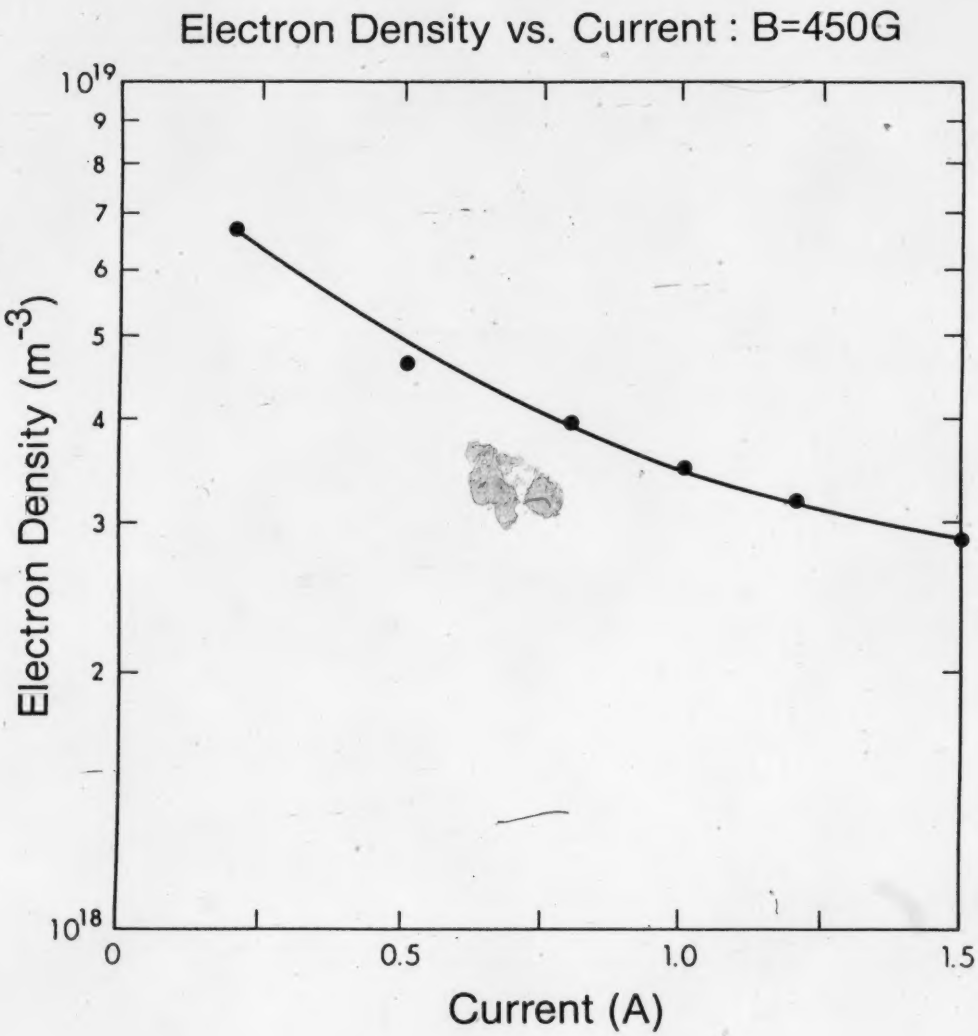

Fig. 4.24 Electron Density vs. Current: B = 450 Gauss

4.3.3 Electron Density: 10 m/sec Gas Velocity

This test was performed both with and without magnetic field. In the case of zero magnetic field, however, the data was of little use. Recall the off-center discharge discussed in the temperature measurements of section 4.2. When the on-axis electron density probe was inserted into the discharge tube, the off-axis discharge was observed to bend towards the probe. Clearly the probe was a disturbance to the discharge and the results of this test were therefore of little value.

However, with the application of the 450 Gauss transverse rotating magnetic field, the discharge became symmetric and on-axis. The ion current vs. negative bias voltage curves for this test are shown in Fig. 4.25. The discharge could not be sustained at a current lower than 0.5 amps. Generally, the ion currents are lower than in the case of zero gas velocity. This is to be expected, since the gas velocity creates an ion loss mechanism, resulting in a lower charged particle density. The electron density for this test is shown in Fig. 4.26. Despite the lower electron density, the exponential decrease in electron density with increased DC current is still apparent.

4.3.4 Electron Density: Radial Variation

The results in section 4.3.2 supported the notion that the pulser was maintaining a uniform ionization with or without the presence of the rotating magnetic field. To investigate this theory, six additional tests were done. For each test the DC current and pulser input voltage were kept at 1 amp DC and 4 kV respectively. At each of three radial values (1, 2.5, 4 cm), two tests were performed, the first with zero magnetic field and the second with a 450 Gauss transverse rotating magnetic field. The results for all six tests are presented in Fig. 4.27. For negative bias voltages greater than 100 V, the clustering of the data about a single curve confirms that the electron density for all six tests has indeed been the same, $(3.5(10)^{18}$ $m^{-3})$. This is the same value predicted by Figs. 4.21 – 4.24 at the 1 amp data points.

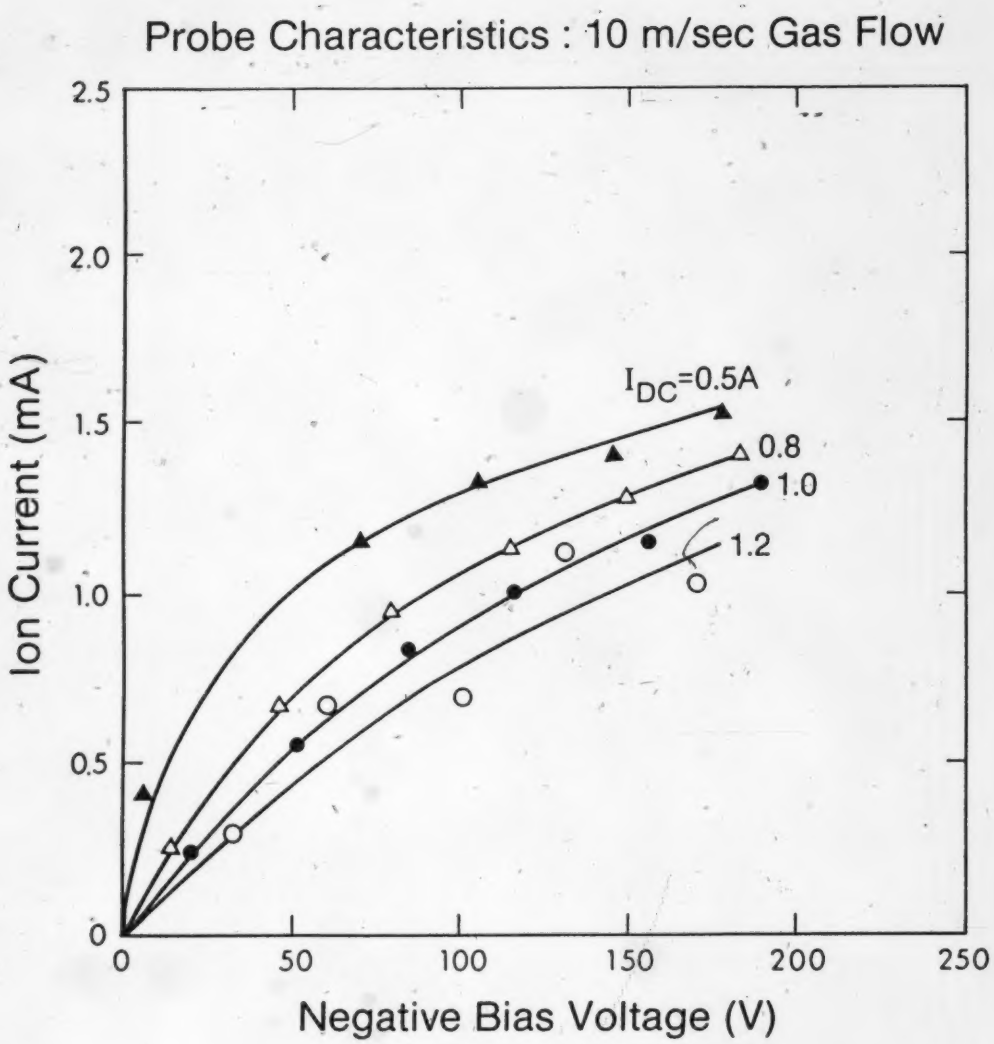

Fig. 4.25 Electron Density Probe Characteristics: 10 m/sec Gas Flow

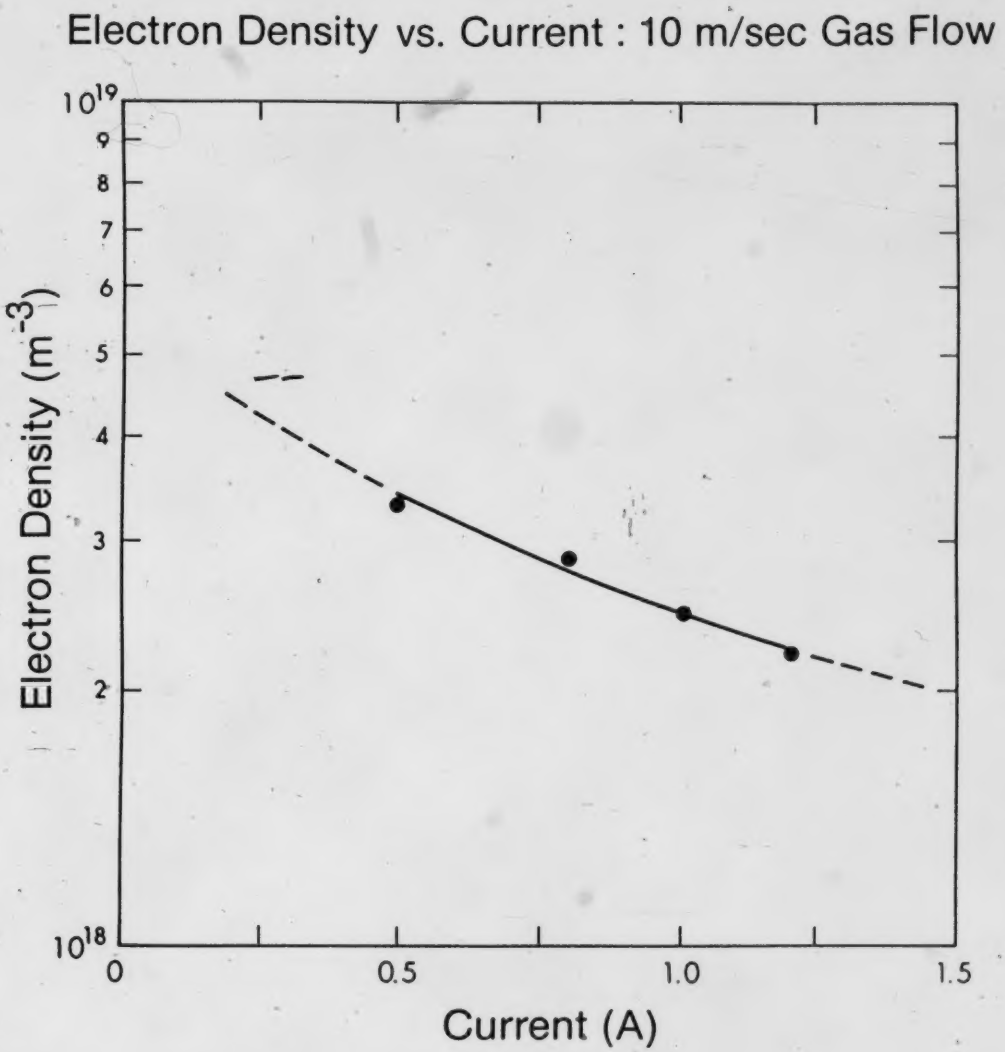

Fig. 4.26 Electron Density vs. Current: 10 m/sec Gas Flow

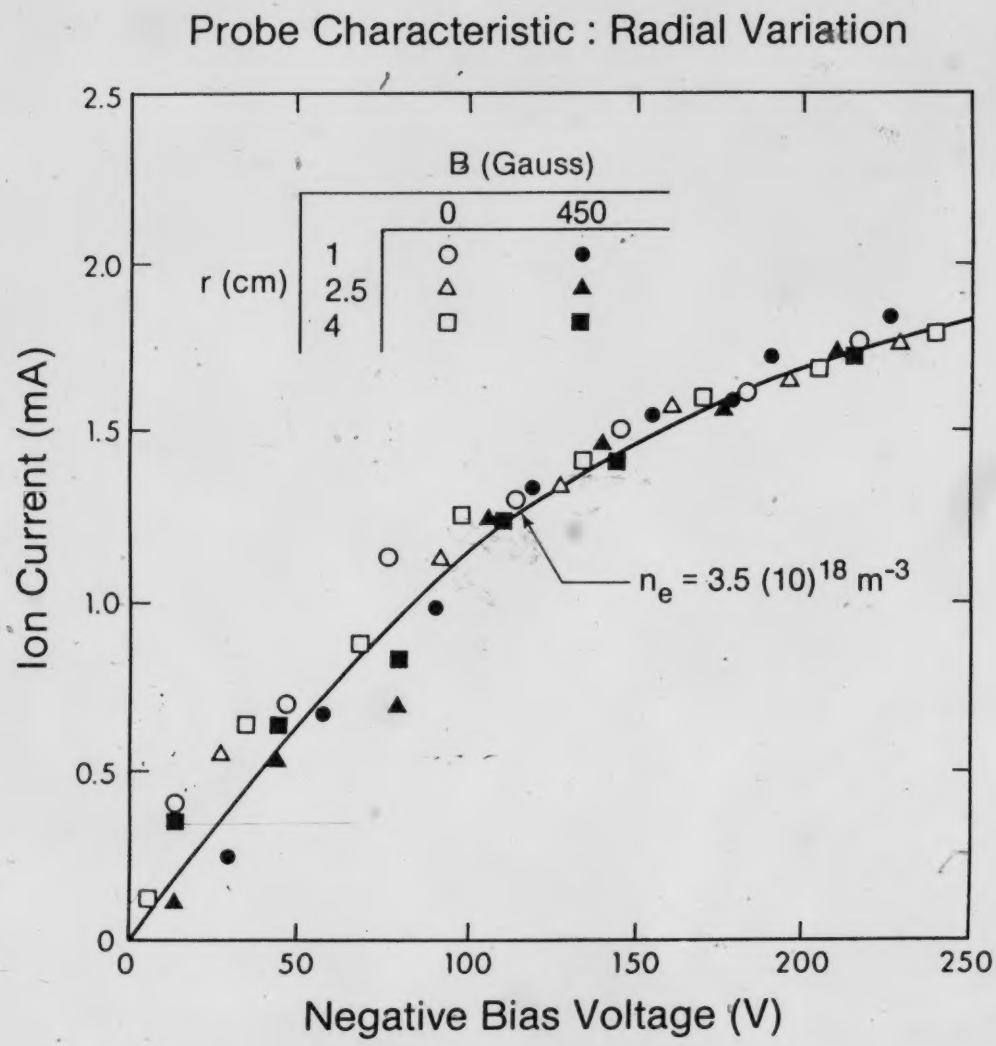

Fig. 4.27 Electron Density Probe Characteristics: Radial Variation

4.3.5 Electron Density: Pulser Variation

The next series of experiments were a study of how the electron density varies with pulser voltage. The test was performed with a variation in pulser input voltage from 2 to 6 kV in 1 kV increments. The discharge was established and maintained at a constant DC current of 1 amp. As with all previous tests, each trace of the ion current vs. negative bias voltage was done with a fresh gas mixture. The first set of measurements were done with zero magnetic field. The experimental results are shown in Fig. 4.28. Based on this data, the electron density variation with pulser input voltage is shown in Fig. 4.29. As expected, the electron density increases for increased pulser input voltage. For a pulser input voltage of less than 2 kV, the plasma could not be sustained. At a pulser input voltage of 2kV, the electron density is $1.5(10)^{18}$ m^{-3}. For an input of 6kV, the electron density is $6(10)^{18}$ m^{-3}, a fourfold increase. The shape of the curve, with its apparent rise to a saturation level is believed to be a pulser effect. For a low voltage input of 2 kV, the pulser produces an output of 9 kV, a multiplying factor of 4.5. At 6 kV, the pulser is only able to produce an output of 12 kV, a reduced multiplying factor of only 2. Thus, as the pulser input voltage increases, the pulser efficiency is decreasing. This accounts for the saturation effect shown in Fig. 4.29.

The previous tests were repeated with the gas discharge being subjected to a transverse rotating magnetic field of 450 G. The ion current vs. negative bias voltage for this test is shown is Fig. 4.30. The resulting electron density is shown in Fig. 4.31. The similarity in results for these two tests support the notion that the pulser is indeed maintaining a uniform ionization throughout the gas discharge tube.

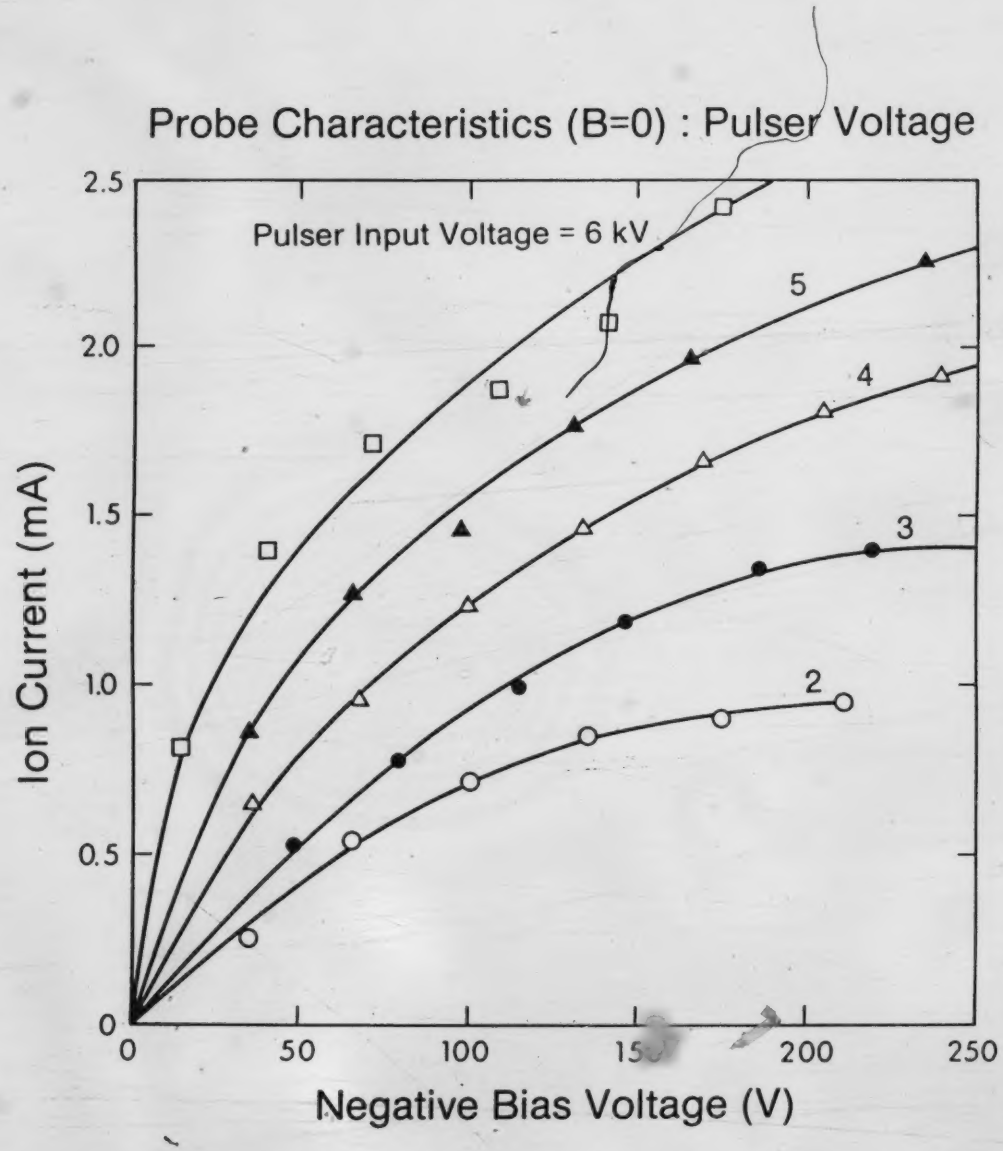

Fig. 4.28 Electron Density Probe Characteristics, B = 0: Effect of Pulser Input Voltage

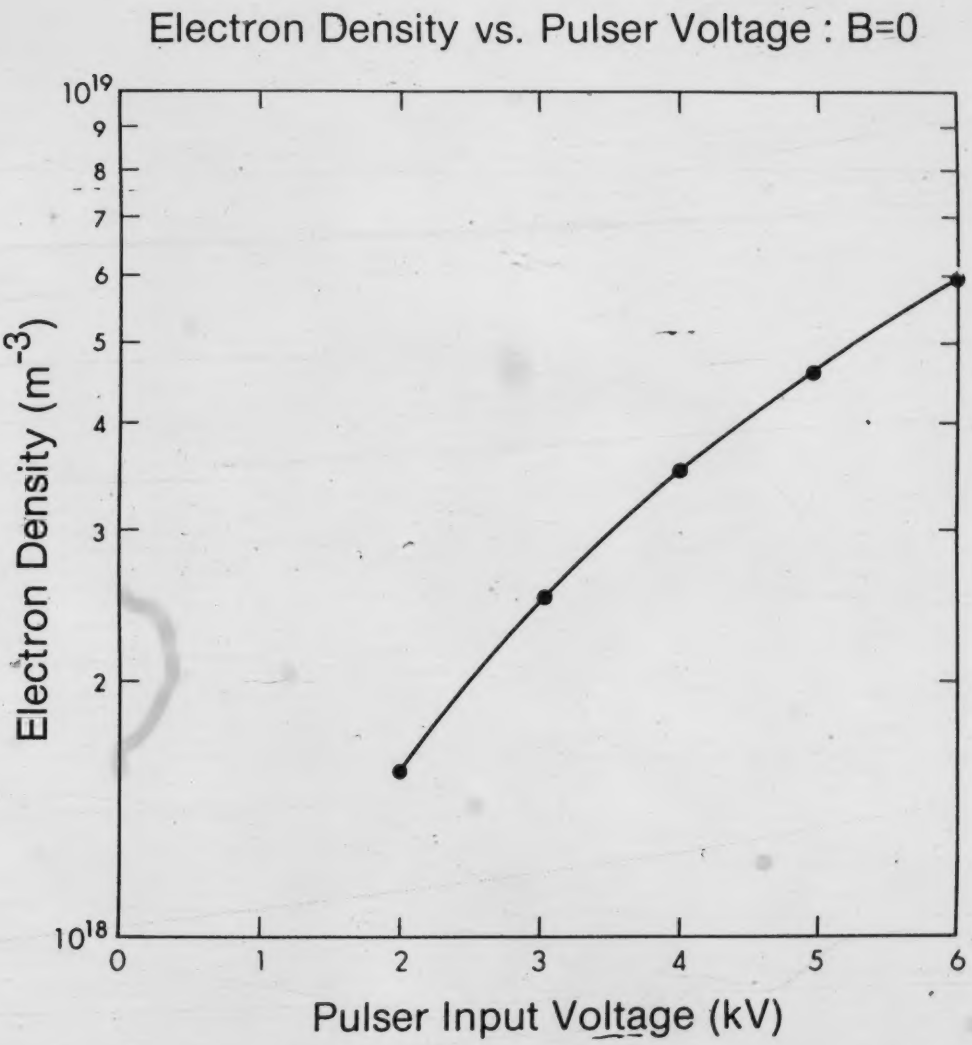

Fig. 4.29 Electron Density vs. Pulser Input Voltage: B = 0

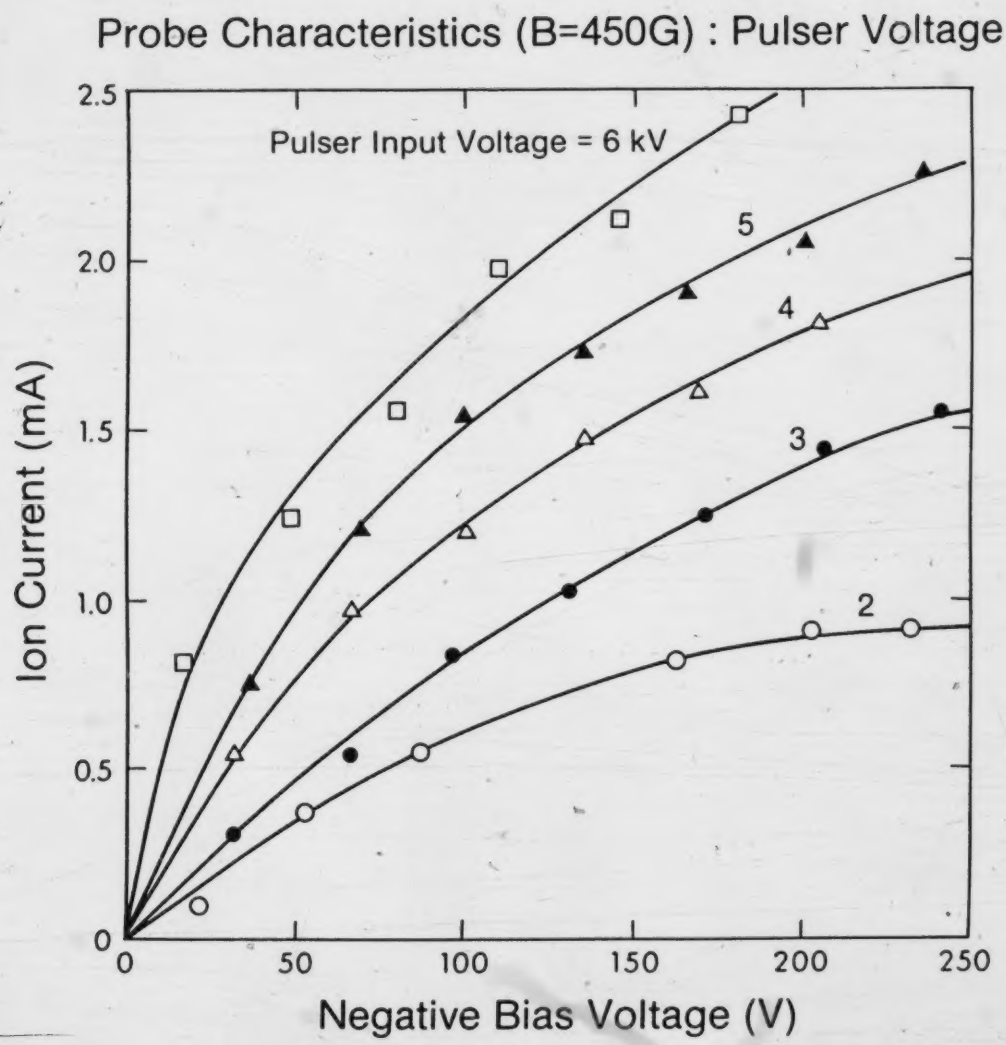

Fig. 4.30 Electron Density ~~Probe C~~haracteristics, B = 450 Gauss: Effect of Pulser Input Voltage

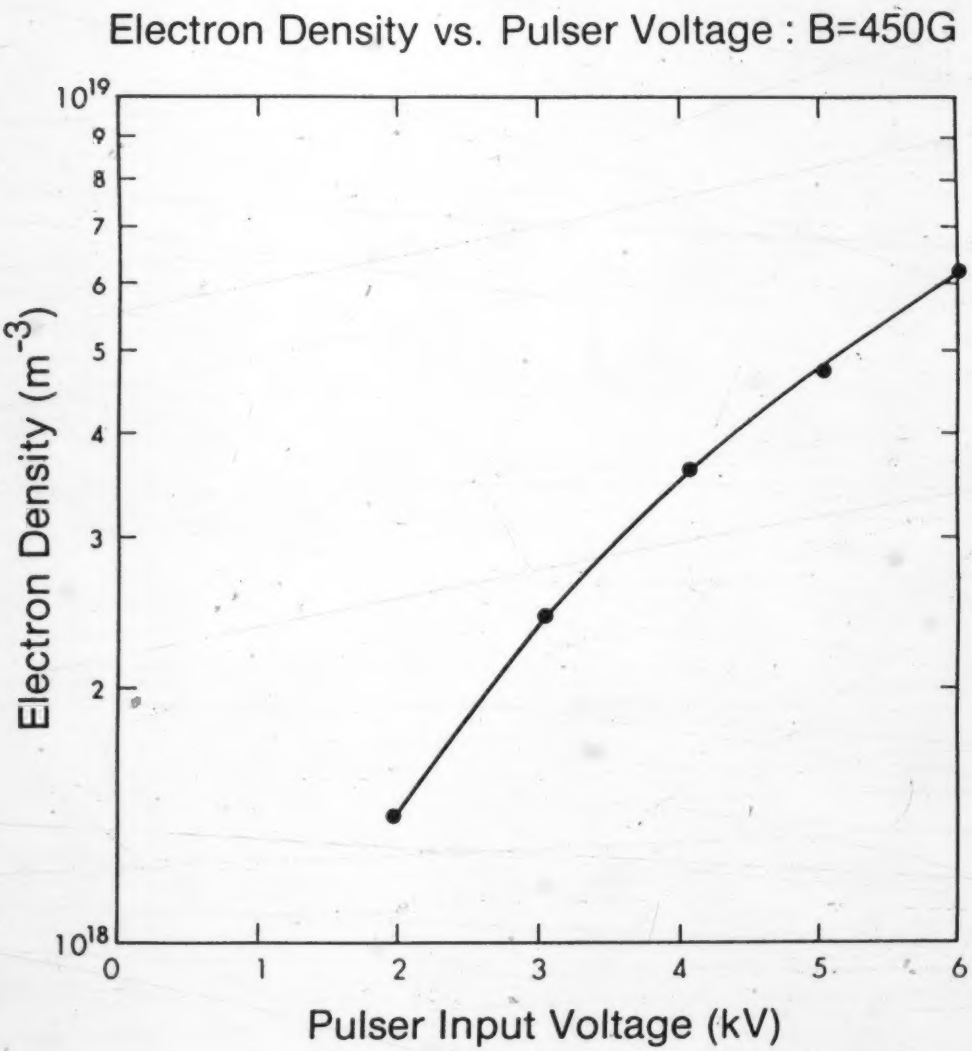

Fig. 4.31 Electron Density vs. Pulser Input Voltage: B = 450 Gauss

4.3.6 Electron Density: Conclusions

The series of tests just discussed appear to indicate that the electron density has no spatial variation. Whether the 450 Gauss transverse rotating magnetic field was energized or not, had no effect on the resultant electron density predicted by Eq. 4.10. This was despite the revelations from high speed photography that showed the gas discharge to be a rapidly rotating plasma column sweeping azimuthally around the discharge tube at the angular velocity of the rotating magnetic field. These aspects suggest that the pulser pre-ionization system may be masking out the spatial variations in electron density.

Consider the following scenario: The pre-ionization system is creating electrons and ions. However, owing to the high voltage impulses that produce this ionization, the electrons have high average energies. In order to collect an ion current from the negatively biased probe, these high energy electrons must be prevented from entering the ion sheath that surrounds the probe tip. Thus, as seen in the previous measurements, it is necessary to strongly bias the probe.

Now consider a second source of electrons, such as those from the sustainer DC power supply. Without the pulser, the sustainer supply is incapable of maintaining the necessary ionization to sustain the plasma. Hence, the electrons from the sustainer supply have low average energies. Because the probe is biased so as to reject the high energy electrons from the pulser, the low energy electrons never get near the probe, and are therefore never detected. This would account for the lack of spatial variation in electron density in the measurements. To test this hypothesis, an electron density measurement was made at a lower pressure, where the sustainer supply alone was able to maintain the discharge, without the need for external ionization. The results of this experiment are described in the following section.

4.3.7 Electron Density: Measurements at Low Pressure (5 Torr)

The previous tests done at 20 Torr showed that the pulser either effectively controlled the electron density or masked out any effects of the rotating plasma column. Thus, a study was needed of the electron density spatial variation without the preionization provided by the pulser. This left two options; either the 20 Torr test would have to be done at much higher voltages, in order to self-sustain the discharge, or else a lower pressure test would need to be done. Due to power supply and apparatus limitations, the low pressure (5 Torr) approach was taken.

The test apparatus is the same as that shown in Fig. 4.20. Because the voltage on the probe has a large DC component with a small superimposed AC component, a differential type of measurement is required. In order to get good resolution, a maximum voltage of 50 V is required for the differential oscilloscope in the laboratory. Thus, a 2 kΩ resistor, R_0, is placed in series with the 78 kΩ resistor; as shown in Fig. 4.20. When V_{probe} and I_{ion} are defined as the voltage and the ion current collected by the negatively biased probe, the following relations result:

$$V_{probe} = V\left[1 + \frac{R_2}{R_0}\right] , \tag{4.11}$$

$$I_{ion} = V\left[\frac{R_1 + R_2}{R_0 R_1} + \frac{1}{R_1}\right] - V_{power\ supply}\left[\frac{1}{R_1}\right] , \tag{4.12}$$

where V is the voltage across R_0, (the input to the differential oscilloscope). Substitution for R_0, R_1 and R_2 yields:

$$V_{probe}(V) = 39.875\ V\ , \text{ and} \tag{4.13}$$

$$I_{ion}\,(mA) = 2.099\ V - 0.040\ V_{power\ supply} . \tag{4.14}$$

For the 5 Torr experiment, the gas mixture has the same percentage contribution as that used at 20 Torr; ($CO:CO_2:N_2:He$ = 0.25:0.25:1:3.5 Torr for a 5 Torr total). At this pressure, a magnetic field of 450 Gauss is enough to push the discharge into the wall and extinguish it. Hence, the magnetic field was reduced to 100 Gauss. This is sufficient to spread the discharge, but not to the point of what appears to the naked eye, to be an annulus. As the

gas transport system provides little axial gas flow at this low pressure, the test was done under no flow conditions. With a magnetic field of 100 Gauss, the operating voltage is 1400 V with a DC current of 0.5 amps. At a point midway between the anode and cathode the plasma voltage is estimated to be 750 V. This was arrived at in the following manner. At a DC current of 0.5 A, the voltage drop across the 600 Ω fluid ballast resistor is 300 V. This leaves a plasma voltage of 1100 V. The cathode fall voltage is roughly 400 V.[76] Thus the voltage drop across the positive column is 700 V. Across half of the positive column the voltage drop is 350 V. Since voltages are referenced to ground, the plasma voltage at the midpoint is 350 + 400 = 750 V. With the electron density power supply set at 640 V, a voltage of ~500 V appears on the electron density probe. This gives a negative bias voltage, V_{bias}, of 250 V, between the probe and the plasma.

The probe characteristics, as displayed on the differential oscilloscope are shown in Fig. 4.32 for radii of 1, 2.25 and 4.5 cm. The amplitude of 0 mV corresponds to the point where the differential amplifier is providing a DC offset of 12.54 V. Hence, the voltage across R_0 varies from 12.54 V to 12.84 volts at its maximum.

Eqs. 4.13 and 4.14 are used to evaluate the probe voltage and ion current. Assuming a constant bias voltage of 250 V, the relation between ion current, bias voltage, and electron density given by Eq. 4.10 is applied. (In using Eq. 4.10, we must account for the ion mobility at 5 Torr being 4 times that at 20 Torr.) The spatial variation of electron density is graphically displayed in Fig. 4.33. This figure is created in the following manner. First, the horizontal time scale in Fig. 4.32 is redrawn as the circular time scale in Fig. 4.33. Three circles corresponding to radii of 1, 2.25 and 4.5 cm are drawn, centered on the "+" in Fig. 4.33. In this manner, points may be plotted as to their time and radial locations. Each trace in Fig. 4.32 is then divided into 50 mV segments. The electron density at the midpoint of each of these 7 segments is then plotted on Fig. 4.33. Once all time-radius points are plotted, contour lines are drawn to separate the drawing into 7 levels of electron density, thereby resulting in a contour plot of the plasma column for a "snapshot" in time.

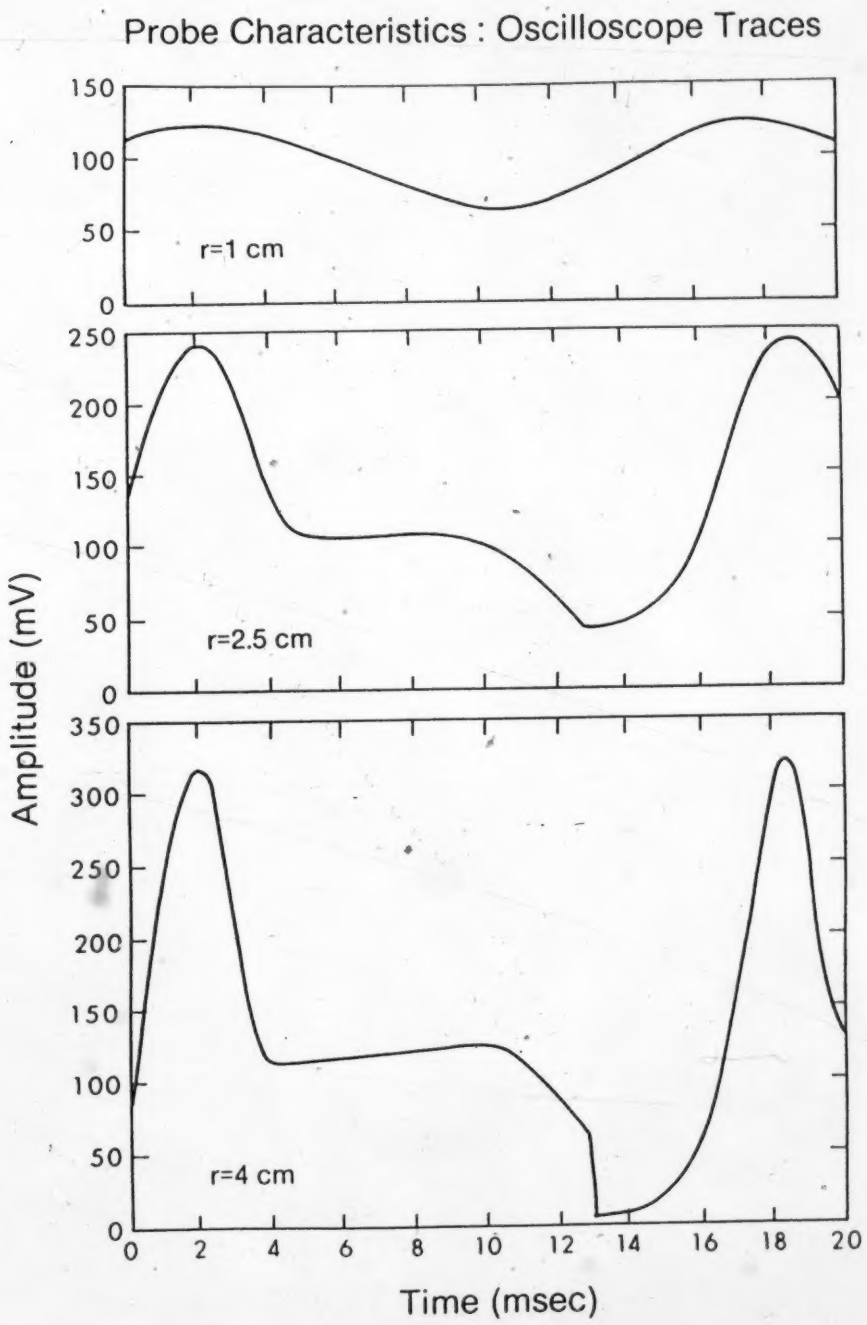

Fig. 4.32 Electron Density Probe Characteristics at 5 Torr: Oscilloscope Traces

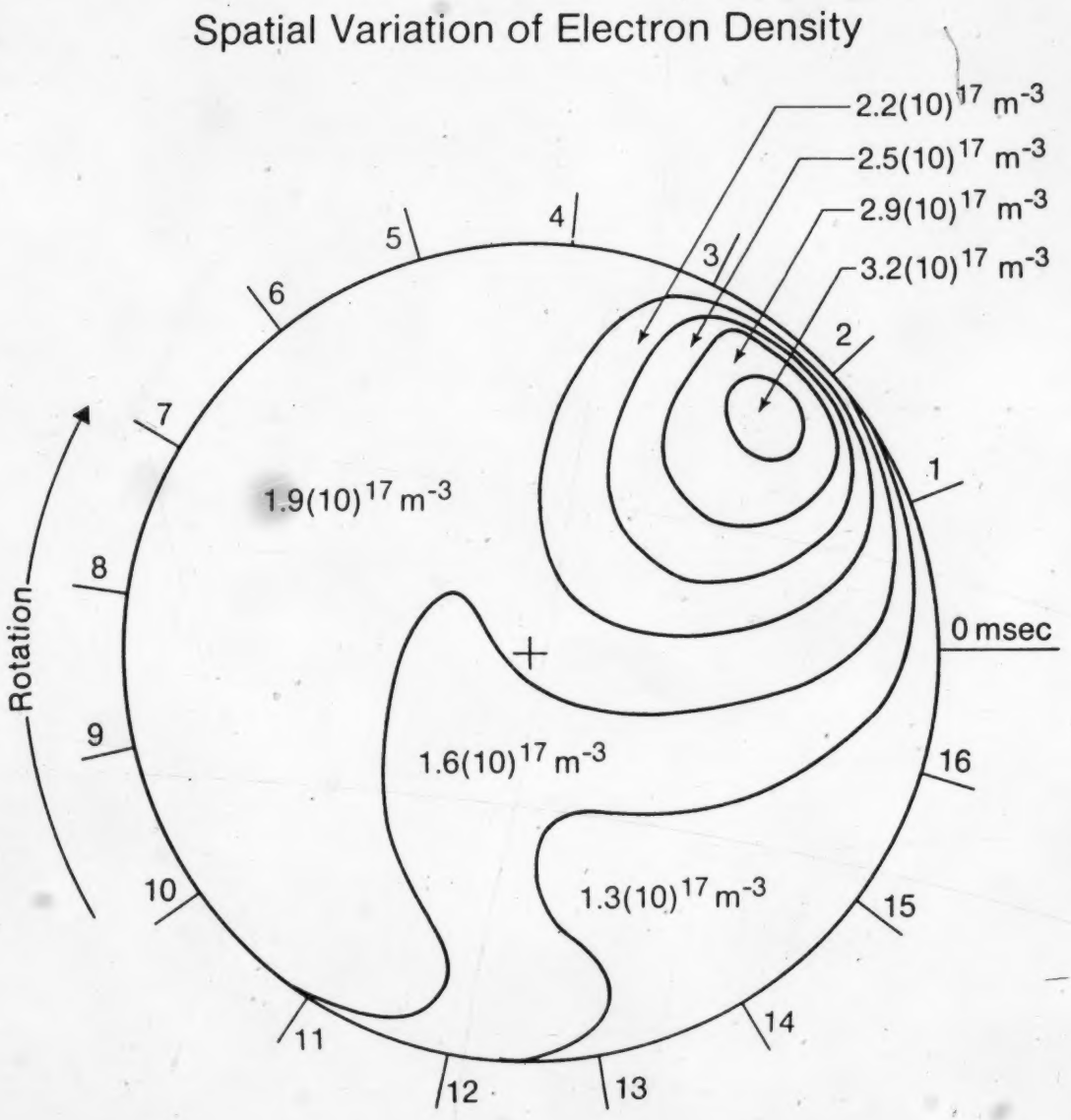

Fig. 4.33 Spatial Variation of Electron Density at 5 Torr

There are two noteworthy points regarding Fig. 4.33. Firstly, while the electron density is understandably highest at the location of the plasma column, the density at other locations of the cross-section does not fall to zero. In fact, the ratio between the highest and lowest electron density over the entire cross-section is roughly 2.5. Thus, despite the forces that result with the introduction of the transverse rotating magnetic field, current still flows in all regions of the cross-section. This is the only conclusion that may be drawn. Without the ionization provided by the DC current, the electron density would decay to zero in a fraction of a millisecond at this pressure.[77] Thus, in order to maintain the lowest observed density of $1.3(10)^{17}$ m^{-3}, some current must still be flowing through this region.

The second noteworthy point is that an electron density of $1.9(10)^{17}$ m^{-3} exists over roughly half of the discharge cross-section. Most of this uniform region is the tail that forms behind the electron density peak as it executes its circular motion. (Note the direction of rotation in Fig. 4.33.) This region of fairly uniform electron density may prove to be a uniform region of laser pumping. If the angular velocity of the plasma was increased, (even if only by a factor of two), by using a faster rotating magnetic field, the electron density may remain quite uniform, except for the peak of electron density that would still result when the plasma column is swept through.

CHAPTER V

GAIN OPTIMIZATION, SATURATION INTENSITY AND LASER POWER

The most important parameter in laser gas discharge studies is the amplifying quality of the gain media. In this chapter, the effects of magnetic field, applied DC voltage and pulser input voltage on gain will be presented. Next, tests to evaluate the small signal gain and saturation intensity are detailed. These data are particularly important since the maximum available optical power density of a gas discharge is directly related to the product of these two parameters.[3] This is followed by a brief section describing the laser power output experiments and results.

5.1 Gain Optimization

As discussed in section 1.2, the population inversion in a gas discharge follows as a result of the following energy exchange relations.[10]

$$e + N_2(v=0) \rightarrow N_2(v=n\leq 8) + (e - K.E.) \text{ , and} \tag{5.1}$$

$$N_2(v=n) + CO_2(00^00) \rightarrow N_2(v=n-1) + CO_2(00^01) \text{ , or} \tag{5.2}$$

$$e + CO_2(00^00) \rightarrow CO_2(00^01) + (e - K.E.) \text{ .} \tag{5.3}$$

In this context, gain optimization may be considered to be primarily the maximization of the inelastic collision process for vibrational excitation, given by Eq. 5.1. Direct excitation of the $CO_2(00^00)$ by inelastic collisions (Eq. 5.3), plays a lesser role.[11] Much work has been done to identify the particular discharge parameters that provide for maximum power deposition into the upper laser level, $CO_2(00^01)$.[24,78,79] The percentage of discharge power actually used for vibrational excitation of the upper laser level, is shown in Fig. 5.1, as a function of E/N, for a typical gas mixture. The efficiency of upper laser level excitation is seen to be a peaked function of E/N; with the optimal point of operation being $\sim 10^{-16}$ V-cm^2. For E/N values less than optimum, few electrons in the gas discharge acquire sufficient energy for the

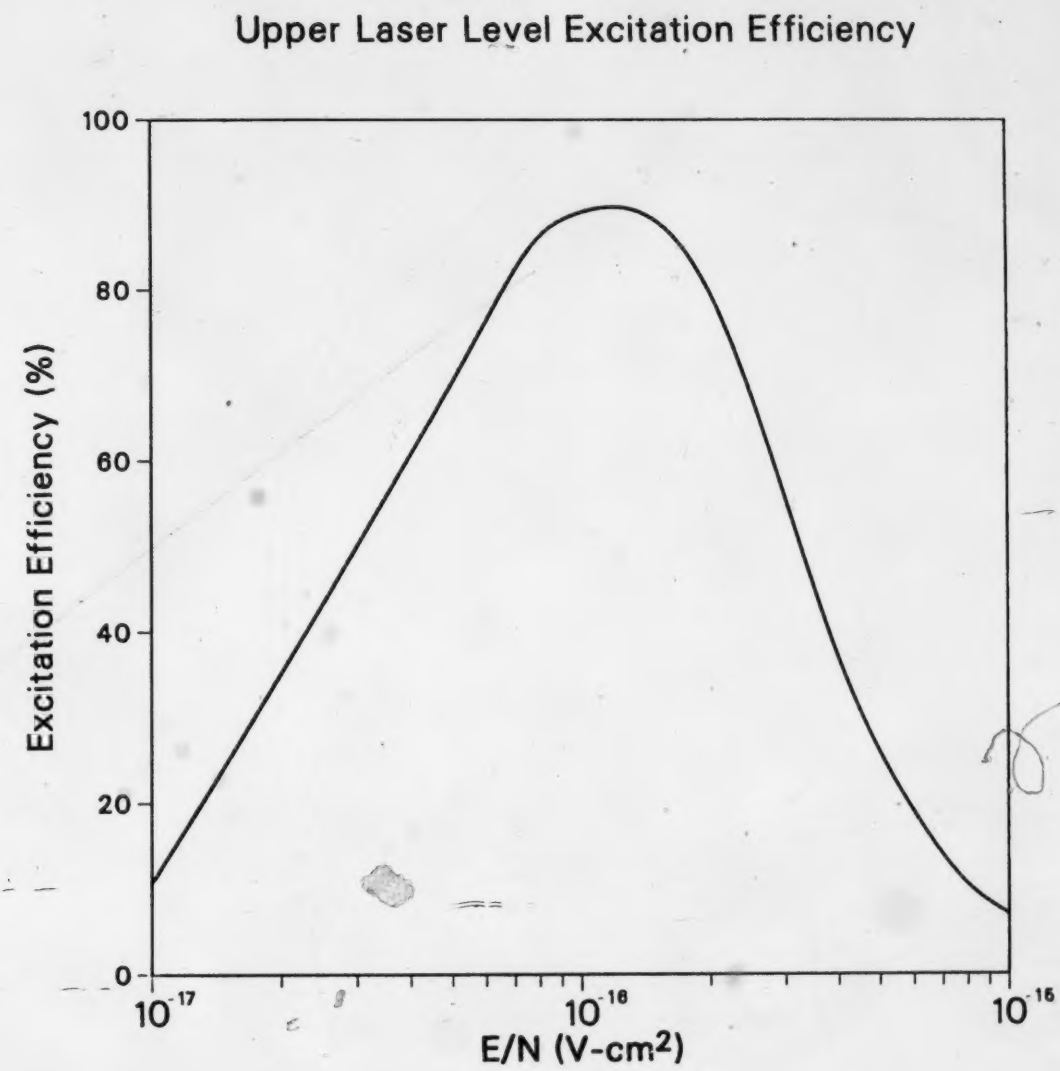

Fig. 5.1 Percentage of Power Input Transferred to the Upper Laser Level[24]

inelastic collisions of interest (Eqs. 5.1 and 5.3). As a consequence, only elastic collisions occur, with concomitant gas heating. Operating at a higher E/N than optimum also decreases the efficiency of excitation to the upper laser level. Under such conditions, the cross-section for inelastic excitation of nitrogen molecules is greatly reduced. Thus, the bulk of the discharge power is lost to electronic and ionizational phenomena.[11] Based on this discussion, and with a sufficiently low gas temperature, the gain should then be an increasing function of the DC supply voltage, until an E/N of $\sim 10^{-16}$ V-cm^2 is achieved. Increasing the DC supply voltage beyond this point should result in a decreasing gain.

In calculating the E/N of the gas discharge, it is important to realize that the electric field, E, represents only that portion of the externally applied field that is actually impressed across the positive column of the gas discharge. Thus, the voltage losses associated with the cathode and anode falls must be accounted for, when evaluating the electric field. Hence:

$$E = \frac{V_{\text{positive column}}}{d} = \frac{V_{\text{terminal}} - V_{\text{cathode fall}} - V_{\text{anode fall}}}{d} , \tag{5.4}$$

where d is the length of the gas discharge. E/N is therefore given by:

$$\frac{E}{N} = \frac{k_B T}{P} \left[\frac{V_{\text{terminal}} - V_{\text{cathode fall}} - V_{\text{anode fall}}}{d} \right] . \tag{5.5}$$

The cathode fall voltage, as determined by Ivanchenko and Shepelenko, for a CO_2 laser gas discharge, is 400 ± 20 V at a pressure of 2.7 kPa (20.25 Torr).[76] The anode fall voltage is in the order of the magnitude of the ionization potential of the gas.[48,80] This varies between 13.79 eV for CO_2 and 24.59 eV for He.[18] A combined anode and cathode fall voltage loss of 420 V is therefore reasonable. With an optimal E/N value, the input electrical energy deposition to vibrational excitation of N_2 molecules is maximized, and the initial gas temperature rise is minimized. For a temperature of 25 °C, a pressure of 20 Torr, and a discharge length of 0.5 m, Eq. 5.5 becomes:

$$\frac{E}{N}(\text{V-cm}^2) \sim 3.1(10)^{-20} (V_{\text{terminal}} - 420) . \tag{5.6}$$

5.2 Gain Measurement Theory and Apparatus

The theory of gain measurement is well established. A low power CO_2 probe laser is passed through the gas discharge and then into a suitable detector. Gain of the amplifying media is calculated by relating the detector signals, when the gas discharge is off, to when it is on. If the detected signal is amplified when the discharge is on, then there is gain. If the converse situation is experienced, then the gas discharge is exhibiting absorption.

Since the probe laser beam encounters the same window and mirror losses, whether the discharge is on or off, these parameters cancel when comparing the detected signals. Thus, the following relatively simple expression for gain results.[10]

$$I_{on} = I_{off} e^{\alpha L} , \tag{5.7}$$

where I_{on} and I_{off} are the detected probe laser beam intensities when the gas discharge is on and off. The quantities α and L are the gain coefficient and total length of the gain path respectively. (For the two pass gain measurement described below, L = 1 m; double the length of the gas discharge.) Rearranging Eq. 5.7, and solving for the gain coefficient yields:

$$\alpha = \frac{1}{L} ln\left[\frac{I_{on}}{I_{off}}\right] \tag{5.8}$$

Gain measurement theory is quite simple. However, in practice there are additional complications. Apparatus used for the gain measurements is shown in Fig. 5.2. The probe laser produces a 40 W TEM_{00} CO_2 laser beam which passes through a variable attenuator constructed of two counterrotating polished salt (NaCl) flats. These salt flats attenuate the beam by altering the angle of incidence of the incoming beam, thereby changing the transmissive properties of the attenuator. However, the attenuator does not alter the beam propagation path. One gain test requires that the probe beam be scanned across the discharge cross-section. Thus, after leaving the attenuator, the probe beam is reflected off two mirrors mounted on a precision translation unit. The second mirror deflects the beam through a ZnSe (Zinc Selenide) window and then through the gas discharge. After being reflected by an adjustable mirror, the beam is sent back through the gas discharge for a second time. It again

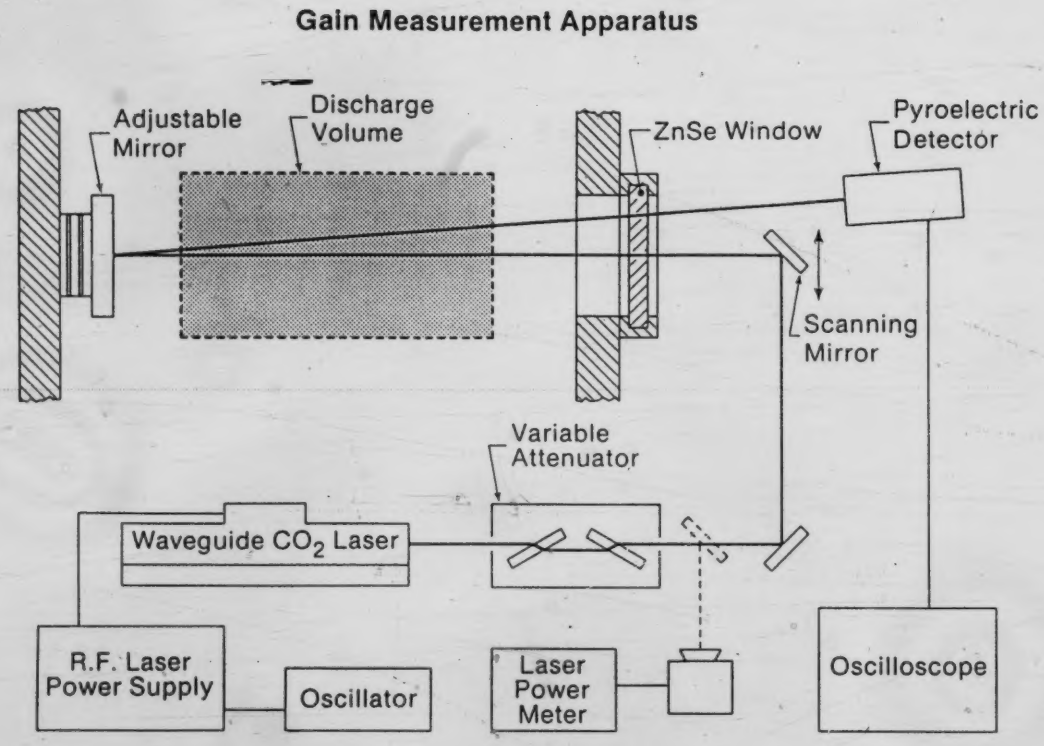

Fig. 5,2 Gain Measurement Apparatus

passes through the ZnSe window, and then enters a fast-response pyroelectric infrared detector (Molectron J3-05), which is also mounted on the translation stage. An oscilloscope displays the output of the detector.

The use of a pyroelectric detector necessitates the modulation of the probe laser beam. Often, this is done with a chopper wheel; a spinning disk with notches, which is placed in front of the probe laser. However, the waveguide laser used (Laakmann RF-125), is excited by an R.F. laser power supply (Laakmann RF-250), with provisions for modulating the laser on and off. The modulation frequency and pulse width used are 1kHz and 100 μsec respectively.

5.3 Burst Pulse Gas Discharge Technique

Measurements in section 4.2 showed that the outlet gas temperature is typically above 600 °C. At this elevated temperature, the discharge becomes an absorbing media, as shown by Robinson.[81] Numerous researchers have shown that the gain is inversely dependent on gas temperature. Bullis demonstrated that at gas temperatures above 600K, the gain falls below practical, useable limits[16], due to the "thermal bottlenecking" phenomena discussed earlier.

Clearly, the gain measurements for the axial gas discharge described herein need to be completed before a significant increase in the gas temperature occurs. One option is to operate the discharge in a pulsed mode. However, the properties of a pulsed laser differ markedly from those of a CW device.[82] Besides that, the pulse width of a pulsed laser is much shorter than the time scale for changes in the transverse rotating magnetic field. A second possibility is to increase convection cooling by increasing the axial gas velocity, so as to reduce the residence time of the gas.[83] This latter solution was not feasible with the present system.

The final resolution to the dilemma is the use of a burst gas discharge technique, developed by S.K. Nikumb.[84] With this method of gain measurement, the device is operated as a CW gas discharge, but only for a short time. A long cooling cycle follows, to allow for gas temperature recovery. The magnetic field rotates at 3600 RPM or 16.7 msec/revolution, and so it is necessary to have the discharge operate for ~17 msec in order to study the

transverse rotating magnetic field effects on the discharge.

An estimate of the cooling time needed for temperature recovery necessitates an analysis of the heat equation. Consider the worst case situation, where there is no heat convection or transport of the hot gas out of the discharge region. That is, the only heat removal mechanism entertained is radial conduction to the wall by thermal diffusion. The applicable heat equation for these circumstances is given by:[85]

$$[\vec{\nabla}\cdot(\lambda\vec{\nabla}T)]_r + \dot{q} = \rho c_p \frac{\partial T}{\partial t} , \tag{5.9}$$

where T, $\dot{q}$, λ, ρ, c_p and t are the temperature, rate of heat generation per unit volume, thermal conductivity, mass density, thermal capacity and time respectively. In that only a gross approximation of the thermal recovery time is required, the thermal conductivity will be taken as constant to simplify the analysis, allowing Eq. 5.9 to be written as:[86]

$$(\nabla^2 T)_r + \frac{\dot{q}}{\lambda} = \frac{1}{\gamma}\frac{\partial T}{\partial t} , \tag{5.10}$$

where γ is the thermal diffusivity ($\lambda/\rho c_p$). The parameter of interest is the time for thermal recovery, so $\dot{q} = 0$, and Eq. 5.10 reduces to the Fourier equation for heat conduction:

$$(\nabla^2 T)_r = \frac{1}{\gamma}\frac{\partial T}{\partial t} . \tag{5.11}$$

An approximate solution to the Fourier equation is obtained by replacing $(\nabla^2 T)_r$ its finite difference approximation:[87]

$$(\nabla^2 T)_r \sim \frac{1}{R^2}(T_{wall} - 2T_{axis} + T_{wall}) , \tag{5.12}$$

where R is the radius of the discharge tube. Upon substitution into Eq. 5.11, and integrating, T_{axis} is given by:

$$T_{axis} = T_{wall} + (T_{axis,initial} - T_{wall})e^{-t/\tau} , \tag{5.13}$$

$$\text{where} \quad \tau = \frac{R^2}{2\gamma} . \tag{5.14}$$

The parameter τ is the characteristic time for temperature recovery.

Thermal conductivity and mass density are both functions of temperature. This aspect was discussed in section 2.1. For a temperature of 150°C, a 20 Torr (1:1:4:14) gas mixture has a thermal conductivity, λ = 0.101 W/m-K, a mass density, ρ = 0.0091 kg/m^3, and a heat capacity, c_p = 1962 J/kg-K. The thermal diffusivity, γ, is 0.006 m^2/sec, and so with a tube radius of 0.05 m, the characteristic time for temperature recovery, τ, becomes 0.2 sec. To allow for complete temperature recovery, the cooling cycle for the burst discharge was set to 0.8 sec. This allows for a 98% recovery of the gas discharge temperature.

Experimentally, the burst discharge technique involves triggering of the thyratron at 5 kHz, for a duration of 17 msec; and then not triggering for 800 msec. This was accomplished with an external sweep/function generator (B&K Precision 3020), used as an external input to the thyratron driver. Provided that the DC supply voltage is of sufficient value, a CW discharge results for a 17 msec duration. The gas discharge then extinguishes for 800 msec; but only if the DC supply voltage is below the threshold for self-sustained operation. Gain measurement involves comparing the pyroelectric detector outputs during the time that the discharge is on and off; and then substituting the measured data into Eq. 5.8 to evaluate the gain coefficient, α.

5.4 Gain Measurements

With the burst gas discharge technique in operation, and the gain measurement apparatus in place, a series of gain measurements where taken. To avoid complications such as off-center discharges, the gain tests were all done with zero axial gas flow velocity. With 800 msec allowed between bursts for temperature recovery, excessive gas heating does not occur; this provided, however, that the discharge remains extinguished between bursts. The pulser input voltage is constant at 4 kV for all tests in this chapter, except those presented in Fig. 5.6, where the effect of pulser input voltage on gain is studied. Also, with the exception of the spatial gain studies, the probe laser is directed along the centerline of the gas discharge tube.

Variation of gain, with and without a magnetic field, as a function of DC power supply voltage is shown in Fig. 5.3. In each case, the gain is seen to be an increasing function of applied voltage. Based on the discussion of section 5.1, this was to be expected. Using Eq. 5.6, the E/N ratio at 2.25 kV is calculated to be $0.6(10)^{-16}$ V-cm^2. At an input voltage of 3.5 kV, E/N becomes $1.2(10)^{-16}$, a value close to the optimum for maximum energy deposition into the vibrational level of N_2. The maximum applied voltage used in these tests is 3.5 kV. If increased beyond this point, the 17 msec burst of pulser pre-ionization was sufficient to initiate a self-sustained arc discharge. The ensuing high current constricted discharge so generated exhibited zero gain, owing to the high gas temperature that resulted. Thus, an applied voltage of 3.5 kV was the upper limit where the burst discharge technique could be applied.

Fig. 5.3 reveals that the centerline gain reduces with the application of the transverse rotating magnetic field. There are two possible explanations for this phenomena. The first centers around the concept of effective pressure[55], as discussed in Chapter 3. Under this concept, a transverse magnetic field causes a gas discharge to behave as though the pressure is increased by a factor $\{1 + \beta_e^2\}^{1/2}$. For the parameters of interest, (B = 450 Gauss and T = 25°C), the electron Hall parameter, $\beta_e = \omega_{ce}/\nu_{en} = 0.24$, and the increased pressure factor, $\{1 + \beta_e^2\}^{1/2} = 1.06$. With a 6% increase in the effective pressure, E/N decreases by approximately the same amount. Thus, for the DC input voltage of 3.5 kV, this results in an E/N drop from $1.2(10)^{16}$ V-cm^2 to $1.13(10)^{-16}$ V-cm^2. This change is too small to account for the large drop in laser gain that is observed, when the transverse rotating magnetic field is applied.

The second, and more probable, explanation for the drop in gain is based on the observation that the discharge cross-sectional area increases with the application of the transverse rotating magnetic field. As discussed earlier, high speed photography revealed that the discharge is in fact deflected away from the centerline position by the tranverse magnetic field. Consequently, as the magnetic field rotates, the plasma column sweeps azimuthally through the discharge tube, with the radius of rotation being an increasing function of the

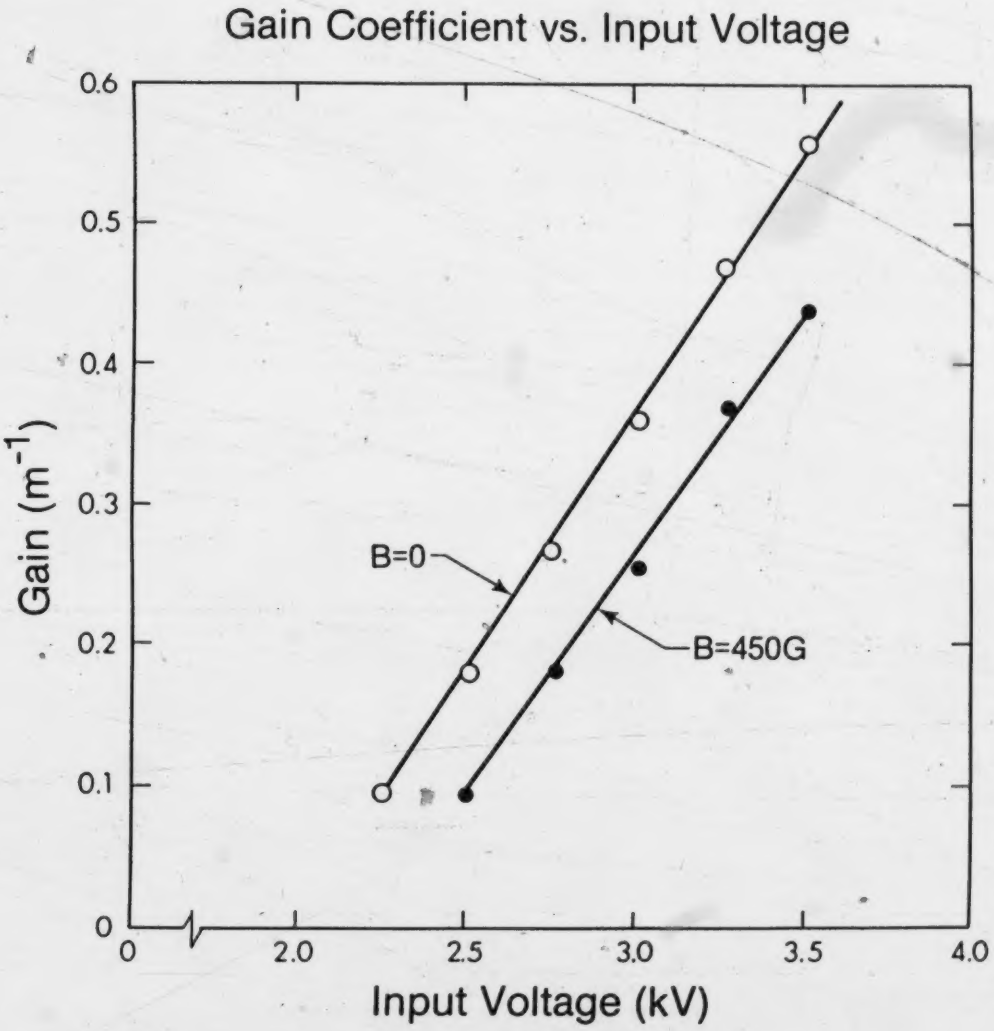

Fig. 5.3 Gain Coefficient vs. DC Input Voltage

magnetic field strength.[63] As a consequence of this situation, the centerline gain measurement yields a lower value, because the probe laser, being on axis, is probing only the edge of the rotating discharge column.

To study this "edge effect", a gain test was done with a constant applied voltage of 3 kV and a magnetic field varying from zero to 450 Gauss. The resulting gain coefficient, obtained as a function of magnetic field strength, is shown in Fig. 5.4. At zero magnetic field strength, a gain coefficient of 0.37 m^{-1} is observed. As the column deflects away from the axis, the centerline gain decreases, until at a magnetic field of 450 Gauss, the centerline gain has been reduced to 0.27 m^{-1}.

To study this magnetic field effect still further, the probe laser was scanned across a diameter of the discharge chamber. The scanning distance was limited to the 4 cm clear aperture of the ZnSe window. This test was also performed with a constant terminal voltage of 3 kV. Spatial variation of gain, with and without magnetic field, is shown in Fig. 5.5. With zero magnetic field, the discharge establishes itself on axis. Maximum gain is observed on the centerline and decreases as the probe laser is moved radially. Fig. 5.5 shows that the gain profile is inverted when the transverse rotating magnetic field is applied. However, the data used for the case when the field was applied are the maximum gains observed, apart from the centerline gain, which was constant. In fact, the values recorded by the detector fluctuated wildly when the magnetic field was used. The reason for this is as follows: The magnetic field rotates with a period of 1/60 sec. However, the plasma exists only for ~17 msec, and then is extinguished for ~800 msec, before being re-established. The signal recorded by the detector depended on where the discharge happened to be, relative to the detector's optical path, when the discharge was established.

The next experiment studied the variation of gain with changes in pulser input voltage. In Figs. 4.29 and 4.31, it was shown that the electron density is an increasing function of pulser input voltage. Thus, this gain test is effectively a study of gain versus electron density. Investigations by Bullis[16] and Fowler[88] have shown that gain increases with electron density. This is because the vibrational excitation of the N_2 molecules is dependent on

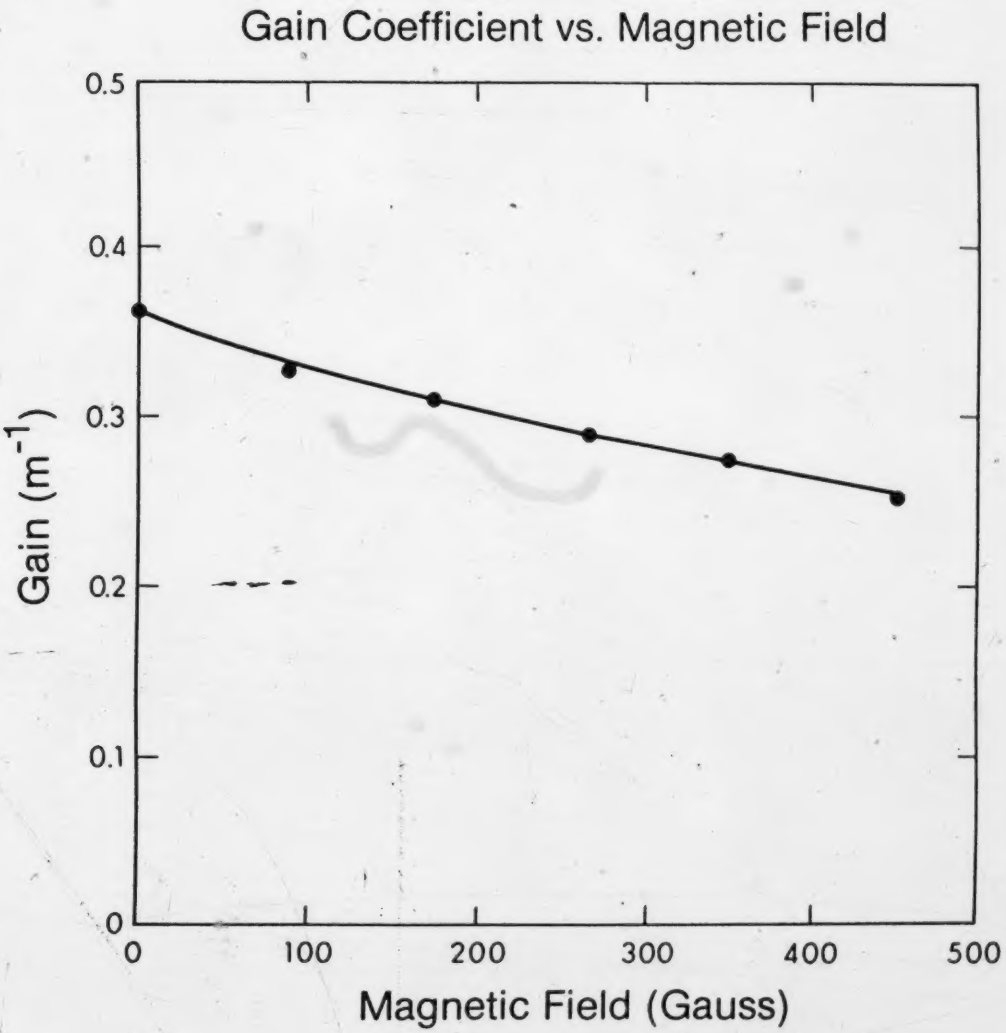

Fig. 5.4 Gain Coefficient vs. Magnetic Field

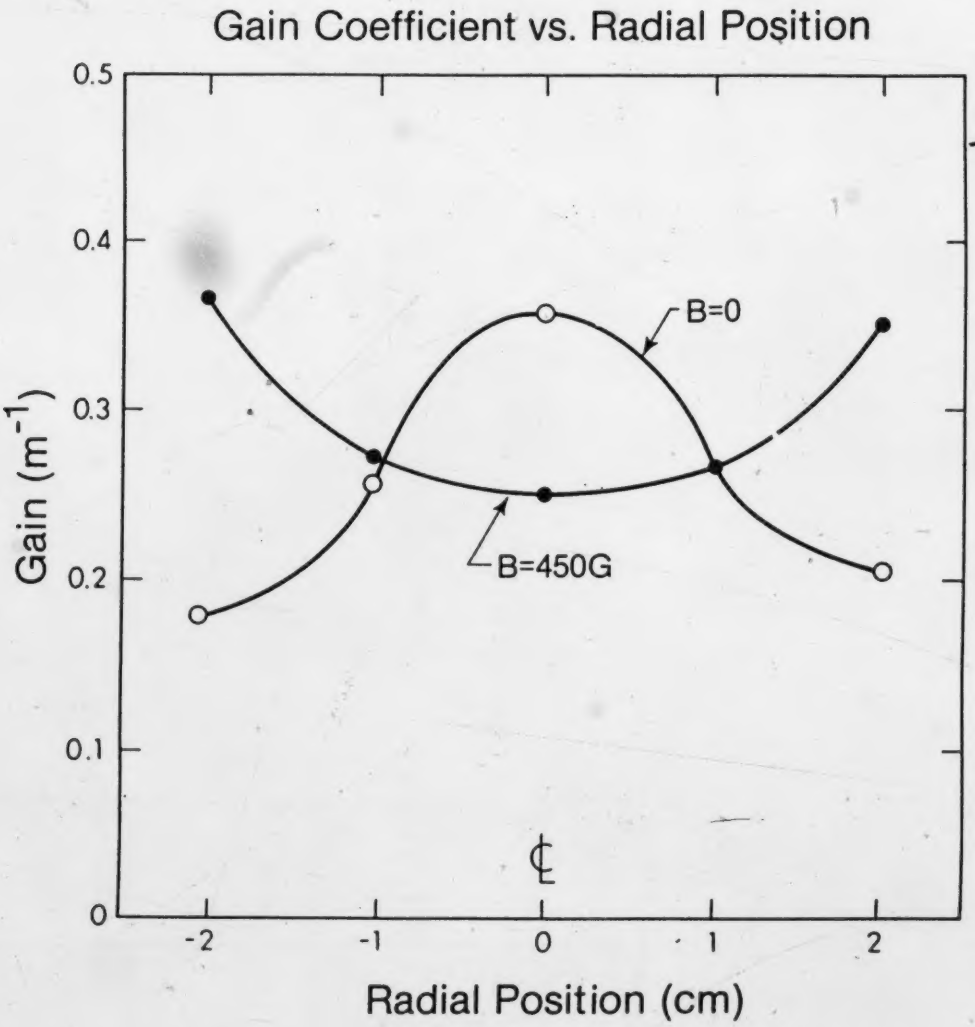

Fig. 5.5 Maximum Gain Coefficients vs. Radial Position

inelastic collisions between electrons and N_2 molecules.[10] The test was done with zero magnetic field, a DC terminal voltage of 3 kV, and with the probe laser repositioned on axis. The data so collected of the variation of gain with pulser input voltage is shown in Fig. 5.6. With pulser input voltages between 1 and 2.5 kV, the gain remains below 0.1 m^{-1}. Clearly, these low electron densities provide insufficient vibrational excitation of the N_2 molecules. Hence, with a limited population inversion, the resultant gain is small. Between 3 and 4 kV, the greatly increasing electron density is able to sustain a much larger population inversion, resulting in a rapidly increasing gain. (The electron density at 4 kV pulser input voltage is 2.33 times greater than at a pulser input voltage of 2 kV. See Figs. 4.29 and 4.31.) For pulser input voltages greater than 4 kV, the ionization provided by the 17 msec burst of pre-ionization is enough that the plasma is maintained long after 17 msec has passed. By the time the pulser input voltage has reached 5 kV, this long living plasma causes gas heating. Consequently, the gain value observed deviates from the expected dashed line, as shown in Fig. 5.6. Increasing the pulser input voltage past 5 kV, initiates a discharge that does not extinguish between bursts. Immediate gas heating results, and the gain reduces to zero.

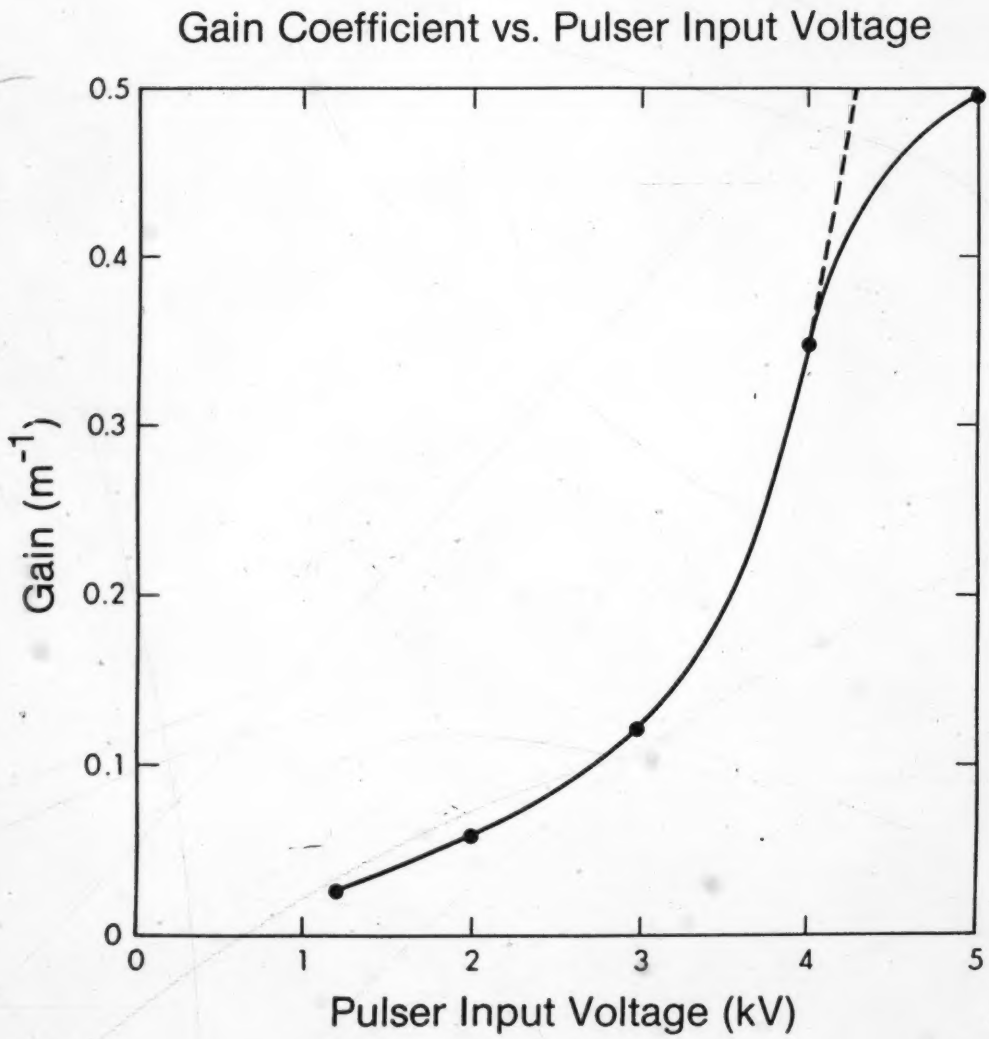

Fig. 5.6 Gain Coefficient vs. Pulser Input Voltage

5.5 Saturation Intensity

The saturation intensity is defined as the point at which the excitation of CO_2 molecules to the upper laser state, $CO_2(00^01)$, becomes exactly balanced by the loss of $CO_2(00^01)$ molecules by stimulated emission and other loss mechanisms. Experimental determination of the saturation intensity involves measuring the gain of the amplifying media while varying the output power of the probe laser. This is achieved by using the variable attenuator to scan through a full range of probe power inputs into the gas discharge.

Technically, a combination of both homogeneous and inhomogeneous broadening are responsible for determining the gain line profile. However, for the gas mixture considered here, (CO_2:CO:N_2:He = 1:1:4:14), homogeneous line broadening mechanisms are dominant.[89] This is confirmed by experimental results to follow, where the gain variation follows that predicted for a homogenously broadened medium.[90]

Gain saturation for a gas discharge with homogeneous broadening is given by the differential equation:[91]

$$\frac{dI}{dz} = \frac{\alpha_0 I}{1 + (I/I_{sat})} , \tag{5.15}$$

where I, I_{sat}, and z are the intensity of the probe beam, saturation intensity and axial position respectively. The small signal gain coefficient, α_0, is the theoretical maximum gain possible when the intensity of the probe laser beam approaches zero. Rearranging Eq. 5.15 and integrating, yields:

$$ln\left[\frac{I_{out}}{I_{in}}\right] = -\left[\frac{I_{out} - I_{in}}{I_{sat}}\right] + \alpha_0 L , \tag{5.16}$$

where I_{in} and I_{out} are the input and output probe beam intensities. Eq. 5.16 is the equation of a straight line, with the slope given by $-1/I_{sat}$ and the y-intercept being $\alpha_0 L$. Thus, by plotting $ln(I_{out}/I_{in})$ versus $(I_{out} - I_{in})$, I_{sat} and α_0 may be evaluated.

The intensity of the probe laser beam is related to its average power, the frequency of modulation, the width of the probe laser pulse and the area of the beam. Since the modulated RF probe laser produces square pulses, the intensity of the beam is simply given by:

$$I = \frac{P_{av}}{A\tau_p f} , \tag{5.17}$$

where P_{av}, A, τ_p, and f are the average power, probe beam area, pulse width and frequency respectively. The average power of the beam is recorded with a thermopile laser power meter (Coherent 201). The frequency of modulation is 1000 Hz, and the width of the probe laser pulses is 100 μsec. The average beam diameter of the input and output beams is 0.7 cm, and so upon substitution into Eq. 5.17,

$$I(W/cm^2) = 26\ P_{av}(W) . \tag{5.18}$$

Experimental results used in deriving the saturation intensity and small signal gain are shown in Fig. 5.7. From the slope of the curve, the saturation intensity is calculated to be 160.6 W/cm^2. Because the length of the gain path is 1 m, (twice the length of the gas discharge), $\alpha_0 L = \alpha_0$, and the small signal gain of 0.85 m^{-1} is taken directly from the y-intercept of Fig. 5.7. These values of small signal gain and saturation intensity are comparable to those presented elsewhere. As an example, Yessik and MacKen[92] report a small signal gain of 1.5 m^{-1} and a saturation intensity of 203 W/cm^2 for their 1 meter long CO_2 laser.

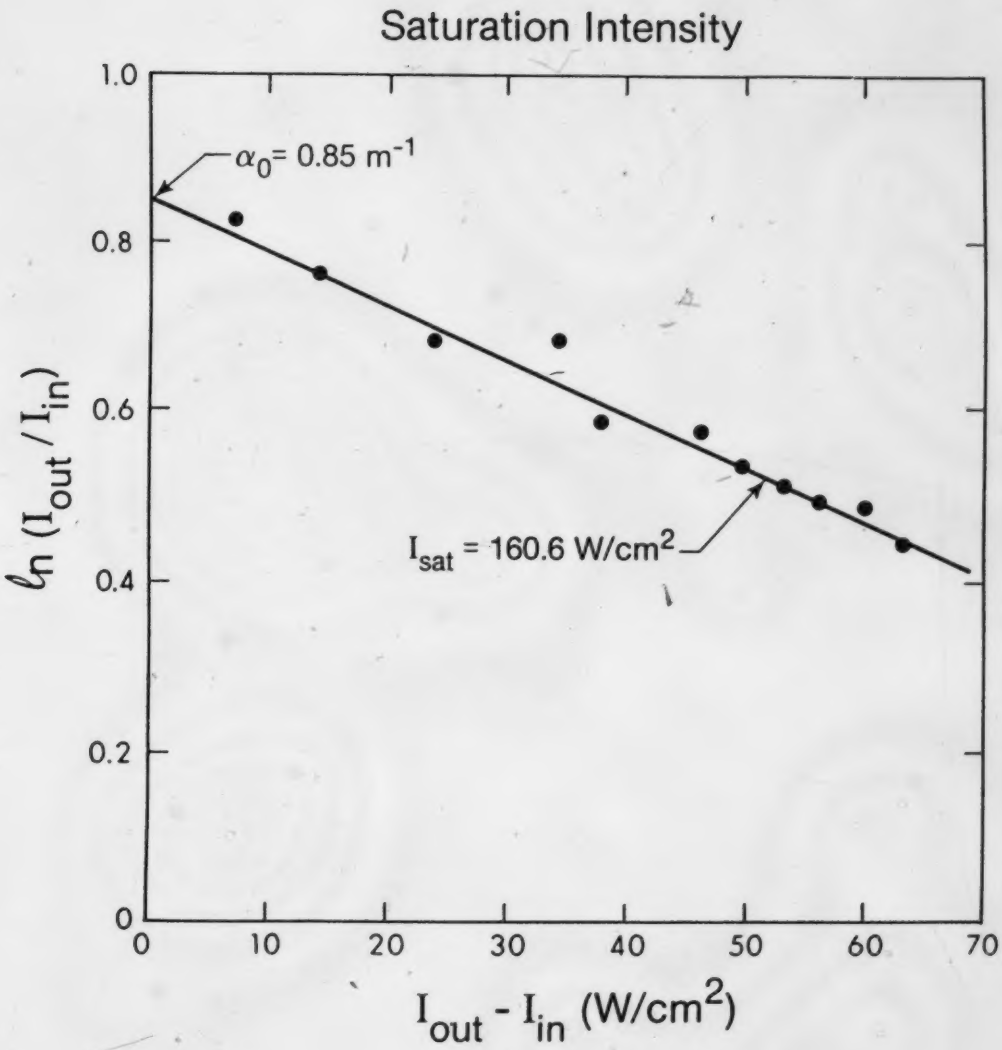

Fig. 5.7 Saturation Intensity

5.6 Laser Power Measurements

The gain measurements demonstrated that there was some potential for laser output. A brief laser power test was done by replacing the ZnSe window, used for the gain measurements, with an adjustable, partially transmitting, coated ZnSe mirror. Transmittance of the flat ZnSe mirror is 30%. The radius of curvature of the adjustable aluminum mirror is 2 m. These two optical elements form an elementary stable resonator.

Laser power measurements were performed using the same burst pulse technique as was used for gain measurements. The laser power detector (Gentec ED-200) has a typical output of 5 mV/mJ. Laser power output as a function of DC applied voltage, for three separate runs, all with zero magnetic field, is shown in Fig. 5.8. As is evident, the repeatability of the data between runs is poor. The primary reason for this is that the gas discharge apparatus was designed as a testbed for gas discharge analysis. As such, little attention was paid to eliminating vibration of the apparatus. The motors used for ballast solution flow and for gas transport vibrated the entire system, resulting in constant misalignment of the optical system. Under these conditions, no consistent quantitative analysis was possible.

Qualitative analysis, however, is possible. The laser power output is an increasing function of DC input voltage up to almost 3 kV. This is consistent with the gain observations presented earlier. The laser power output then peaks and drops to zero with increased DC input voltage. This is the result of increasing gas temperature.

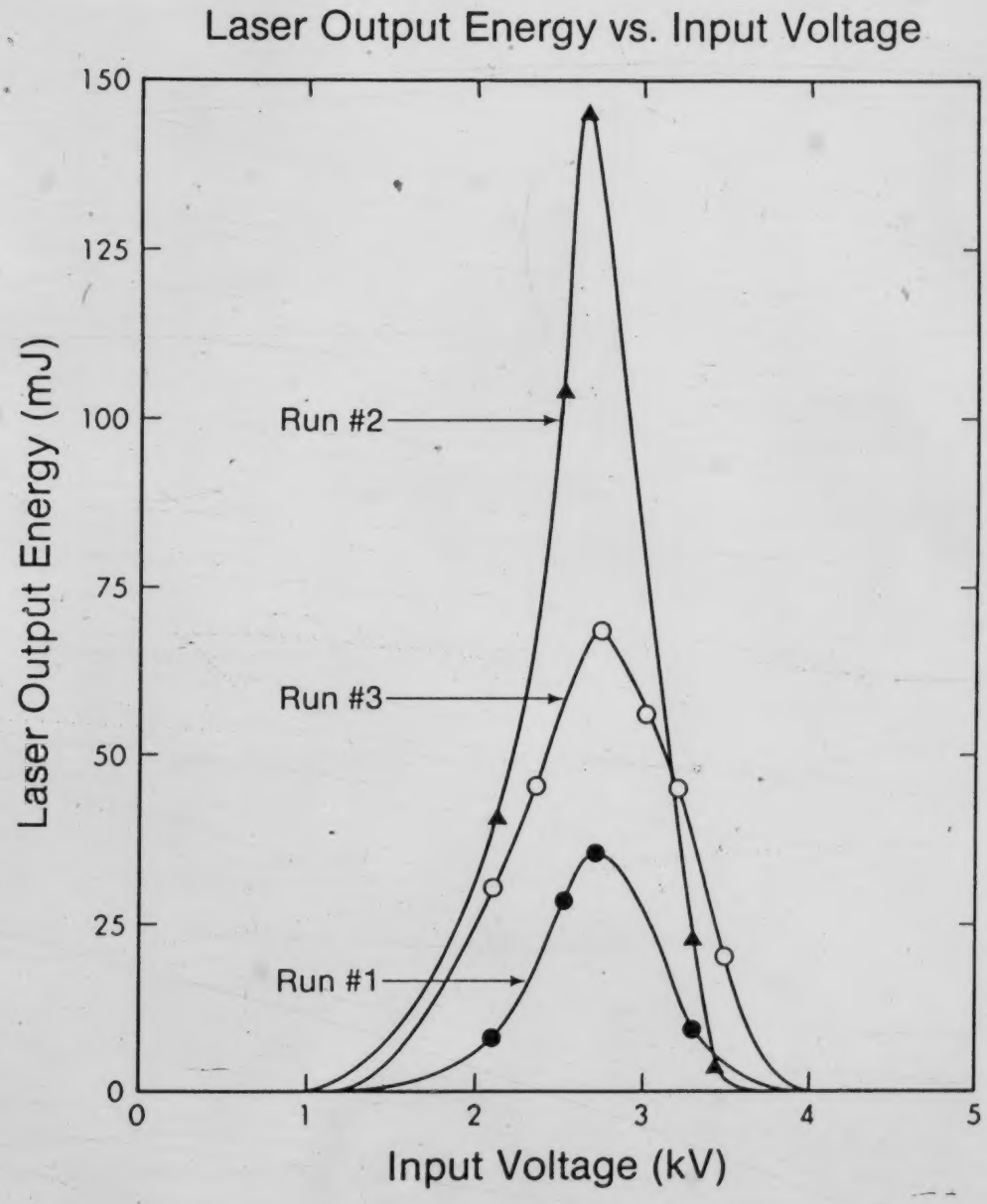

Fig. 5.8 Laser Output Energy vs. Input Voltage

CHAPTER VI

CONCLUSIONS AND CONSIDERATIONS FOR FUTURE RESEARCH

The results presented in this thesis have shown that the use of a transverse rotating magnetic field allows for increased plasma power loading into an axial gas discharge. High speed photography revealed that the plasma is in fact deflected away from the centerline position when the magnetic field is applied.

Theoretical analysis showed that this effect was the result of a Lorentz force acting on the plasma column. As the magnetic field rotated, the plasma column swept across the tube cross-section at the same angular velocity as the impressed magnetic field. With increasing magnetic field strength, the Lorentz force grew, and deflected the plasma column still closer to the chamber wall. At pressures of ~5 Torr, a 450 Gauss field was of sufficient strength to force the plasma column into the container wall; thus extinguishing the discharge.

The terminal characteristics showed that the plasma is held in the abnormal glow discharge region for a higher applied voltage with the application of such a rotating magnetic field. The higher terminal voltage necessary to maintain a given current, when the magnetic field was applied, was a result of: (i) the magnetic field deflecting the plasma column away from the center of the discharge tube, and into cooler, less conductive, neutral gas and (ii) the axial electron conductivity being reduced by the imposition of the transverse magnetic field.

Electron density experiments, performed at a pressure of 20 Torr, demonstrated no spatial variation in electron density when the transverse rotating magnetic field was applied. It was speculated that any spatial variation in electron density, that may in fact have existed, were being masked by pulser effects. To test this hypothesis, an electron density measurement was made at a lower pressure of 5 Torr, where the sustainer supply alone was able to maintain the discharge, without the need for external ionization. This test revealed that the electron density had both spatial and temporal variations at this low pressure. The electron

density was understandably highest when the plasma column swept through the probe area. However, the density at other locations of the cross-section, did not fall to zero, and so, despite the Lorentz force effects, current was still flowing in all regions. Furthermore, the electron density was uniform over roughly half of the discharge cross-section.

Results obtained in the gain measurement studies indicated that the centerline gain was a decreasing function of magnetic field. This was due to the increasing deflection of the plasma away from the tube bore with an increasing applied magnetic field. Centerline gain was also shown to be an increasing function of pulser input voltage, provided that the discharge remained extinguished between bursts of external ionization. Data for both the gain and the saturation intensity measurements were comparable to those presented elsewhere. Only a qualitative analysis was possible for the laser power assessments. These showed that the variation of laser output power was consistent with the gain observations.

At this, the conclusion of the project, it is desirable to make a number of recommendations regarding future work with this discharge apparatus. A study should be undertaken to investigate the effect of varying the rotational velocity of the magnetic field. There is likely a minimum rotational velocity below which the discharge moves too slowly to prevent thermal instabilities from occuring. Effects due to a faster (than 60 Hz) rotational velocity should also be explored as a means of providing more uniform ionization in the discharge tube; thereby resulting in more uniform gain across the tube cross-section.

Ideally, the plasma should be rotated as fast as possible. However, there are two reasons why the rotation frequency may not be set to an indiscriminately high value. Firstly, the penetration of a magnetic field into a conducting medium varies inversely with rotational frequency. This is seen clearly by considering the classical skin depth, given by:[93]

$$\delta = \left[\frac{2}{\mu_0 \sigma_\perp \omega}\right]^{1/2} , \qquad (6.1)$$

where all parameters are as defined previously (see section 2.2). For a conductivity of 4.48 C^2-sec/kg-m^3 and a 60 Hz rotational frequency ($\omega = 120\pi$ sec^{-1}), the classical skin depth, δ,

is 30.7m, indicating complete penetration of the plasma column by the rotating magnetic field.

The discussions of section 2.2 indicated that the magnetic Reynolds number, R_m, had to be much less than one in order that the applied magnetic field lines were not distorted by the plasma column. Taking $R_m = 0.01$ and using Eq. 2.45, a rotational frequency, ω, of $7.1(10)^5$ sec^{-1} or 113 kHz is calculated. In this case, the classical skin depth is 71cm, which is still much larger than the 10cm diameter of the discharge tube.

The second limit on the rotational frequency is a restriction due to the rotating magnetic field structure. If the frequency applied to the magnetic field coils is increased, then the applied voltage must also be increased proportionately to maintain the same magnetic flux density in the discharge tube.[94] A rotational frequency of 113 kHz implies that a voltage of 414 kV would be required, which is clearly impractical, if not impossible. Thus, in practice, the limitation on rotational frequency is due to the experimental configuration in use, rather than a concern regarding the skin depth and penetration of the magnetic field into the plasma column.

Another experiment, currently under consideration, proposes to utilize static transverse magnetic fields interacting with an axial AC electric field. This configuration eliminates the need for the power consuming and expensive rotating magnetic field coils, and allows the use of permanent magnets instead. However, it remains to be seen if the same enhanced stability will be achieved, as was demonstrated with the present apparatus.

In conclusion, the magnetic stabilization concept, using a transverse rotating magnetic field, has been shown to be effective in suppressing electrothermal instabilities in an axial electric discharge. Theoretical and experimental analysis determined that the enhanced stability was the result of Lorentz forces acting on the gas discharge. Using this discharge stabilization technique, a 25% increase in discharge power loading was demonstrated.

REFERENCES

[1] R. Walker, *Applying Multikilowatt CO_2 Lasers in Industry*, Lasers and Applications, April 1984

[2] V.E. Merchant, *Development of a New 20-kW CO_2 Laser*, Laser Focus, May 1985

[3] A.J. Demaria, *Review of CW High-Power CO_2 Lasers*, Proc. IEEE **61**, 731 (1973)

[4] M.W. Sasnett, *Comparing Industrial CO_2 Lasers*, Lasers and Applications, Sept. 1984

[5] P.A. Miles, J.W. Lotus, *A High Power CO_2 Laser Radar Transmitter*, IEEE J. Quantum Electron. **QE-4**, 811 (1968)

[6] P.K. Cheo, *Effects of Gas Flow on Gain of 10.6 micron CO_2 Laser Amplifiers*, IEEE J. Quantum Electron. **QE-3**, 683 (1967)

[7] T.F. Deutsch, F.A. Horrigan, R.I. Rudko, *CW Operation of High Pressure Flowing CO_2 Lasers*, Appl. Phys. Lett. **15**, 88 (1969)

[8] W.B. Tiffany, R. Targ, J.D. Foster, *Kilowatt CO_2 Gas Transport Laser*, Appl. Phys. Lett. **15**, 91 (1969)

[9] S.L. Ream, *Present and Future Acceptance of High-Power CO_2 Lasers*, Laser Focus, Dec. 1982

[10] J.T. Verdeyen, *Laser Electronics*, (Prentice-Hall, New Jersey, 1981)

[11] C.J. Elliot, O.P. Judd, A.M. Lockett, S.D. Rockwood, *Electron Transport Coefficients and Vibrational Excitation Rates for Electrically Excited CO_2 Lasers*, Los Alamos Scientific Laboratory Research Report LA-5562-MS (1974)

[12] B.E.Cherrington, *Gaseous Electronics and Gas Lasers*, (Pergamon, Oxford 1979)

[13] R.L. Taylor, S. Bitterman, *Survey of Vibrational Relaxation Data for Processes Important in the CO_2-N_2 Laser System*, Rev. Mod. Phys. **41**, 26 (1969)

[14] T.J. Bridges, C.K.N. Patel, *High-Power Brewster Window Laser at 10.6 microns*, Appl. Phys. Lett. **7**, 244 (1965)

[15] D.L. Franzen, R.J. Collins, *Radial Gain Profiles in CO_2 Laser Discharges*, IEEE J. Quantum Electron. **QE-8**, 400 (1972)

[16] R.H. Bullis, W.L. Nighan, M.C. Fowler, W.J. Wiegand, *Physics of CO_2 Electric*

Discharge Lasers, AIAA Journal **10**, 407 (1972)

[17] W.J. Wiegand, W.L. Nighan, *Plasma Chemistry of CO_2-N_2-He Discharges*, Appl. Phys. Lett **22**, 583 (1973)

[18] A.A. Radzig, B.M. Smirnov, *Reference Data on Atoms, Molecules and Ions*, (Springer-Verlag, New York, 1985)

[19] K. Smith, R.M. Thomson, *Computer Modelling of Gas Lasers*, (Plenum, New York, 1978)

[20] W.L. Nighan, W.J. Wiegand, *Influence of Negative-Ion Processes on Steady-State Properties and Striations in Molecular Gas Discahrges*, Phys. Review A **10**, 922 (1974)

[21] R.A. Hass, *Plasma Stability of Electric Discharges in Molecular Gases*, Phys. Review A **8**, 1017 (1973)

[22] W.L. Nighan, W.J. Wiegand, R.A. Haas, *Ionization Instability in CO_2 Laser Discharges*, Appl. Phys. Lett **22**, 579 (1974)

[23] W.J. Wiegand, M.C. Fowler, J.A. Benda, *Carbon Monoxide Formation in CO_2 Lasers*, Appl. Phys. Lett. **16**, 237 (1970)

[24] J.J. Lowke, A.V. Phelps, B.W. Irwin, *Predicted Electron Transport Coefficients and Operating Conditions of CO_2-N_2-He Laser Mixtures*, J. Appl. Phys. **44**, 4664 (1973)

[25] C.A. Fenstremacher, M.J. Nutter, W.T. Leland, K. Boyer, *Electron-Beam Controlled Electrical Discharges as a Method of Pumping Large Volumes of CO_2 Laser Media at High Pressure*, Appl. Phys. Lett. **20**, 56 (1972)

[26] O.P. Judd, *An Efficient Electric CO_2 Laser Using Preionization by UV Radiation*, Appl. Phys. Lett. **22**, 95 (1973)

[27] H.J.J. Seguin, K.H. Nam, J. Tulip, *The Photoinitiated Impulse-Enhanced Electrically Excited (PIE) Discharge for High-Power CW Laser Applications*, Appl. Phys. Lett. **32**, 418 (1978)

[28] V.E. Merchant, H.J.J. Seguin, J. Dow, *High-Power High-Repetition Rate Pulser for Photo-Impulse Ionized Lasers*, Rev. Sci. Instrum. **49**, 1631 (1978)

[29] G.I. Shapiro, *Suppression of the Attachment Instability in a Glow Discharge by a*

Rotating Electric Field, Sov. Tech. Phys. Lett. **4**, 411 (1978)

[30] N.I. Lipatov, A.P. Mineev, V.I. Myshenkov, P.P. Pashinin, A.M. Prokhorov, *Stabilizing Effect of an AC Magnetic Field on the Ionizational-Thermal Instability of a Glow-Discharge Plasma*, Sov. Tech. Phys. Lett. **10**, 171 (1984)

[31] R.H. Lynch, *Constriction of the Thermally Inhomogeneous Positive Column with Volume Recombination*, J. Appl. Phys. **38**, 3965 (1967)

[32] G.L. Rogoff, *Gas Heating Effects in the Constriction of a High-Pressure Glow Discharge Column*, Phys. Fluids **15**, 1931 (1972)

[33] C. Kenty, *Volume Recombination, Constriction, and Volt-Ampere Characteristic of the Positive Column*, Phys. Rev. **126**, 1235 (1962)

[34] J.H. Jacob, S.A. Mani, *Thermal Instability in High-Power Laser Discharges*, Appl. Phys. Lett. **26**, 53 (1975)

[35] W.L. Nighan, W.J. Wiegand, *Causes of Arcing in CW CO_2 Convection Laser Discharges*, Appl. Phys. Lett. **25**, 633 (1974)

[36] W.L. Nighan, *Causes of the Thermal Instability in Externally Sustained Molecular Discharges*, Phys. Rev. A **15**, 1701 (1977)

[37] A.C. Eckbreth, J.W. Davis, *RF Augmentation in CO_2 Closed-Cycle DC Electric-Discharge Convection Lasers*, Appl. Phys. Lett. **21**, 25 (1972)

[38] H.J.J. Seguin, J. Tulip, *Photoinitiated and Photosustained Laser*, Appl. Phys. Lett. **21**, 414 (1972)

[39] K.H. Nam, H.J.J. Seguin, J. Tulip, *Operational Characteristics of a PIE CO_2 Laser*, IEEE J. Quantum Electron. **QE-15**, 44 (1979)

[40] H.J.J. Seguin, K.H. Nam, J. Tulip, *An Efficient Multielement Cathode for High Power Electric Discharge Laser Applications*, J. Appl. Phys. **49**, 4566 (1978)

[41] H.J.J. Seguin, C.E. Capjack, D.M. Antoniuk, K.H. Nam, *High-Power Laser Discharge Stabilization with Magnetic Fields*, Appl. Phys. Lett. **37**, 130 (1980)

[42] D.M. Antoniuk, C.E. Capjack, H.J.J. Seguin, *Computer Simulation of Gas Transport in a Magnetically Stabilized Glow Discharge*, J. Appl. Phys. **55**, 708 (1984)

[43] C.E. Capjack, H.J.J. Seguin, D. Antoniuk, V.A. Seguin, *A Magnetically Stabilized Coaxial Laser Discharge*, Appl. Phys. B , **26**, 161 (1981)

[44] C.E. Capjack, D.M. Antoniuk, H.J.J. Seguin, *Dynamics of a Magnetically Stabilized Laser Discharge*, J. Appl. Phys. **52**, 4517 (1981)

[45] R. Razdan, C.E. Capjack, H.J.J. Seguin, *Influence of a Magnetic Field on the Growth of Instabilities in a Helium Glow Discharge using Monte Carlo Simulation of the Cathode Fall Region*, J. Appl. Phys. **57**, 4954 (1985)

[46] R. Razdan, C.E. Capjack, H.J.J. Seguin, *Charge Carrier Dynamics of a CO_2 Laser Plasma in a Magnetized Cathode Glow*, Appl. Phys. Lett. **48**, 1513 (1986)

[47] G.W. Sutton, A. Sherman, *Engineering Magnetohydrodynamics*, (McGraw-Hill, New York, 1965)

[48] E. Nasser, *Fundamentals of Gaseous Ionization and Plasma Electronics*, (Wiley, New York, 1971)

[49] M. Mitchner, C.H. Kruger, Jr., *Partially Ionized Gases*, (Wiley, New York, 1973)

[50] C.M. Van Atta, *Vacuum Science and Engineering*, (McGraw-Hill, New York, 1965)

[51] S. Chapman, T.G. Cowling, *The Mathematical Theory of Non-Uniform Gases*, (Cambridge Univ. Press, 1970)

[52] M. Cloutier, *Computed Physical and Thermodynamic Properties of Various $He/CO_2/N_2$ Mixtures*, DREV Technical Notes, Quebec, Canada (1970)

[53] F.F. Chen, *Introduction to Plasma Physics*, (Plenum, New York, 1974)

[54] N.A. Krall, A.W. Trivelpiece, *Principles of Plama Physics*, (McGraw-Hill, New York, 1973)

[55] H.A. Blevin, S.C. Haydon, *The Townsend Ionization Coefficients in Crossed Electric and Magnetic Fields*, Aust. J. Phys. **11**, 18 (1958)

[56] M.J. Bernstein, *Townsend Ionization Coefficient for Hydrogen in a Transverse Strong Magnetic Field*, Phys. Rev. **127**, 342 (1962)

[57] D.M. Antoniuk, *A Magnetohydrodynamic Approach to Laser Discharge Stabilization*, Ph.D. Thesis, University of Alberta, Canada (1983)

[58] W.F. Hughes, J.A. Brighton, *Fluid Dynamics - Schaum's Outline Series*, (McGraw-Hill, New York, 1967)

[59] P.M. Morse, H. Feshbach, *Methods of Theoretical Physics, Part I*, (McGraw-Hill, New York, 1953)

[60] C. Devanathan, P.L. Bhatnager, *Flow Induced in a Cylindrical Column by a Uniformly Rotating Magnetic Field*, Proc. Roy. Soc. (London) A **297**, 558 (1967)

[61] P. Smith, *The Rotation of a Conducting Liquid in a Uniform Transverse Magnetic Field*, Z. angew. Math. und Mech. **44**, 495 (1964)

[62] M. Abramowitz, I. Stegun, eds., *Handbook of Mathematical Functions*, (Dover, New York, 1972)

[63] R.J.Willis, C.E. Capjack, H.J.J. Seguin, *Axial Discharge Stabilization using a Rotating Magnetic Field*, submitted to Phys. Lett. A (1987)

[64] K.H. Nam, *A Kilowatt P.I.E. CO_2 Laser*, Ph.D Thesis, University of Alberta (1978)

[65] A. von Engel, *Ionized Gases*, (Oxford University, Oxford, 1965)

[66] V.E. Merchant, H.J.J. Seguin, J. Dow, *Novel Transformer Designs for High-Power High-Repetition Rate Applications*, Rev. Sci. Instrum. **50**, 1151 (1979)

[67] W.J. Beek, K.M.K. Muttzall, *Transport Phenomena*, (Wiley, New York, 1975)

[68] I. Langmuir, M. Mott-Smith, *The Theory of Collectors in Gaseous Discharges*, Phys. Rev. **28**, 727 (1926)

[69] J.D. Swift, M.J.R. Schwar, *Electric Probes for Plasma Diagnostics*, (American Elsevier, New York, 1977)

[70] P.R. Smy, *The use of Langmuir Probes in the Study of High Pressure Plasmas*, Adv. in Phys. **25**, 517 (1976)

[71] M.A. Heald, C.B. Wharton, *Plasma Diagnostics with Microwaves*, (Wiley, New York, 1965)

[72] R.E. Kiel, *Probe Theory for Spheres and Cylinders*, J. Appl. Phys. **40**, 3668 (1969)

[73] C.H. Su, S.H. Lam, *Continuum Theory of Spherical Electrostatic Probes*, Phys. Fluids **6**, 1479 (1963)

[74] R.M. Clements, P.R. Smy, *Electrostatic-Probe Studies in a Flame Plasma*, J. Appl. Phys. **40**, 4553 (1969)

[75] F.F. Chen, *Plasma Diagnostic Techniques*, ed. by R.H. Huddlestone and S.L. Leonard, (Academic Press, New York, 1965)

[76] A.I. Ivanchenko, A.A. Shepelenko, *Voltage Drop at the Cathode of a Glow Discharge at Moderate Pressures in Nitrogen and a Mixture of CO_2-Laser Gases*, Teplofiz. Vys. Temp. **20**, 636 (1981)

[77] D.C. McKen. *A Parametric Study of Ultra-Violet Photoionization for CO_2 Lasers*, Ph.D Thesis, University of Alberta (1976)

[78] W.L. Nighan, *Electron Energy Distributions and Collision Rates in Electrically Excited N_2, CO and CO_2*, Phys. Review A, **2**, 1989 (1970)

[79] O.P. Judd, *The Effect of Gas Mixture on the Electron Kinetics in the Electrical CO_2 Gas Laser*, J. Appl. Phys. **45**, 4572 (1974)

[80] J.D. Cobine, *Gaseous Conductors*, (Dover, New York, 1958)

[81] A.M. Robinson, E.F. Girczyc, *High Temperature 10.4 μm Absorption in CO_2-N_2-He Mixtures*, Appl. Opt. **19**, 1969 (1980)

[82] O. Svelto, (trans. by D.C. Hanna), *Principles of Lasers, 2nd ed.*, (Plenum, New York, 1982)

[83] A.E. Hill, *Role of Thermal Effects and Fast Flow Power Scaling Techniques in CO_2-N_2-He Lasers*, Appl. Phys. Lett. **16**, 423 (1970)

[84] S.K. Nikumb, Personal Communication

[85] B. Gebhart, *Heat Transfer, 2nd ed.*, (McGraw-Hill, New York, 1971)

[86] D.R. Pitts, L.E. Sisson, *Heat Transfer – Schaum's Outline Series*, (McGraw-Hill, New York, 1977)

[87] W.F. Ames, *Numerical Methods for Partial Differential Equations*, (Academic Press, New York, 1977)

[88] M.C. Fowler, *A Quantitative Analysis of the Dependence of CO_2 Laser Performance on Electric Discharge Properties*, Appl. Phys. Lett. **18**, 175 (1970)

[89] V.A. Seguin, H.J.J. Seguin, C.E. Capjack, S.K. Nikumb, *Gain Characteristics of a MAGPIE Coaxial CO_2 Laser System*, IEEE J. Quantum Electron. **QE-23**, 600 (1987)

[90] A. Yariv, *Quantum Electronics*, (Wiley, New York, 1967)

[91] K.T.K. Cheng, L.W. Casperson, *Properties of a Coaxial CW CO_2 Laser*, Appl. Opt. **18**, 2130 (1979)

[92] M. Yessik, J.A. Macken, *Helical-Flow CO_2 Laser*, J. Appl. Phys. **54**, 1693 (1983)

[93] S. Ramo, J.R. Whinnery, T. Van Duzer, *Fields and Waves in Communication Electronics*, (Wiley, New York, 1965)

[94] A.E. Fitzgerald, C. Kingsley, Jr., A. Kusko, *Electric Machinery, 3rd ed.*, (McGraw-Hill, New York, 1971)